QUARTET MOUNTAIN LAMPROPHYRES AND CRUSTAL XENOLITHS: NEW INSIGHTS INTO THE MESOPROTEROZOIC METAMORPHIC HISTORY OF NORTHWESTERN LAURENTIA

by

Dejan Milidragovic
B.Sc. (Honors) Simon Fraser University, 2005

THESIS SUBMITTED IN PARTIAL FULFILLMENT OF
THE REQUIREMENTS FOR THE DEGREE OF

MASTER OF SCIENCE

In the
Department
of
Earth Sciences

SIMON FRASER UNIVERSITY

Spring 2008

APPROVAL

Name:	**Dejan Milidragovic**
Degree:	**Master of Science**
Title of Thesis:	**Quartet Mountain Lamprophyres and crustal xenoliths: new insights into the Mesoproterozoic metamorphic history of northwestern Laurentia**

Examining Committee:

Chair: **Dr. Andrew Calvert**
Professor, Department of Earth Sciences
Simon Fraser University

_____

Dr. Derek J. Thorkelson
Senior Supervisor
Professor, Department of Earth Sciences
Simon Fraser University

_____

Dr. H. Dan Gibson
Supervisor
Assistant Professor, Department of Earth Sciences
Simon Fraser University

_____

Dr. Dan D. Marshall
Supervisor
Associate Professor, Department of Earth Sciences
Simon Fraser University

_____

Dr. William J. Davis
Supervisor
Research Scientist and SHRIMP Facility Manager
Geological Survey of Canada

_____

Dr. James K. Mortensen
External Examiner
Professor, Department of Earth and Ocean Sciences
University of British Columbia

Date Defended/Approved: February 4th, 2008

ABSTRACT

The Quartet Mountain Lamprophyres are Early Cambrian ultramafic dykes that crosscut Proterozoic sedimentary strata in the Wernecke Mountains, east-central Yukon. They were derived from low-degree partial melting of a light REE-enriched garnetiferous upper mantle and have near-chondritic εNd_{530} values of -1.5 to 1.9. The lamprophyres contain xenoliths derived from the crust and upper mantle. SHRIMP U-Pb isotopic analysis of zircon from five xenoliths identified ages of metamorphism, at 1.60 Ga, 1.27 Ga and 1.15 Ga. The 1.60 and 1.27 Ga events were likely caused by nearby, documented events of metasomatism and magmatism. The 1.15 Ga metamorphism correlates with scattered igneous and metamorphic ages from the northern and central North American Cordillera, the Grenville orogen and the Sibao orogen of South China. The 1.15 Ga event in northwestern Cordillera is thought to reflect crustal heating in an extensional regime generated by the oblique convergence of the Yangtze Craton with western Laurentia.

Keywords: geochronology; sensitive high resolution ion microprobe (SHRIMP); zircon; Laurentia; Grenville; ultramafic lamprophyre

Subject Terms: lamprophyres; Earth-Crust; xenolith; zircon; U-Pb geochronology

PREFACE

This thesis consists of a paper describing the geology of the Quartet Mountain Lamprophyres and their constituent crustally derived xenoliths, followed by six appendices. The appendices provide supplemental information on methodologies and other details of this study, including some additional thoughts related to the subject.

The paper, entitled "Quartet Mountain Lamprophyres and crustal xenoliths: new insights into the Mesoproterozoic metamorphic history of northwestern Laurentia," summarizes the findings of this research, and can be subdivided into two main parts. The first part describes the petrology and geochronology of the Early Cambrian Quartet Mountain Lamprophyres and formalizes the suite, informally named by Thorkelson et al. (2003). The suite hereby includes the lamprophyre dykes reported by Delaney (1981), Laznicka and Gaboury (1988), Hulstein et al. (1994), Thorkelson et al. (2003) and Milidragovic et al. (2006). The second part of the paper describes the petrography, U-Pb geochronology and Sm-Nd geochemistry of select, crustal xenoliths, and provides a tectonic model that accounts for a poorly understood tectono-thermal pulse that affected the length of Canadian Cordillera at ca. 1.2-1.0 Ga. The paper and figures are prepared in the format prescribed by the journal *Precambrian Research.*

The paper is co-authored by Dr. D.J Thorkelson, Dr. D. Marshall, Dr. W.J. Davis and Dr. H.D. Gibson. Thorkelson contributed to editing of the text and figures throughout, and his knowledge and understanding of the regional geology and tectonics was instrumental in the writing of the "Geological Background" section, as well as the "big-picture" interpretation of the geochronological data. Marshall produced the cathodoluminescence (CL) images of the analyzed zircon grains, and conducted qualitative chemical analyses of mineral grains that could not be identified petrographically. Davis conducted the U-Pb isotopic analysis of more than 60 zircon domains over two days at the J.C. Roddick Ion Microprobe Laboratory in Ottawa. He provided valuable discussion and feedback regarding the interpretation of the U-Pb data. Gibson provided discussion regarding the interpretation of the U-Pb data, zircon textures and xenolith petrography. All co-authors contributed to the rigorous development of ideas and wording.

Appendices at the end of the paper include a more detailed discussion of xenolith petrography, sample preparation and methodology, and geochemical modelling, as well as some additional thoughts on the significance of the granulite-facies crustal xenoliths. In addition, a more detailed overview of the principles of SHRIMP U-Pb dating and Sm-Nd isotope geochemistry is presented. Furthermore, additional figures (Figs. A1-A12) are included in the appendices.

Fieldwork for this project was undertaken over a nine-day period (July 5th to July 13th) in the summer of 2005. The study area is situated in the Wernecke Mountains, central-eastern Yukon, ~150 km north of the town of Mayo and ~250

km east-northeast of Dawson City, and is contained within map sheets 106C/13, 106D/15, 106D/16,106E/1, 106E/2 and 106F/4. Access to the study area was gained by fixed wing aircraft on floats and by helicopter. During the nine days spent in the Wernecke Mountains, four helicopter-supported "fly-camps" served as bases for the search for lamprophyre dykes.

In memory of

Geoff Bradshaw,

whose help with the collection of

lamprophyre sample 2

will always be remembered

ACKNOWLEDGMENTS

Finally a section in which, instead of my being evaluated, I am tasked with evaluating the performance of those who contributed in making the past 30 months a very memorable experience.

Derek Thorkelson, my senior supervisor, is greatly thanked for his patience and mentorship, both in the field and in the lab. His big-picture approach to science will hopefully continue to influence me as I continue my professional development. I will also take this opportunity to apologize to Derek, in writing, for making him walk in circles. I thank Dan Marshall for being, in effect, a reserve senior supervisor, and for treating me as if I were his own student. I greatly appreciate the endless hours Dan spent with me imaging zircon, identifying minerals, and seeking biotite in biotite-free rocks. Dan Gibson's enthusiasm and intrest in most things Cordilleran or zircon made him a fantastic resource. The two months spent picking zircon in the middle of summer 2006 would have been unimaginably worse without Dan's words of wisdom. My experience with Bill Davis in Ottawa was mind-blowing – I have never learned so much in a 5-day period. I could only wish that my stay were twice as long. I also thank Jim Mortensen for agreeing to be my external examiner, and for the discussions we've had at various conferences.

I am especially indebted to Ryan Ickert whose field assistance was superb. Even after his departure to ANU he still remained a strong educating

force in my life. My CORD-lab mates, Christa, Sarah, and Francesca, all provided beneficial discussion on various topics of geology. I thank Gabe for being the coolest Maritimer in the department, and for the countless hours he spent at the SEM with me. Closly trailing Gabe in the coolest Maritimer category is Kevin Cameron, whose help is the main reason why the following document contains no mention of kyanite. Also much appreciated is Wes Groome's help in the petrography department. I thank Glenda and Tarja for making sure I adhered to deadlines and always received my pay. I also thank the grads, the faculty and many undergrads for making the last two and a half years fun and eventful.

I am very grateful to the Yukon Geological Survey for funding my fieldwork and giving me one of the most exciting jobs I have ever had. I especially thank Craig Hart and Don Murphy whose teachings in the earliest days of my M.Sc. were of high value. I am doubly indebted to Craig, who along with the late Geoff Bradshaw, helped me in sample collection on a brilliant sunny morning in July 2005. Discussions with John Mair about the petrogenesis of lamprophyres in those early days were highly beneficial.

I also thank Tom Ullrich (PCIGAR), Tom Pestaj (GSC) and Pat Hunt (GSC) for all their help with the laboratory-related aspects of my thesis. I thank Dr. Rob Creaser (U of A) for expeditious Nd isotope results.

A huge thank you goes to my mom, my dad, and especially my "little" sister, who spent numerous hours proof-reading my thesis, and listening to dry-runs of my presentations. For this, her vocabulary is now enriched with terms such as lamprophyre, kimberlite, suite, Wernecke Mountains, and phenocryst.

Finally, I thank all of my friends who have made sure that I remained active in non-academic circles of life.

TABLE OF CONTENTS

LIST OF FIGURES

LIST OF TABLES

QUARTET MOUNTAIN LAMPROPHYRES AND CRUSTAL XENOLITHS: NEW INSIGHTS INTO THE MESOPROTEROZOIC METAMORPHIC HISTORY OF NORTHWESTERN LAURENTIA

Abstract

The Quartet Mountain Lamprophyres (QML) are Early Cambrian volatile-rich ultramafic alkaline lamprophyre dykes that intrude the Proterozoic sedimentary strata in the Wernecke Mountains, east-central Yukon. The lamprophyres were derived from low-degree partial melting of a light rare earth element-enriched garnetiferous upper mantle and have near-chondritic εNd_{530} values of -1.5 to 1.9. The lamprophyres belong to a suite of Paleozoic alkaline to ultrapotassic igneous rocks that span the length of the northern Cordilleran miogeocline and whose genesis is attributed to extension along the northern proto-Pacific margin.

Entrainment of both crustal and mantle xenoliths accompanied the emplacement of QML into the crust of Yukon. One of the lamprophyres contains a wide range of xenolith types including upper amphibolite to granulite- facies, sillimanite-bearing xenoliths, as well as orthopyroxene-bearing and other strongly retrograded xenoliths. The petrography, detrital zircon geochronology and Sm-Nd isotope geochemistry of the xenoliths suggest derivation from a supracrustal sequence indistinguishable from the Paleoproterozoic Wernecke Supergroup. Sensitive High Resolution Ion Microprobe (SHRIMP) analysis of zircon crystals

from five of the xenoliths identified three episodes of metamorphism at: (1) ca. 1.60 Ga, coincident with formation of the hydrothermal Wernecke Breccias; (2) 1.27 Ga, coincident with emplacement of the Bear River dykes and the Mackenzie dyke swarm; and (3) 1.15 Ga, coincident with the Grenville orogeny of eastern and southeastern Laurentia. The Grenville event is also evident in the northern and central North American Cordillera from scattered igneous and metamorphic ages, and is also recorded on other continents including Australia and South China. The 1.15 Ga event in northwestern Cordillera is rationalized by crustal heating in an extensional regime generated by the oblique convergence of the Yangtze Craton with the western margin of the joint Laurentia-Cathaysia landmass during the Late Mesoproterozoic.

Introduction

Xenoliths are valuable sources of information on the age and nature of the underlying lithosphere (e.g., Jefferson and Parrish, 1989; Davis, 1997; Davis et al, 2003; Canil, 2004; Harder and Russell, 2006). In the Wernecke Mountains of Yukon, Canada (Fig. 1), xenoliths are present in the Quartet Mountain Lamprophyres, a set of volatile-rich, ultramafic dykes of Cambrian age (Thorkelson et al., 2003; Milidragovic et al., 2006). The lamprophyres crosscut weakly-metamorphosed sedimentary strata of the Pinguicula Group and Wernecke and Mackenzie Mountains supergroups. The xenoliths were derived from a wide range of depths extending from the mantle to the upper crust.

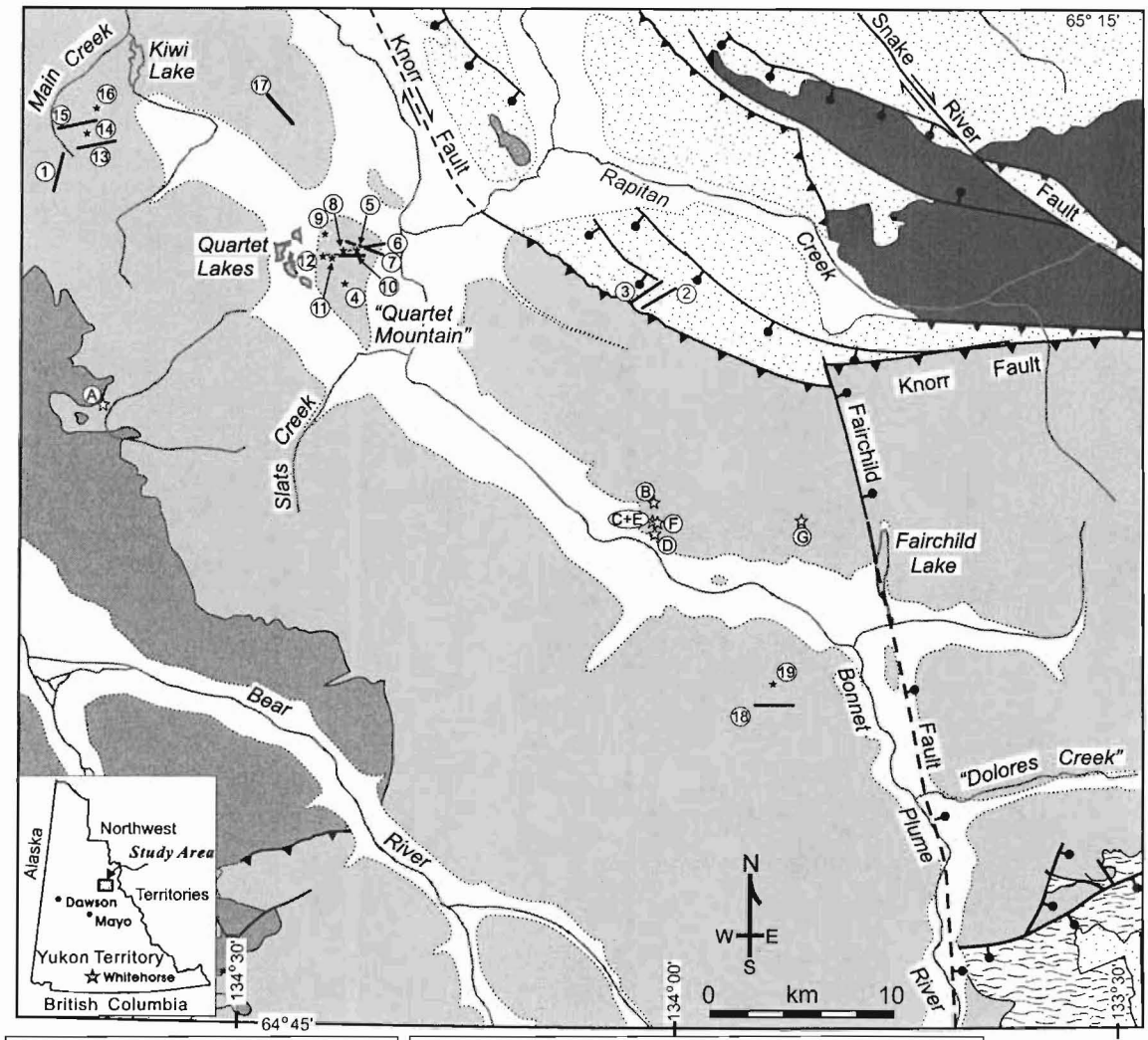

STRATIFIED ROCKS

QUATERNARY
- Alluvium, colluvium, glacial deposits

CAMBRIAN TO DEVONIAN
- Carbonates and clastics

UPPER PROTEROZOIC TO CAMBRIAN
- Vampire/ Backbone Ranges

UPPER PROTEROZOIC
- Windermere Supergroup

MIDDLE TO UPPER PROTEROZOIC
- Mackenzie Mountains Supergroup

MIDDLE PROTEROZOIC
- Pinguicula Group

LOWER PROTEROZOIC
- Wernecke Supergroup

INTRUSIVE ROCKS

- Quartet Mountain Lamprophyre: outcrop, float
- ⑲ Sample location - refer to Table 1 for more details

- Stratigraphic or intrusive contact: certain, approximate, inferred
- Fault: normal, reverse, strike-slip, inferred

Ar-Ar lamprophyre crystallization ages	
②	532±2.9 Ma
⑥	524±2.9 Ma
⑯	526.5±2.7 Ma
⑱	525±5 Ma

☆ Hydrothermal/metamorphic ages	
Ⓐ *JH02-12-1*	1178±6.1 Ma
Ⓑ *JH01-14-1a*	1135±5.5 Ma
Ⓒ *SB-94-1-345.1m*	996.7±8 Ma
Ⓓ *JH-01-27-3D*	1052±10 Ma
Ⓔ *SB-94-1-6m*	1113±5 Ma
Ⓕ *DT-95-2B*	980±4 Ma
Ⓖ *DT-93-22-1*	778±8 Ma

Figure 1. Geological map of the study area showing locations of the Quartet Mountain lamprophyres. Also shown for reference are the Late Mesoproterozoic/ Early Neoproterozoic hydrothermal/metamorphic ages reported by Hunt (2004; locations A-E) and Thorkelson et al. (2005; locations F and G). Map modified from Schwab and Thorkelson (2000), Gordey and Makepeace (2003), Thorkelson et al. (2005) and Milidragovic et al. (2006).

This paper provides new age and geochemical information on the Quartet Mountain Lamprophyres and on five of the crustal xenoliths from one of the lamprophyres. The xenoliths were examined using petrography, scanning electron microscopy, and Nd isotope geochemistry. U-Pb ages of zircon grains extracted from the xenoliths were determined by SHRIMP and interpreted with the aid of scanning electron microscopy. The results provide a unique glimpse into metamorphic and igneous processes in the crust of north-central Yukon. The data provide new constraints on the Middle and Late Proterozoic evolution of northwestern Laurentia, particularly during the time of Grenville orogenesis. The issue of Grenville-age activity along the west coast of Laurentia is addressed and a tectonic model is presented.

Geological Background

The Wernecke Mountains of east-central Yukon are underlain by thick successions of deformed, weakly metamorphosed Proterozoic sedimentary rocks deposited during several extensional, basin-forming events between ca. 1.84 Ga and ca. 540 Ma (Young et al., 1979; Delaney, 1981; Thorkelson, 2000; Thorkelson et al., 2005). Sedimentation was interrupted by periods of orogenesis, exhumation, and magmatic and hydrothermal brecciation. In early Paleozoic time, the region was marked by further extension and dissection of the rifted margin into a broad carbonate-dominated area, called the Mackenzie-Ogilvie platform, and surrounding basins (e.g., Selwyn basin; Blackstone and Richardson troughs) dominated by siliciclastic sediments (Lenz, 1972; Cecile, 1982; Gordey and Anderson, 1993; Norris and Dyke, 1997). The Early Cambrian

Quartet Mountain lamprophyres were emplaced into the Mackenzie Platform at ca. 530 Ma (Milidragovic et al., 2006).

The Wernecke Supergroup, consisting of siliciclastic and carbonate strata, is the oldest exposed succession in the Wernecke Mountains. Its deposition likely began with attenuation of the inferred underlying crystalline basement following the assembly of northwestern Laurentia during the ca. 2.10-1.84 Ga Wopmay orogeny (Hoffman, 1980; Delaney, 1981; Hildebrand et al., 1987; Hall and Cook, 1998; Cook and MacLean, 2004), and prior to emplacement of the Bonnet Plume River intrusions at ca. 1.71 Ga (Thorkelson et al., 2001a). The Wernecke Supergroup was subsequently metamorphosed and subjected to at least three phases of deformation collectively termed the Racklan orogeny, overlain by subaerial post-Racklan Slab volcanics, and hydrothermally brecciated at ca. 1.60 Ga to form the Wernecke breccias (Thorkelson et al., 2005). Porphyroblasts of chloritoid and minor garnet in a foliated groundmass of quartz, chlorite and muscovite imply peak metamorphic temperatures of 450-500°C (Brideau et al., 2002; Laughton et al., 2005) for the exposed lower parts of the Wernecke Supergroup during the Racklan orogeny.

Extension in the Wernecke Mountains at ca. 1.38 Ga was accompanied by deposition of the Pinguicula Group, and marine volcanism and mafic sill emplacement as recorded by the Hart River volcanics and Hart River sills, respectively. Subsequently, the area was affected by a thermal pulse at ca. 1.27 Ga, recorded by the Bear River dykes (Thorkelson, 2000; Schwab et al., 2004), and veins at the Nor mineral occurrence (Parrish and Bell, 1987). Based on the

geochemistry, Nd isotopic composition and geochronology, Schwab et al. (2004) argued that the Bear River dykes are the western extension of the Mackenzie dyke swarm, the world's largest radiating dyke swarm.

Renewed subsidence at $\leq$1.0 Ga was accompanied by the deposition of the Mackenzie Mountains Supergroup in the Wernecke and Mackenzie Mountains of the northern Cordillera. Cook and MacLean (2004) correlated the Mackenzie Mountains Supergroup with the Shaler Supergroup on Victoria Island, Brock Inlier and Coppermine homocline. A characteristic feature of the Mackenzie Mountains Supergroup and correlative successions ("Sequence B" of Young et al., 1979) is an abundance of Grenville-age detrital zircon grains (ca. 1.25-1.00 Ga; Rainbird et al., 1992, 1997). This observation led Rainbird et al. (1992, 1997) to suggest that much of the sediment was carried by continental-scale river systems originating from the Grenville structural province, more than 3000 km to the southeast. This hypothesis is supported by the Grenvillian ages of detrital muscovite grains from the Mackenzie Mountains Supergroup (Thorkelson et al., 2005).

A period of contractional deformation termed the Corn Creek orogeny succeeded the deposition of the Mackenzie Mountains Supergroup (Eisbacher, 1978, 1981; Thorkelson, 2000), and may have led to significant uplift and exhumation in the study area (Thorkelson et al., 2005). The Neoproterozoic Windermere Supergroup was deposited with angular unconformity to disconformity on older Proterozoic rocks, over a time span of ca. 150-180 m.y. (Aitken, 1991; Aitken and McMechan, 1992; Ross and Villeneuve, 1997;

Thorkelson, 2000). Its deposition is widely regarded to reflect the break-up of a Neoproterozoic supercontinent and opening of the proto-Pacific ocean (Eisbacher, 1985; Bell and Jefferson, 1987; Ross, 1991; Young, 1995). Synsedimentary extensional faults, tholeiitic volcanic and intrusive rocks and conglomeratic deposits that characterize the early deposition of Windermere Supergroup provide clear evidence for syndepositional extensional tectonism (Eisbacher, 1981; Aitken, 1991; Ross, 1991; Mustard and Roots, 1997). The maximum age of deposition of the Windermere Supergroup is constrained by the ca. 779 Ma Tsezotene sills ($^{207}Pb/^{206}Pb$ baddeleyite; Heaman, unpublished data in Heaman et al., 1992) and a 777+2.5/-1.8 Ma quartz diorite plug (U-Pb zircon; Jefferson and Parrish, 1989), which have been chemically linked to the Little Dal basalt (Jefferson and Parrish, 1989; Dudas and Lustwerk, 1997), the uppermost member of the Mackenzie Mountains Supergroup (Gabrielse et al., 1973; Jefferson and Ruelle, 1986; Thorkelson, 2000).

The Quartet Mountain Lamprophyres

Lamprophyres in the Wernecke Mountains were first reported by Delaney (1981), subsequently noted by Laznicka and Gaboury (1988), Hulstein (1994), and Thorkelson et al. (2003), and examined in detail by Milidragovic (2005) and Milidragovic et al. (2006). The field information for all of the known lamprophyres is summarized in Table 1, and lamprophyre locations are shown in Fig. 1. These intrusions, termed the Quartet Mountain Lamprophyres (QML) by Thorkelson et al. (2003) consist of steeply dipping dykes, ranging in width from 15 cm to 2 m, and striking east to southeast. They are grey, brown weathering and porphyritic,

with phenocrysts of euhedral to anhedral phlogopite ± bladed diopside ± equant pseudomorphed olivine. Apatite phenocrysts are a minor constituent of some of the lamprophyres. With the exception of phlogopite and minor opaque minerals, the groundmass is pervasively altered, and includes carbonate, chlorite and clay.

Some of the lamprophyres contain xenoliths of both mantle and crustal lithologies, and xenocrysts of spinel and carbonate-pseudomorphed olivine. Importantly, granulite-grade, zircon-bearing gneiss xenoliths, discussed in the following sections were identified in one of the lamprophyres (sample 2; Table 1).

Geochemistry and Neodymium Isotope Systematics of the Quartet Mountain Lamprophyres

Analytical Techniques and Uncertainties

Five lamprophyres were selected for whole rock chemical analysis (samples 2, 6, 7, 16 and 18). Samples 2, 6 and 16 were also selected for Nd isotopic analysis. Three high grade, sillimanite-bearing xenoliths were analyzed for Nd isotopes together with the lamprophyre samples. With the exception of sample 2, whose xenoliths form the main body of this paper, the samples were selected on the basis of their freshness and geographic location. Selected samples, free of visible xenoliths and/or xenocrysts and amygdules were chipped and sawn to remove weathered surfaces.

Major and trace element concentrations of samples 2, 6 and 7 were analyzed at the ACTLABS commercial laboratory and are reported in Table 2. Major oxides and select trace elements were determined by fusion ICP-OES (inductively coupled plasma optical emission spectroscopy), and all other trace

elements including the rare earth elements (REE) were analyzed using ICP-MS (inductively coupled plasma mass spectrometry) or INAA (instrumental neutron activation analysis). Relative uncertainties at 95% confidence interval are less than 15% for most determinations, although uncertainties for Pb, Co, Sc, Ho, Tm, Yb and Lu exceed 20%. Major oxides for sample 18 were measured at X-ray Assay Laboratories by X-ray fluorescence spectrometry. Trace element determinations for sample 18 were carried out by ICP-MS at the University of Saskatchewan.

Neodymium isotopic compositions were determined at the University of Alberta Radiogenic Isotope Facility, using a NuPlasma multiple collector-ICP-MS. The samples were analysed in accordance with the analytical protocol outlined by Creaser et al. (1997), and the results are presented in Table 3.

Geochemical Results

Major and trace element geochemical data for five lamprophyre samples are given in Table 2. The major elements concentrations discussed in this section have been normalized to a volatile-free basis. However, it must be noted that the Quartet Mountain Lamprophyres are characterized by high volatile contents that range from 4.7% to 24.8%, with the highest volatile concentrations measured in sample 2, which is xenolith-rich. The measured volatile concentration of sample 2 likely reflects the combined effect of primary gas-rich magma and assimilation of carbonate-rich wallrock. Whole-rock Mg numbers characteristic of the suite, defined as $100xMg/(Mg+Fe)_{atomic}$, where all Fe has been converted to Fe^{2+}, range from 63 to 86. The suite is silica-undersaturated,

with SiO_2 contents that vary from 32.3% to 43.4 wt.%, and normative nepheline contents from 0.37 to 5.28 wt.%. The lamprophyres plot in the alkaline field on the total alkali vs. silica diagram (Irvine and Baragar, 1971; Le Maitre, 2002).

The Quartet Mountain Lamprophyres are enriched in all trace elements (Fig. 2) relative to the primitive mantle values of Sun and McDonough (1989). Notable features characteristic of the suite are pronounced negative K anomalies, positive Ta-Nb anomalies and strongly fractionated rare earth element (REE) patterns. The light REE (LREE) are strongly enriched relative to chondritic values (Sun and McDonough, 1989) with La_n=236-821, whereas the heavy REE (HREE) are only moderately enriched with Yb_n=7.3-11.0, resulting in high ratios of LREE to HREE (La/Yb_n=30-113). With the exception of high Rb concentrations in samples 16 and18, the lamprophyres are depleted of large ion lithophile elements (LILE) relative to the high field strength elements (HFSE), when normalized to primitive mantle concentrations. The xenolith-free samples have Ni and Cr concentrations between 412-591 ppm and 364-851 ppm respectively, whereas the xenolith-rich sample 2 is significantly more enriched in both, with Ni=774 ppm and Cr=1220 ppm.

The elevated Ni and Cr concentrations in sample 2 probably reflect the high abundance of mantle xenoliths and olivine xenocrysts in this sample. The highly fractionated REE patterns of the QML, combined with the enrichment of all REE relative to the primitive mantle indicate the presence of residual garnet in the mantle source. Even very small degrees of partial melting (<0.1%) of a primitive mantle source (Sun and McDonough, 1989) in the garnet stability field

cannot account for the high La contents (Fig. A3). Therefore, we infer that QML were derived from a LREE-enriched mantle source, at a depth lying within the garnet stability field.

The intrasuite geochemical variation cannot be ascribed to any single process, such as fractional crystallization or different degrees of partial melting of a common mantle source. Attempts of relating the measured major and trace element concentrations of the lamprophyres through fractional crystallization of the major phases (phlogopite, diopside, and olivine) were unsuccessful. Contamination of the lamprophyres by assimilation of both upper mantle and crustal rocks, along with deuteric and post-emplacement alteration of groundmass minerals are likely important causes of the observed compositional variability.

Neodymium Isotope Results

Three of the Quartet Mountain lamprophyres were analyzed for Nd isotopes (samples 2, 6 and 16) and their isotopic compositions are presented in Table 3 and shown graphically in Fig. 3 on a εNd vs Time graph. The εNd values at 530 Ma, the approximate crystallization age of the lamprophyres (see Ar-Ar Geochronology), are relatively juvenile and range form -1.5 to 1.9. Depleted mantle model ages (Goldstein et al., 1984), representing the minimum time of extraction from a depleted mantle source with a uniform Sm/Nd ratio, range from 1.11 to 1.22 Ga.

Sample 6, which is completely xenolith- and xenocryst-free, and therefore likely approaches the uncontaminated Nd isotopic composition of its mantle source, shows a nearly identical εNd_{530} to xenolith-rich sample 2. The REE, including Sm and Nd, are widely considered to be immobile under sub-lower amphibolite metamorphic conditions (Creaser et al., 1997). Contamination by assimilation of peridotite or crustal components, both of which are typified by Nd concentrations significantly lower than the very high Nd content of sample 2, is unlikely to have an important effect on its isotopic composition (cf. Mitchell, 1995). A binary mixing calculation using the Nd isotopic parameters determined from two sillimanite bearing xenoliths (9044 and 9048; Table 3) demonstrates that assimilation of 20 wt.% of highly evolved crustal material would lead to a corresponding change in the initial εNd of only -0.76.

An attractive, although not unique, hypothesis is that the proposed LREE enrichment of the source lithospheric mantle (see Geochemical Results), took place at ca. 1.2-1.1 Ga. This enriched, low Sm/Nd mantle reservoir then underwent partial melting to form the Quartet Mountain lamprophyres at ca. 530 Ma. This hypothesis assumes the lamprophyre source evolved from a reservoir resembling the depleted mantle (Goldstein, 1984) through a single episode of LREE enrichment and consequent decrease in Sm/Nd.

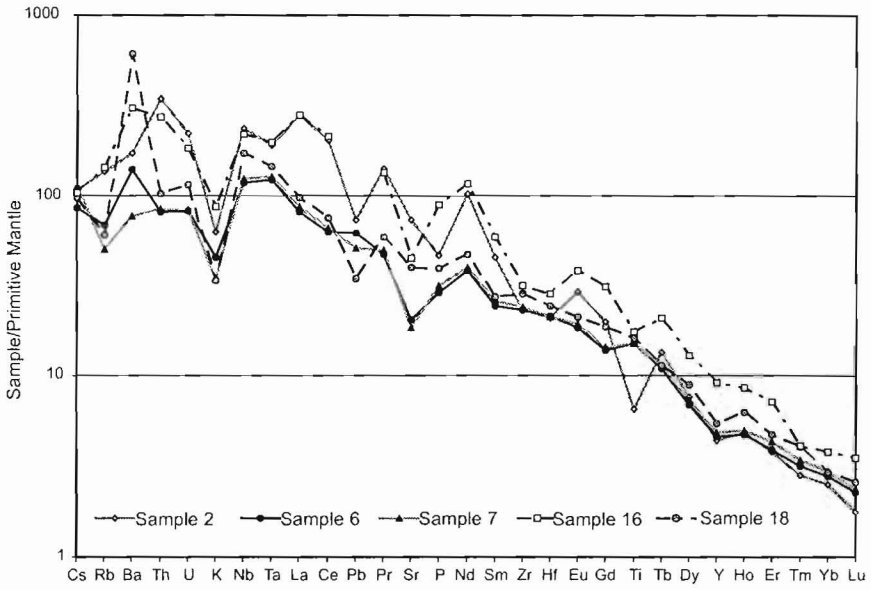

Figure 2. Primitive mantle (Sun and McDonough, 1989) normalized trace element profiles of the Quartet Mountain Lamprophyres.

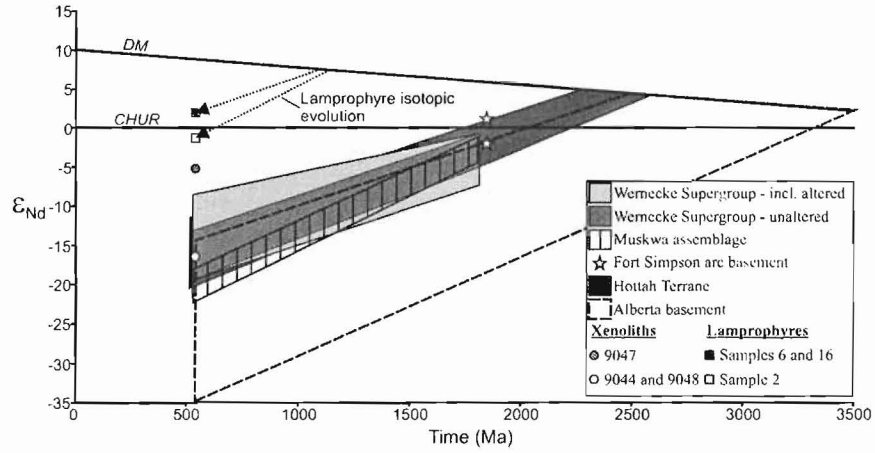

Figure 3. εNd vs Time diagram, showing the εNd values of xenoliths 9044, 9047 and 9048 at 530 Ma and the Nd isotopic evolution of the Quartet Mountain lamprophyres. Nd isotopic fields for Alberta basement and Muskwa assemblage (Ross et al.,2001), Hottah Terrane (Bowring and Podosek, 1989), and Wernecke Supergroup (Thorkelson et al., 2005) are shown for comparison. εNd values from two ca. 1845 Ma biotite granites, interpreted to represent the Fort Simpson basement (Villeneuve et al., 1991) are also shown. The depleted mantle (DM) curve is from Goldstein et al. (1984).

Classification of the Quartet Mountain Lamprophyres

The pervasive replacement of groundmass minerals makes the petrographic classification criteria outlined by Rock (1987, 1991), Le Maitre (2002) and Tappe et al. (2005) inapplicable in this case. Consequently, the lamprophyres were classified as ultramafic lamprophyres on the basis of their relative MgO, Al_2O_3 and CaO concentrations, metaluminous and ultramafic character, presence of normative nepheline and positive Ta-Nb anomalies (Rock, 1987; 1991). Furthermore, the comparison of trace element contents of the QML with published analyses of other lamprophyres worldwide highlights the similarities between the Quartet Mountain Lamprophyres and other ultramafic lamprophyres. The absence of "index" minerals, melilite, monticellite or alkali feldspar in the groundmass, possibly because of alteration, precludes further subdivision of the Quartet Mountain Lamprophyres into alnöites, aillikites and damtjernites (Tappe et al., 2005).

The ultramafic character, inequigranular texture and high phlogopite and olivine macrocryst content of sample 2 bears striking similarity to that of kimberlitic rocks (Mitchell, 1995). The dyke's mineralogy and texture are indistinguishable from reported mineralogical and textural characteristics of orangeites (Mitchell, 1995; Tappe et al., 2005). However, the sample's slightly negative initial εNd value is inconsistent with the strongly negative initial εNd values that are considered characteristic of orangeites, and which form the basis of the petrogenetic models for the rocks of the orangeite clan (Smith, 1983; Mitchell, 1995). The sample's high phlogopite phenocryst content is inconsistent

with the kimberlite classification. Furthermore, the low SiO_2/Al_2O_3 and MgO/CaO (Hamilton and Rock, 1990; Rock, 1991) ratios reflect higher phlogopite and clinopyroxene abundances in the Quartet Mountain Lamprophyres than typical of olivine-dominated kimberlites. Thus, despite its "kimberlitic" texture, sample 2 is best classified as an ultramafic lamprophyre.

Ar-Ar Geochronology

Samples and Methodology

Phlogopite phenocrysts from five lamprophyre dykes were selected for Ar-Ar geochronology. Sample locations are shown in Fig. 1 and were chosen on the basis of freshness and geographical location. Four of the samples were analyzed by the ^{40}Ar-^{39}Ar laser fusion technique at the Noble Gas Laboratory, Pacific Centre for Isotopic and Geochemical Research, University of British Columbia, Vancouver, BC, Canada (Table 4). Sample 18 was analyzed at the Geological Survey of Canada's Geochronology Laboratory (Table 5; Thorkelson, 2000; clarified by Thorkelson, 2003). The phlogopite fraction from sample 3 underwent a significant isotopic disturbance, and consequently did not yield a plateau age (Fig. 4b). Accordingly, we did not consider this sample in our interpretation of emplacement age.

$^{40}Ar/^{39}Ar$ results

The $^{40}Ar/^{39}Ar$ geochronological results constrain the timing of emplacement of the Quartet Mountain Lamprophyres to the Early Cambrian (Tables 4 and 5, Fig. 4). The plateau ages of 524.2 ± 2.9 Ma and 526.5 ± 2.7

from samples 6 and 16 respectively, in conjunction with the 522.5 ± 4.7 Ma age from sample 18, are identical within error. Xenolithic sample 2 yielded a slightly older plateau age of 532.2 ± 2.9 Ma. The narrow distribution of plateau ages from samples collected at different stratigraphic levels in the study area (Fig. 1) suggests that the ages signify emplacement rather than cooling associated with exhumation. It is unlikely that the Wernecke and Mackenzie Mountains supergroups were at the same relative crustal levels during the Early Cambrian emplacement of the lamprophyres. The Knorr Fault, which presently juxtaposes the Wernecke and Mackenzie Mountains supergroups in this area, is believed to be Cretaceous to Tertiary in age (Norris, 1997). This interpretation of the Ar-Ar ages is further supported by the lack of evidence for significant thermal history of the Mackenzie Mountains Supergroup carbonate that hosts sample 2, as evidenced by its very low metamorphic grade. From the available dataset it cannot be determined if (1) the emplacement of the Quartet Mountain Lamprophyres occurred over a period of ca. 10-15 m.y., (2) the lamprophyres were emplaced in at least two discrete pulses, or (3) the differences in Ar-Ar ages may simply reflect different cooling rates and closure temperatures (Dodson, 1973) among samples. The new $^{40}Ar/^{39}Ar$ dates are significantly younger than the two K-Ar dates of 552 ± 13 and 613 ± 15, reported by Delaney (1981). We consider the new dates to be more reliable, and hence interpret lamprophyre emplacement in the Early Cambrian.

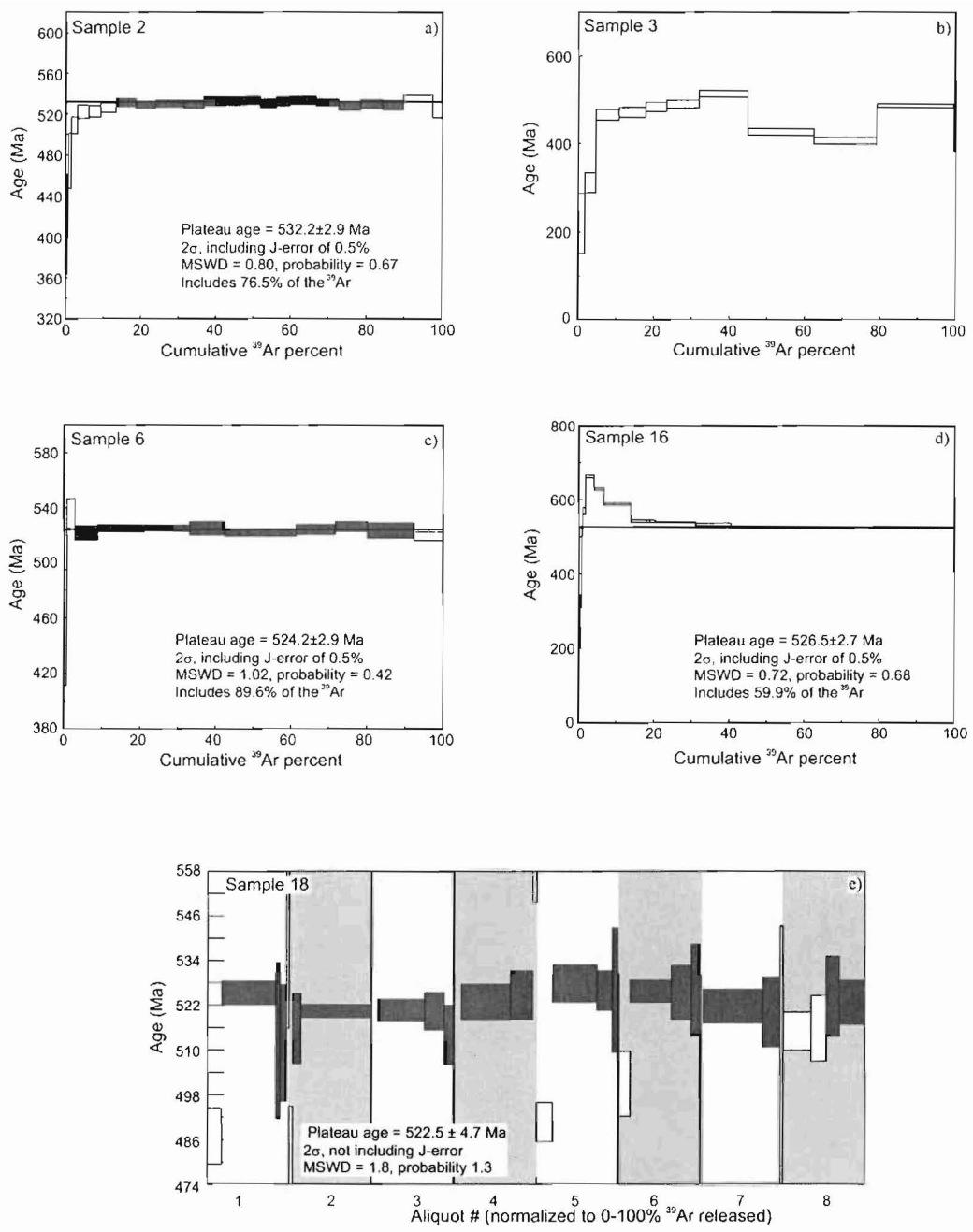

Figure 4. $^{40}Ar/^{39}Ar$ age spectra of igneous phlogopite from four Quartet Mountain Lamprophyres. Four samples (2, 6 and 16 and 18) yield well defined plateau ages. Shaded boxes signify release steps that were used in plateau age calculation. Box height represents 2σ error (Ma).

Regional Geological Setting of the Quartet Mountain Lamprophyres

The Quartet Mountain Lamprophyres belong to a suite of Paleozoic alkaline to ultrapotassic igneous rocks that extend from Canada's Arctic margin to southern British Columbia. These Cambrian to Late Devonian rocks occur as thin, laterally restricted volcanic piles and intrusions within the northern Cordilleran miogeocline and their genesis is probably linked to extension along the northern proto-Pacific margin (Pell, 1994; Goodfellow et al., 1995). The architecture of the miogeocline was largely inherited from Neoproterozoic rifting (Ross, 1991; Colpron et al., 2002; Harlan et al., 2003), which is widely thought to have led to the break-up of the supercontinent Rodinia and separation of the western Laurentia' s conjugate margin (e.g., Bell and Jefferson, 1987; Moores, 1991). Renewed extension in the Early Cambrian led to further rifting and division of the continental margin into deep clastic basins, flanked by shallow carbonate platforms.

In the study area, the Early Cambrian was marked by the development of the Mackenzie Platform (Lenz, 1972), an extensive, shallow, unevenly subsiding carbonate platform that formed the shelf facies of the Paleozoic northern Cordilleran miogeocline (Gordey and Anderson, 1993). In addition to the Quartet Mountain Lamprophyres, known Paleozoic igneous rocks in the Mackenzie-Ogilvie platform include the Early Silurian Coates Lake diatreme (McArthur et al., 1980; Godwin and Price, 1986), the Silurian Mountain, Bear and Stib diatremes (Godwin and Price, 1986) and the poorly studied Nash (Green, 1972), Tuk (Goodfellow et al., 1995) and Silurian volcanic rocks (unit Sv of Abbott, 1997).

In the Selwyn Basin, a major paleogeographic element which lies to the southwest of the Mackenzie Platform, volcanic episodes occurred in the Cambrian, Early to Middle Ordovician and Middle to Late Devonian (Cecile, 1982; Goodfellow et al., 1995). In British Columbia, alkaline diatremes, including carbonatites, kimberlites, lamproites, lamprophyres and nepheline syenites were emplaced during three major periods of rifting in the Late Ordovician to Silurian, Early Devonian and Late Devonian (Pell, 1994).

Early Cambrian emplacement of Quartet Mountain Lamprophyres was likely facilitated by the attenuation of the western Laurentian margin and the associated adiabatic decompression and melting of an LREE-enriched, hydrous mantle source. Although not unique, our favoured interpretation of the Nd isotopic data calls for the metasomatic enrichment of the upper mantle source at ca. 1.2-1.1 Ga, corresponding to an episode of zircon growth and recrystallization in four crustal xenoliths, as discussed below.

Petrology and Geochronology of the Crustal Xenoliths

Large xenoliths (>1 cm) of both crustal and mantle origins were identified in three lamprophyre samples. The mantle xenoliths are largely serpentinized and contain minor relict orthopyroxene. Crustal nodules characterized by greenschist or lower metamorphic grades, and likely derived from the immediate wallrock, dominate the crustal xenolith population. Rare, zircon-bearing xenoliths, typically preserving metamorphic conditions in excess of the metamorphic grades in rocks exposed at the surface (Brideau et al., 2002; Laughton et al., 2005) were identified in lamprophyre sample 2. In an attempt to gain insight into the nature of

the poorly understood deeper crustal levels that underlie east-central Yukon, a petrological and geochronological study of five xenoliths from sample 2 was conducted. The xenoliths were studied in detail using a combination of standard petrography, Nd isotope geochemistry and U-Pb zircon geochronology. These xenoliths were chosen over others because of their relatively large size, high-temperature mineral assemblages, including the sillimanite + garnet + K-feldspar assemblage that is consistent with granulite-facies metamorphism and high abundance of relatively large, zoned, inclusion-free zircon. Three of the five xenoliths retain prograde metamorphic assemblages that include sillimanite, garnet and K-feldspar. Two of the xenoliths have undergone retrograde metamorphism and their peak P-T conditions are not evident.

U-Pb Geochronology

Zircon grains were analyzed at the J.C. Roddick Ion Microprobe Laboratory in Ottawa, using the second generation sensitive high resolution ion microprobe (SHRIMP II). U-Pb age determinations on ~9 × 12 um diameter spots were performed following standard operating procedures (Stern, 1997). Analyses were run at 22 minutes each, during which time 7 scans were performed. The calibration correcting for the instrumental bias in the measured Pb/U was performed by multiple repeat measurements of $^{206}Pb^{+}/^{238}U^{+}$ and $^{254}[UO]^{+}/^{238}U^{+}$ of the 559.0±0.2 Ma z6266 zircon standard (Stern and Amelin, 2003). Within-session errors were evaluated by analyzing the standard every fourth or fifth analysis. Errors assigned to SHRIMP U-Pb ages were determined by the data reduction program "SQUID" (Ludwig, 2001a). Overall, 61 analyses from 49 zircon

grains were obtained during a single analytical session totalling ~40 hrs. The choice of spot locations was based on zircon quality and relative absence of inclusions, textural relationships that were identified using cathodoluminescence (CL) imagery and the requirement that analytical spots be located within a single domain. Complete zircon U-Pb data are presented in Table 6, and concordia plots are shown in Fig. 5. Cathodoluminescence photomicrographs of selected zircon grains are shown in Fig. 6. All errors reported in this and the following sections are given at the 95% confidence level (2σ).

Xenolith 9044

Xenolith Petrography

Xenolith 9044 is a finely banded, garnet-sillimanite-quartz paragneiss, with minor alteration to sericite and carbonate. The xenolith is dominated by thin bands (<2 mm) composed of quartz porphyroblasts set in a fine-grained matrix of granoblastic quartz, locally enveloped by a thin hematite film, minor sillimanite and trace zircon and spinel. The quartz bands are separated by equally thin, discontinuous bands of garnet and sillimanite (Fig. A1). Thin lenses dominated by sericite, with subordinate hematite are present, although not ubiquitous. Submicroscopic, irregularly-shaped K-feldspar crystals, occurring interstitially to quartz, were identified using a scanning electron microscope (SEM) mounted with an energy dispersive X-ray analysis (EDAX) spectrometer. The observed metamorphic assemblage of xenolith 9044 implies high temperature and moderate pressure upper amphibolite to granulite facies metamorphism of an aluminous wacke protolith.

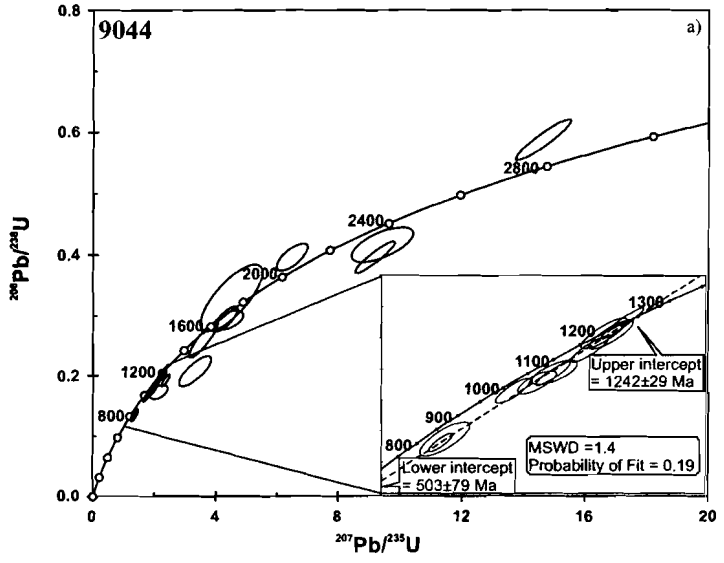
9044
a)
Upper intercept
= 1242±29 Ma
MSWD =1.4
Probability of Fit = 0.19
Lower intercept
= 503±79 Ma
$^{206}Pb/^{238}U$
$^{207}Pb/^{235}U$

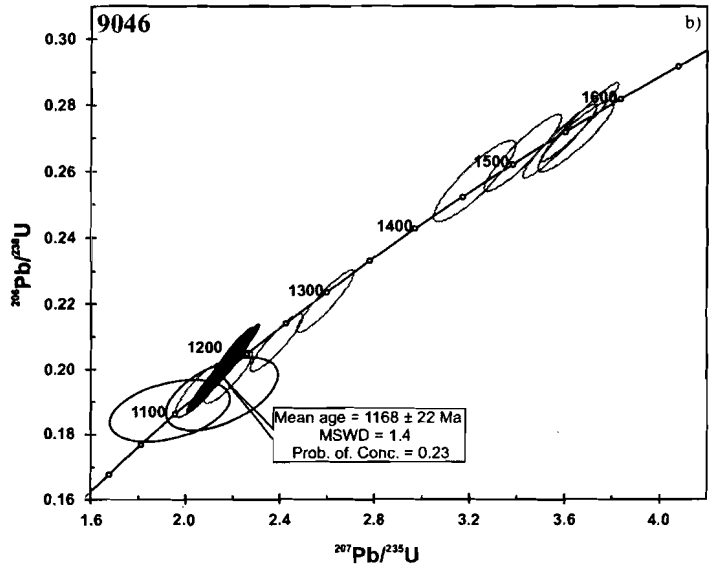
9046
b)
Mean age = 1168 ± 22 Ma
MSWD = 1.4
Prob. of Conc. = 0.23
$^{206}Pb/^{238}U$
$^{207}Pb/^{235}U$

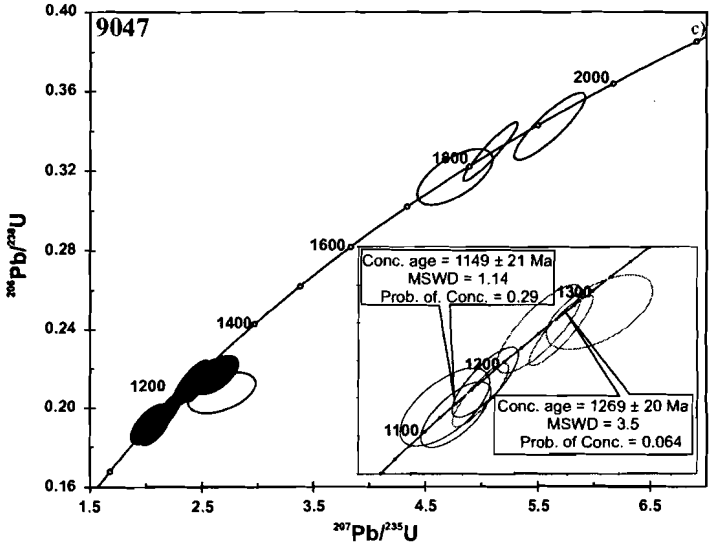
9047
c)
Conc. age = 1149 ± 21 Ma
MSWD = 1.14
Prob. of Conc. = 0.29
Conc. age = 1269 ± 20 Ma
MSWD = 3.5
Prob. of Conc. = 0.064
$^{206}Pb/^{238}U$
$^{207}Pb/^{235}U$

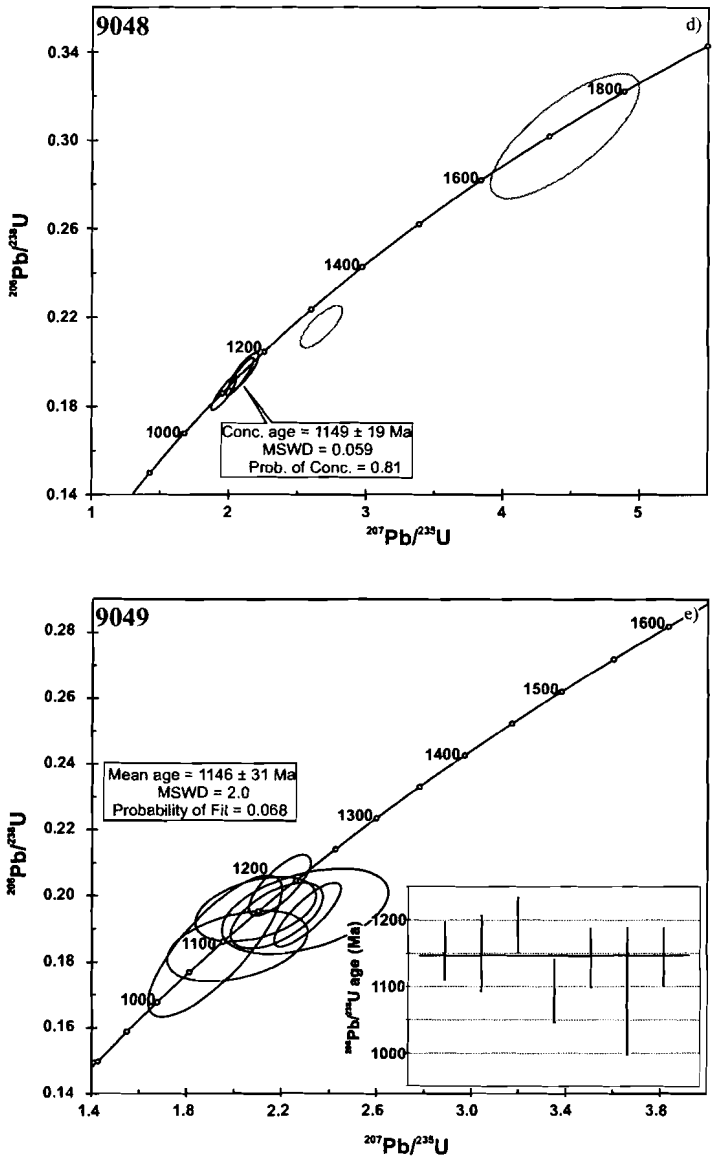

Figure 5. Concordia plots of SHRIMP U-Pb data from xenoliths 9044, 9046, 9047, 9048 and 9049 (ellipses at 2σ). Interpreted ages are shown on individual plots. **a)** Concordia plot of 21 analyses obtained from xenolith 9044. Empty ellipses represent data obtained from detrital zircon cores. Filled ellipses correspond to the homogenous, weakly luminescent metamorphic domains. **Inset:** enlarged view of the data obtained from the homogenous, weakly luminescent domains. **b)** Concordia plot of 17 determinations from xenolith 9046. Empty ellipses symbolize data obtained from zircon cores; filled ellipses correspond to data obtained from the high U (>2000 ppm) metamorphic domains. **c)** Plot of 11 SHRIMP analyses from xenolith 9047. Empty ellipses correspond to analyses of zoned zircon cores. Light grey-filled ellipses represent analyses from low Th/U recrystallized domains formed during the ca. 1.27 Ga metamorphic event. Black-filled ellipses represent the highly luminescent rims formed at ca. 1.15 Ga. **Inset:** An enlarged view of the analyses corresponding to the ca. 1.27 Ga and ca. 1.15 Ga metamorphic events. **d)** Concordia diagram of 5 analyses from xenolith 9048. **e)** Plot of 7 analyses obtained from xenolith 9049. **Inset:** $^{206}Pb/^{238}U$ ages of the analyzed domains. Error bars represent 2σ uncertainty.

The garnet grains are irregular in shape and have abundant fractures generally lined with iron-oxides and sericite. Garnet composition was determined by electron microprobe, as 64 % almandine and 34% pyrope, with a minor grossular component. Sillimanite grains are irregular, approximately 0.05 mm across and set in a K-feldspar groundmass. Rutile, zircon and titanite are important accessory phases, and occur either as interstitial grains, or as mineral inclusions within quartz or garnet. Zircon crystals are largely oriented with c-axes parallel to the foliation direction.

Petrographic examination of the xenolith suggests a complex history of prograde and retrograde metamorphism, and metasomatic alteration during entrainment in the lamprophyre melt. The identification of sillimanite and microscopic K-feldspar crystals, and lack of prograde muscovite, provides evidence that the prograde metamorphism may have taken place under granulite-facies conditions, above the second-sillimanite isograd. The retrograde metamorphic reaction

$$\text{Sillimanite} + \text{K-feldspar} + H_2O \rightarrow \text{Muscovite} + \text{Quartz}$$

(e.g., Spear and Chaney, 1989) under upper amphibolite-facies conditions is thought to have produced the observed assemblage and led to nearly complete consumption of K-Feldspar. Carbonate-filled veinlets, some terminating at the xenolith-lamprophyre contact are locally abundant and thus likely represent carbonate-rich fluids derived from the lamprophyre magma.

The observed zircon orientation indicates syn-kinematic rotation of the detrital zircon cores, but does not provide definite evidence for syn-kinematic

recrystallization or growth of metamorphic rims. Although it is likely that the growth and recrystallization of zircon date the peak metamorphic conditions (i.e. the development of the prograde assemblage), this assignment is equivocal.

Xenolith Geochronology

Twenty-one SHRIMP analyses were conducted on 19 of more than 100 zircon grains from xenolith 9044. The zircon grains are largely rounded to sub-rounded, and show a wide range in both grain size (10 μm-100 μm) and crystal habit (equant to elongate). CL and BSE imaging reveals the complexity of the zoning, and highlights various textural features including: highly luminescent, commonly oscillatory-zoned cores, interpreted as detrital zircon grains of probable igneous origin; weakly luminescent, subtly-zoned cores, likely representing detrital zircon of igneous or metamorphic origin; sharply-truncated domain boundaries indicative of dissolution and/or recrystallization; weakly luminescent unzoned or sector-zoned crystals; and homogenous, weakly luminescent outer rims representing post-depositional metamorphic zircon growth (Fig. 6 a-c; Fig. A5).

The analyzed cores are generally highly discordant, and show a wide range of $^{207}Pb/^{206}Pb$ ages from neo-Archean to Mesoproterozoic. The high degree of discordance and low precision of some of the analyses presents a challenge in establishing the minimum age of detrital zircon in the rock and hence a maximum depositional age of the sedimentary protolith (Fig. 5a). Most of the age determinations for the cores are interpreted to be older than ~1.71 Ga, which is regarded as the minimum depositional age of the Wernecke

Supergroup, the oldest exposed rock unit in the Yukon (Thorkelson et al., 2001a, 2005). Two analyses (19.2 and 52.1) were made on oscillatory, albeit diffusely-zoned cores and yielded younger discordant ages of ~1.41 Ga. Although this age could represent a maximum for deposition of the sedimentary protolith, the diffuse zoning and discordance of the analyses may indicate partial recrystallization and Pb-loss from these cores during the metamorphic event discussed below. As such, these cores do not constrain the age of the sedimentary protolith. Based on the permissible analytical data, we tentatively interpret the age of xenolith 9044 to be $\geq$ 1.71 Ga, thus implying a Wernecke Supergroup or older source.

The weakly luminescent rims and rare single domain crystals (e.g., 9044-1) are characterized by moderate to high U contents (648-2231 ppm) and low Th/U ratios (0.07-0.01), characteristic of metamorphic zircon (Rubatto and Gebauer, 2000). On a concordia plot, the analyses from these domains lie along a well-defined discordia line with upper the intercept age of 1242±29 Ma and the lower intercept age of 503±79 Ma. The upper intercept is interpreted to signify a metamorphic event that caused partial recrystallization of detrital zircon cores (see discussion above), and growth of new weakly luminescent, high U, low Th/U zircon. The lower intercept is identical to, within error, the crystallization age of host lamprophyre DT-02-12-1-4, and likely signifies the fluid-facilitated remobilization of radiogenic Pb associated with heating of xenolith during entrainment.

Xenolith 9046

Xenolith Petrography

Xenolith 9046 is a green, banded rock that has been extensively altered. A foliated texture is manifested by lenses composed dominantly of sericite, surrounded by a matrix of coarse crystalline to very fine carbonate and chlorite (Fig. A1). A relatively sericite-poor band, approximately 1.3 mm wide, contains abundant (>10%) anhedral, fractured crystals of equant apatite (<0.3 mm across). Apatite grains show no indication of alteration along the fractures. In addition to apatite, the band is composed of euhedral sparry carbonate and chlorite mats, both of which are likely pseudomorphs after unidentified minerals.

The extensive retrograde metamorphism / metasomatic alteration makes the interpretation of the protolith of xenolith 9046 difficult. Based on its high sericite content and zircon geochronology (see Discussion), we speculate that xenolith 9046 was derived from an aluminous sedimentary protolith, although, based on strictly mineralogical arguments, a felsic peraluminous igneous protolith cannot be precluded.

Xenolith Geochronology

Seventeen SHRIMP determinations were performed on 13 zircon crystals from xenolith 9046. The separated grains have rounded to sub-rounded crystal faces, equant to elongate habits and range in size from ~30 to 70 μm in the long-axis direction. CL imaging identified cores, characterized by diffuse, irregular, variably luminescent zoning; homogenous weakly luminescent whole grains or rims of inferred metamorphic origin; and highly luminescent, sector-zoned cores

(Fig. 6 d-f; Fig. A6). BSE imaging revealed that many of the zircon grains are fractured and every effort was made to position analyses far from these fractures. All of the determinations are less than 8% discordant.

The oldest analyzed core domain yielded a $^{207}Pb/^{206}Pb$ age of 1582±28 Ma (Fig. 5b). Five of the analyzed cores produced $^{207}Pb/^{206}Pb$ ages in the range between 1445±38 Ma and 1582±28 Ma. Four other cores yielded significantly younger ages, with the youngest one having a $^{206}Pb/^{238}U$ age of 1141±38 Ma. With the exception of analysis 6.1 (U=692 ppm), the five older cores are characterized by high and uniform U contents (1430-1480 ppm). All five cores have low Th/U ratios (0.00-0.02).

Similar U-contents and Th/U ratios, blurred, convoluted zonation, of the five older zircon cores are consistent with growth at a common time (>ca. 1582 Ma), followed by variable loss of radiogenic Pb during subsequent recrystallization. The four younger cores may have a similar history but with greater degrees of recrystallization and associated radiogenic Pb-loss. They are characterized by highly diffuse cathodoluminescence and lower U contents (576-868 ppm), which may indicate a more complete purging of the non-essential structural constituent cations (Hoskin and Schaltegger, 2003), or simply reflect the coarse-scale heterogeneity typical of the cores (e.g., Fig. 6e). Alternatively, these cores may reflect a population of detrital cores that has undergone complete loss of radiogenic Pb: at >ca. 1582 Ma, followed by a more recent episode of variable loss. The age of the Pb-loss is considered to be

approximated by the age of the youngest core, i.e., 1141±38 Ma, based on its near-concordant $^{206}Pb/^{238}U$ age.

Analyses from zircon rims and individual grains support the interpretation of a metamorphic event at ca. 1150 Ma. Six analyses of unzoned, weakly luminescent, high U single grains and rims were carried out. The analyzed spots are characterized by low Th/U (0.07-0.1) and very high U contents (2170-3828 ppm). Despite the high U concentrations, no signs of radiation damage or metamictization were observed within these domains. All six analyses are ≤5% discordant and are identical within error, yielding a $^{206}Pb/^{238}U$ weighted mean age of 1184±15 Ma. In addition, two highly luminescent, high Th/U (0.12-0.20), very low U (222-260 ppm), diffuse sector-zoned cores yielded imprecise $^{206}Pb/^{238}U$ ages of 1106±42 Ma and 1134±50 Ma. These cores are unlikely to be genetically related to the weakly-luminescent, high-U domains, but may reflect zircon re-equilibration with late stage metamorphic fluids. Combined determinations from the six high-U rims, two low-U cores, and two youngest low-Th/U cores yields a $^{206}Pb/^{238}U$ weighted mean age of 1168±22 Ma, which represents the best age-estimate of the metamorphic event recorded by xenolith 9046.

Xenolith 9047

Xenolith Petrography

Xenolith 9047 is an irregularly banded sillimanite-bearing paragneiss, largely composed of lenses of sericite juxtaposed against lenses of chlorite closely intergrown with microcrystalline potassic feldspar. Within the chlorite-potassic feldspar lenses, very fine, massive to acicular, crystals of celestite (Sr,

Ba) SO_4 were identified using scanning electron microscopy. Single grains or lenses of fine (0.1-0.2 mm), granoblastic, potassic feldspar, showing sericite alteration along the margins are generally isolated, but locally occur in association with sillimanite. Sillimanite is fine grained (<0.1 mm), forming discontinuous lenses, although it also occurs as single grains intergrown with rutile, within garnet poikiloblasts. Garnet porphyroblasts are anhedral and highly fractured, and contain significant rutile and opaque inclusions. Zircon crystals are minor constituents of xenolith 9047. A large veinlet, locally 0.2 mm wide and composed largely of fine-grained to sparry carbonate cross-cuts the xenolith. The cross-cutting veinlet can be traced back to the lamprophyre, and thus, likely represents crystallized carbonate-rich fluid derived from the lamprophyre melt.

The mineralogy dominated by sericite and chlorite is interpreted to signify extensive retrograde metamorphism of a former garnet, sillimanite and K-feldspar-rich assemblage. Small regions of the xenolith, however, escaped significant retrogression, and likely still reflect maximum P-T conditions. As is the case with xenolith 9044, the high-temperature upper amphibolite to granulite-facies metamorphism of xenolith 9047 cannot be unequivocally equated to the timing of metamorphism recorded by zircon growth and recrystallization.

Xenolith Geochronology

Eleven U/Pb isotopic determinations were made from eight zircon crystals separated from xenolith 9047. The zircon grains from xenolith 9047 are typically well rounded, and range in habit from equant to highly elongate. The grains range in size from 30 to 60 μm in the long dimension. BSE and CL imagery

revealed a variety of textural elements that included: detrital cores characterized by sharp oscillatory zoning suggesting igneous genesis; diffuse domains of inward-directed recrystallization characterized by moderate luminescence; and the outermost highly luminescent, homogenous zircon rims representing the youngest episode of metamorphic growth.

Four cores, including three with oscillatory zonation, were analyzed. All 4 cores are characterized by comparatively low U contents (213-425 ppm) and high Th/U (0.26-0.55). Three core analyses are near-concordant, with the youngest core yielding a $^{207}Pb/^{206}Pb$ age of 1781±82 Ma (Fig. 5c), therefore defining the maximum age of the sedimentary protolith of xenolith 9047. The high degree of discordance calculated for analysis 37.2 (19%), is attributed to isotopic disturbance associated with one of the two events discussed below.

Analyses of four diffuse, cloudy domains, characterized by moderate luminescence demonstrated uniform U concentrations (450-575 ppm) and Th/U ratios (<0.02). These domains mantle older, typically oscillatory-zoned cores, while preserving the original zircon morphology and are interpreted to represent inward-directed sub-solidus recrystallization (Corfu et al., 2003). Three of the analyses are identical within error and yield a concordia age (Ludwig, 2001b) of 1269±20 Ma, thus recording the same metamorphic event as xenolith 9044. The younger analysis 37.3 is interpreted to have undergone radiogenic Pb-loss during the youngest thermal event that generated the highly luminescent, outermost zircon rims.

The highly luminescent, outermost rims occur in many of the zircon grains separated from xenolith 9047, but only three were identified as suitable for SHRIMP analysis. The rims appear homogenous and are characterized by lower U concentrations (157-340 ppm), and variable Th/U (0.09-0.88). The contacts between the outermost rims and older domains are sharp and commonly straight, suggesting new zircon growth, rather than recrystallization of previously formed zircon. The analyses yield a concordia age of 1149±21 Ma and define the second episode of metamorphism recorded by xenolith 9047.

While performing analysis 37.1, a small volume (<20%) of the older, diffuse domain inferred to represent ca. 1270 Ma recrystallization that has undergone Pb-loss at ca. 1150 Ma was analyzed. Given the small extent of the overlap between the two metamorphic domains, and the near complete loss of radiogenic Pb from the recrystallized domain during the ca. 1150 Ma event as determined from analysis 37.3, we interpret analysis 37.1 as representative of the highly luminescent zircon growth at ca. 1150 Ma.

Xenolith 9048

Xenolith Petrography

Xenolith 9048 is a small paragneissic inclusion lacking evidence of banding. Its mineralogy is dominated by fine-grained, granoblastic heavily fractured crystals of sillimanite. The sillimanite crystals are approximately equant in shape, 0.3-1.2 mm long, and are closely intergrown. Sericite forms large, irregularly shaped mats within sillimanite and around heavily altered crystals of potassic feldspar. Volumetrically minor, coarse-grained, highly fractured garnet is

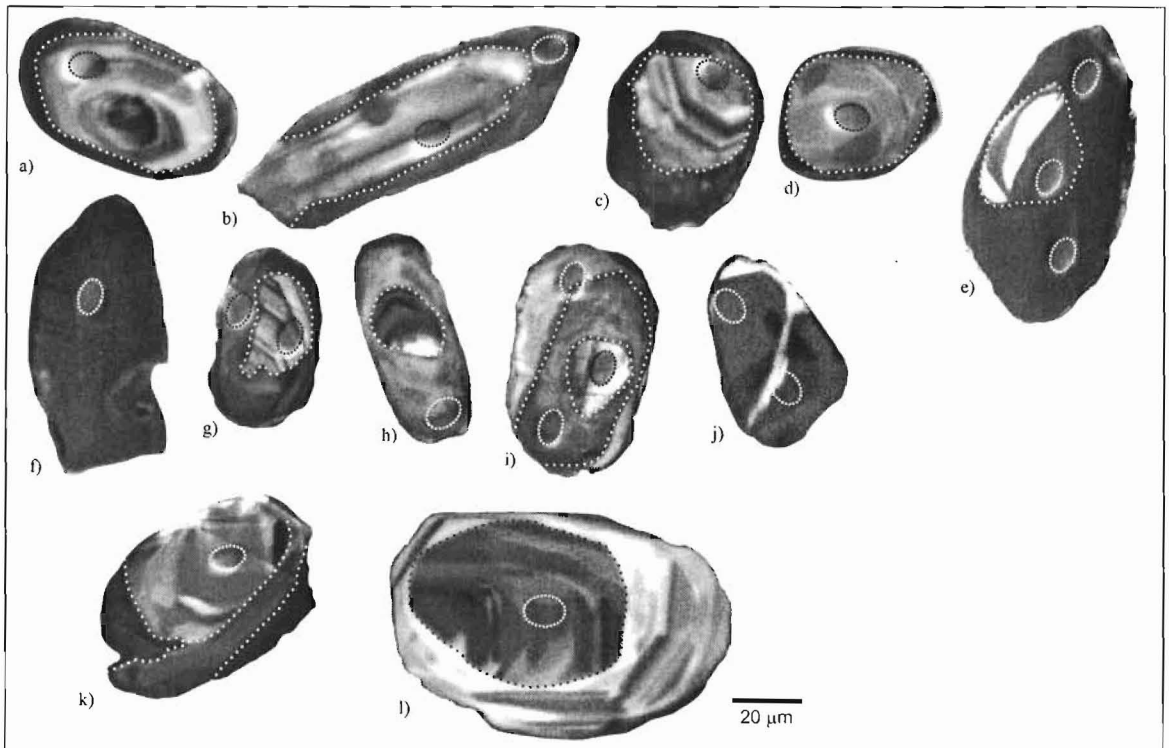

a) 9044-7; **b)** 9044-23; **c)** 9044-78; **d)** 9046-13; **e)** 9046-15; **f)** 9046-20; **g)** 9047-4; **h)** 9047-16; **i)** 9047-37; **j)** 9048-13; **k)** 9049-7; **l)** 9049-9

Figure 6. Cathodoluminescence photomicrographs of representative zircon grains from xenoliths 9044, 9046, 9047, 9048 and 9049. Positions of analysis pits are shown as dotted ellipses. Dotted lines delineate approximate domain boundaries. Greyscale was adjusted for each crystal to maximize contrast, and is hence only relative. **a-c)** Zircon crystals from xenolith 9044. Dark, weakly luminescent metamorphic rims mantle inherited detrital cores, which commonly display oscillatory zoning and brighter luminescence (a and c). **d-f)** Zircon crystals from xenolith 9046. **d)** Very thin, weakly luminescent rim mantling a very low U (222 ppm) sector-zoned core. **e)** An irregularly zoned core showing both weakly and strongly luminescent domains, surrounded by a weakly luminescent, homogenous metamorphic rim. **f)** A homogenous, very weakly luminescent grain, similar in composition and age to the rim in e). **g-i)** Zircon grains from xenolith 9047. **g)** Highly luminescent, oscillatory-zoned, irregularly-shaped detrital core of igneous origin, enclosed by a slightly less luminescent metamorphic rim, representing the second episode of metamorphism recorded by xenolith 9047. **h)** An elongate, originally oscillatory-zoned zircon crystal, that has undergone inward-directed recrystallization, and effective chemical homogenization that obliterated most of the initial zoning during the 1st metamorphic episode recorded by xenolith 9047. **i)** A zircon crystal displaying a nearly euhedral habit and prismatic terminations, that has undergone recrystallization associated with the initial metamorphic event. A subsequent metamorphic episode led to the growth of the more highly luminescent outer rim. **j)** Weakly luminescent, unzoned zircon crystal from xenolith 9048. A highly luminescent, recrystallization vein cross-cuts the zircon. The vein was accidentally sampled by analysis 13.2. **k-l)** Zircon crystals from xenolith 9049. **k)** A complexely zoned zircon crystal. The age relationships between the dark grey and black domains cannot be determined with confidence. **l)** Oscillatory-zoned zircon crystal with a recrystallized rim in which the oscillatory zoning is only faintly preserved.

locally intergrown with sillimanite ± K-feldspar and pervasively replaced by sericite and chlorite. Other important minor mineral phases include rare zircon crystals, irregularly shaped rutile and minor opaques.

Xenolith 9048 appears to have been formed through upper amphibolite to granulite-facies metamorphism of an aluminous wacke protolith, which underwent subsequent retrogression. Extensive retrograde metamorphism of the xenolith is evident from extensive replacement of potassium feldspar and sillimanite by sericite (Fig. A1), and the alteration of garnet to sericite and chlorite. As is the case with the other paragneiss xenoliths, the timing of metamorphism cannot confidently be linked to the observed prograde mineral assemblage.

Xenolith Geochronology

Due to the very small grain size and relatively complex zoning of the zircon grains recovered from xenolith 9048, only five analyses from four grains were carried out. The zircon grains are dominantly equant in shape, with irregular to rounded grain boundaries. The four analyzed zircon grains are 20-40 μm in diameter.

Two of the zircon crystals contain diffusely zoned cores that underwent partial recrystallization. Analysis 10.1 returned an imprecise $^{207}Pb/^{206}Pb$ age of 1747 ±118 Ma that constrains the maximum age of xenolith 9048. The analysis of the second core produced a highly discordant result, which did not permit a meaningful interpretation.

The other three analyses were obtained from featureless, weakly luminescent, high U (>1000 ppm), low Th/U (<0.10) zircon, interpreted to be of metamorphic origin. The analyses returned $^{206}Pb/^{238}U$ ages that overlap within error and range from 1100 to 1153 Ma (Fig. 5d). Analysis 13.2, however, was partially positioned over a strongly luminescent, cross-cutting feature, interpreted to represent a late recrystallization vein within the zircon crystal, and thus texturally-younger than the metamorphic domains. Hence, the analysis underestimates the true crystallization age of the metamorphic domain and was therefore excluded from the age determination for the U-rich domains. The remaining two points yield a concordia age (Ludwig, 2001b) of 1149±19 Ma, corresponding to the time of metamorphic growth.

Xenolith 9049

Xenolith Petrography

Xenolith 9049 is an ovoid nodule of finely laminated, green and white gneiss. At 3 cm long, it is the largest xenolith encountered. The texture of the xenolith is dominated by discontinuous lenses of polygonal, very fine grained feldspar partially altered to chlorite, and lenses and laminae of carbonate, sericite, chlorite and a dark brown material inferred to be an extremely fine grained aggregate of carbonate, chlorite, sericite and clay. Lenses of fine grained feldspar frequently contain larger, irregularly shaped feldspar crystals that are commonly characterized by undulose extinction. EDAX determinations of feldspar grains have shown that they are Ca^{2+} free, and of approximate $Ab_{90}Or_{10}$ composition. Many of the lenses are likely boudins formed by tensional

deformation of formerly continuous compositional bands. An important mineralogical aspect of xenolith 9049 is the presence of coarse (>4 mm), relict crystals of Mg-rich orthopyroxene. The orthopyroxene has been in large part replaced by a Ca-Mg-Fe rich carbonate, opaque minerals, chlorite and a brown aggregate of an unidentified microcrystalline mineral. Phlogopite pseudomorphism of orthopyroxene is evident. Furthermore, randomly-oriented phlogopite grains are scattered throughout the xenolith. A carbonate veinlet, approximately 1 mm wide cross-cuts the xenolith.

The xenolith has undergone extensive retrograde metamorphism, and has in part reacted with the lamprophyre magma, as evidenced by the carbonate veinlet, growth of post-kinematic unaligned phlogopite and phlogopite pseudomorphism of orthopyroxene (Fig. A1). It appears that orthopyroxene may once have formed a mono-mineralic band within the xenolith at least 0.5 mm thick.

The combination of prograde metamorphism, deformation, retrograde metamorphism and metasomatic alteration during entrainment, hampers the identification of the xenolith's protolith. Based on the presence of Mg-rich orthopyroxene, absence of quartz, relatively low abundance of aluminosilicate phases and absence of detrital zircon grains (see U-Pb geochronology section), xenolith 9049 is interpreted as a silica-undersaturated orthogneiss.

Xenolith Geochronology

Seven analyses were obtained from five zircon crystals from xenolith 9049. The analyzed grains are equant to elongate in shape with irregular to

rounded grain boundaries and range in size from ~50-100 μm in long dimension. CL images of the analyzed grains show complex textural relationships (Fig. 6 k-l; Fig. A9). Highly luminescent domains commonly displaying diffuse, relict oscillatory zoning mantle or cross-cut zircon domains characterized by oscillatory zoning and weaker luminescence. The highly luminescent domains are interpreted to represent sub-solidus recrystallization (Rubatto and Gebauer, 2000) of pre-existing oscillatory-zoned igneous domains. All analyzed domains have elevated Th/U (0.4-2.3) and U contents less than 500 ppm, with all but one domain containing <230 ppm U. As a consequence of low U contents, the individual age determinations are accompanied by large uncertainties. The $^{206}Pb/^{238}U$ ages derived from all seven analyses range from 1093 Ma to 1192 Ma (Fig. 5e), and yield a weighted mean age of 1146±31 Ma. The ages obtained from the partially recrystallized domains and the non-recrystallized oscillatory-zoned domains are identical within error, and are consequently taken to signify a single thermal event or two closely spaced thermal events at ca. 1150 Ma.

Nd Isotope Geochemistry of the Xenoliths

Sillimanite bearing xenoliths, 9044, 9047 and 9048 were analyzed for Neodymium isotopes at the University of Alberta Radiogenic Isotope Facility. Their isotopic compositions are significantly less radiogenic than the chondritic uniform reservoir (CHUR; DePaolo and Wasserburg, 1976), having present day εNd values that range from -11 to -23. Depleted mantle model ages of the xenoliths range from 1.7 to 2.4 Ma. We interpret the relatively high $^{143}Nd/^{144}Nd$ ratio and the relatively young depleted mantle model age of xenolith 9047 to be

meaningless, and to reflect the contamination of the xenolith by approximately 10 wt.% of the more radiogenic, high Nd lamprophyre magma (Fig. A4). This interpretation is substantiated by the identification of the 0.2 mm wide veinlet that crosscuts the xenolith.

$^{143}Nd/^{144}Nd$ and depleted mantle model ages of xenoliths 9044 and 9048, are indistinguishable from those of the Wernecke Supergroup (Thorkelson et al., 2005), the Hottah Terrane (Bowring and Podosek, 1989), the Fort Simpson "arc" (Villeneuve et al., 1991), the Muskwa assemblage and the Alberta basement (Ross et al., 2001) (Fig.3).

Discussion

Discussion of Protolith Ages

The study of the Quartet Mountain lamprophyre xenoliths was, in large part, driven by their evidence of upper amphibolite to granulite- facies metamorphism, which is significantly higher than the maximum regional greenschist metamorphism observed in the schist belts of the Fairchild Lake Group (FLG; Delaney, 1981; Thorkelson et al., 2005). The greenschist-facies metamorphism of FLG resulted in peak temperatures of 450-550 °C (Brideau et al., 2002; Laughton et al., 2005). In contrast, the sillimanite and potassium-feldspar bearing mineral assemblage of xenoliths 9044, 9047 and 9048, is consistent with the reaction

Muscovite + Quartz → Sillimanite + K-Feldspar + H_2O,

thus, implying minimum metamorphic temperatures of ~600 °C (Fig. A11).

Imprecise and discordant SHRIMP data from detrital zircon cores from the paragneissic xenolith 9044 do not allow for an unequivocal interpretation of the age of its protolith. However, the analyses are consistent with the age of the xenolith being ≥ ca. 1.71 Ga and thus with the assignment of the xenoliths protolith to the ca. 1.84-1.71 Ga Wernecke Supergroup. Furthermore, imprecise analyses of 6 detrital cores from xenoliths 9047 and 9048 are consistent with this interpretation. Moreover, the neodymium isotopic systematics of xenoliths 9044 and 9048 are indistinguishable from those of the Wernecke Mountain Supergroup (Thorkelson et al., 2005) and fall within the range characteristic of the western Canadian Shield, and the terranes amalgamated during the ca. 1.95-1.84 Ga Wopmay Orogen (Bowring and Podosek, 1989; Villeneuve et al., 1991, 1993; Ross et al., 2001).

Proterozoic Metamorphism as Revealed by SHRIMP Zircon U-Pb Geochronology

U-Pb isotopic systematics of metamorphic rims and recrystallized zircon domains from five xenoliths indicate that parts of the crust beneath the study area were subjected to at least three metamorphic events during the Proterozoic, at ca. 1.60 Ga, 1.27 Ga and.1.15 Ga.

Wernecke Breccia-age 1.6 Ga Metamorphism Revealed by Zircon Cores from Xenolith 9046

An important result of the ion probe analyses of zircon grains from xenolith 9046 was the identification of ca. 1.60-1.45 Ga "concordant" to slightly discordant cores. Zircon of this age is unrepresentative of Laurentian sources, falling within

a 120 m.y. period of magmatic quiescence in North America (1610 -1490 Ma) However, it is considered a valuable tool in paleocontinental reconstructions, since it is widespread in Australia (Blewett et al., 1998; Page and Sun, 1998; Ireland et al., 1999; Camacho et al., 2002; Raetz et al., 2002), Amazonia (Bettencourt et al., 1999; Bell et al., 1999), Baltica (Ahäll et al., 2000; Rämö et al., 1996) and the South China block (Li et al., 2008). The abundance of ca. 1.61-1.50 Ga detrital zircon grains in the ca. 1.47-1.40 Ga Belt-Purcell Basin of western North America has been used to argue for a direct connection between western Laurentia and Australian crust at ca. 1.45 Ga (Ross et al., 1992; Ross and Villeneuve, 2003). As discussed above (Petrology and Geochronology of the Crustal Xenoliths section), the distribution of zircon core ages does not allow for a unique interpretation and can be interpreted in three ways, with widely different implications.

Our preferred interpretation of the U-Pb data is that the concordance of zircon cores from xenolith 9046 is only apparent and that the observed age distribution is spurious, lying along a short discordia line having a lower intercept at ca. 1150 Ma and a poorly defined upper intercept at ca. 1.6 Ga. This interpretation is based on the similar Th/U ratios and U concentrations of the cores (Fig. A10), which suggest that they may be genetically related. The observed range of ages is thus believed to reflect variable disturbance of the U-Pb isotopic systematics of these cogenetic grains. In this scenario, a tectono-thermal event with the minimum age of 1582±28 Ma, constrained by the $^{207}Pb/^{206}Pb$ age from analysis 9046-5.1, led to growth of low Th/U, diffuse,

irregularly zoned zircon and/or recrystallization of existing detrital zircon in a protolith older than ca. 1.6 Ga. The recrystallization was accompanied by complete loss of radiogenic Pb, thus obliterating any of the protolith's pre-1.6 Ga history. The subsequent episode of metamorphism at ca. 1150 Ma manifested itself through renewed zircon recrystallization and growth of very weakly luminescent, U-rich (>2000 ppm) zircon, having near constant Th/U of ~0.1.

An alternative interpretation is that the U-Pb isotopic ratios of the analyzed zircon cores reflect the original U-Pb systematics, and the maximum $^{206}Pb/^{238}U$ age of the xenolith protolith is 1142±19 Ma, defined by the youngest analyzed core. If correct, then all of the analyzed cores could represent detrital grains, such that the protolith of xenolith 9046 was sourced from an area dominated by ca. 1.60-1.45 Ga zircon, but characterized by a relative absence of grains older than 1.60 Ga. Such a source, however, seems unlikely as most tectonic provinces characterized by an abundance of ca. 1.60-1.45 Ga zircon also contain significant populations of Paleoproterozoic and Archean zircon grains (Fig. A12). If this hypothesis were correct, then the sedimentary protolith of xenolith 9046 would have been deposited shortly prior to, or during the ca. 1150 Ma metamorphism, an idea that is difficult to reconcile with the inferred ca. 1.38-1.0 Ga depositional hiatus in the study area.

Another possible interpretation is that the xenolith 9046 was derived from a ca. 1150 Ma shallow, peraluminous intrusion or a volcanic flow. In this hypothesis, the analyzed zircon cores would represent a xenocrystic population, inherited from assimilated country-rock. This scenario is equally difficult to

reconcile because assimilation of the local country-rock would be expected to yield a xenocrystic population dominated by Paleoproterozoic and Archean ages.

The ca. 1.58 Ga metamorphism, deduced from xenolith 9046, is inferred to be intimately related to a widespread and voluminous hydrothermal event, dated by U-Pb titanite at 1595±5 Ma (Thorkelson et al., 2001a) that affected many parts of the study area and resulted in the formation of numerous zones of crosscutting breccia, collectively termed Wernecke Breccia (Bell, 1986; Thorkelson, 2000). The source of heat required to drive the large-scale fluid circulation and to generate the high fluid temperatures (Hunt, 2004) is not known, but a deep-seated intrusive complex, conceivably acting as a magma source to the Slab volcanics is appealing (Thorkelson et al., 2005). Whether the postulated ca. 1.6 Ga zircon grains from xenolith 9046 reflect thermal metamorphism of the intruded country-rock or precipitation of zircon from hot hydrothermal fluids, driven by deep intrusion cannot be determined due to the poor understanding of the xenolith's petrographic character.

Our proposed model for the observed distribution of nearly concordant zircon cores in xenolith 9046 removes the necessity for a westerly source of ca. 1.60-1.45 Ga zircon grains; although a proximal relationship with South Australia at ca. 1.60 Ga is still a viable hypothesis based on the similar mineral assemblages and textures between the Wernecke Breccia and the breccias near the Olympic Dam deposit (Thorkelson et al., 2001b). Furthermore, this model identifies a potential northwesterrn Laurentian source for the ca. 1.58 Ga zircon.

Mackenzie-age Metamorphism (1.27 Ga)

Analyses of zircon rims from xenolith 9044, and diffuse recrystallized zircon domains of xenolith 9047 provide evidence for metamorphism at ca. 1.27 Ga. U-Pb data from xenolith 9047 yield a concordant age of 1269±20 Ma. Analyses from xenolith 9044 lie along a well-defined discordia line, anchored by upper and lower intercepts of 1242±29 Ma and 503±79 Ma, respectively. We interpret the upper intercept as the age of the thermal disturbance that led to zircon growth and recrystallization of detrital zircon cores, and the lower intercept as the time of fluid-facilitated Pb loss during the xenolith's entrainment in the lamprophyre melt.

Metamorphism and zircon growth at 1.27 Ga is consistent with existing evidence for igneous and hydrothermal activity in northern Yukon. In the Wernecke Mountains, the Bear River dykes were intruded into the Wernecke Supergroup at ca. 1.27 Ga, based on U-Pb zircon and baddeleyite ages. By comparison of age and composition, Schwab et al. (2004) correlated the Bear River dykes with the Mackenzie radiating dyke swarm, which was emplaced across much of the Canadian Shield at 1267±2 Ma (U-Pb baddeleyite; Le Cheminant and Heaman, 1989) above a large mantle plume centred beneath Victoria Island (Ernst et al., 1995). In the Richardson Mountains, approximately 150 km north-northwest of the study area, evidence of secondary hydrothermal activity in a zone of Wernecke Breccia (Nor mineral occurrence; probably generated at ca. 1.60 Ga), was provided by a U-Pb monazite date of 1.27±0.04 Ga from a hydrothermal vein (Parrish and Bell, 1987; Thorkelson et al., 2001b).

Davis (1997) suggested that Mackenzie-aged zircon and rutile dates from mafic granulite xenoliths in the Slave province represented metamorphism induced by advective transport of heat through lateral intrusion of mafic magma generated hundreds of kilometres away. Similarly, we attribute the growth and recrystallization of specific zircon domains from xenoliths 9044 and 9047 to the heat supplied by the intrusion of mafic magma of the Mackenzie event into the crust of Yukon.

Grenville-age Metamorphism (1.15 Ga)

The new zircon U-Pb data from crustal xenoliths obtained from lamprophyre sample 2 provide compelling evidence for an episode of Grenville-age metamorphism and limited igneous activity at ca. 1150 Ma. Interpreted recrystallization, metamorphic growth and igneous crystallization ages of 1168±22, 1149±21, 1149±19 and 1146±31 Ma from xenoliths 9046, 9047, 9048 and 9049, respectively, strongly suggest a Grenvillian tectono-thermal disturbance in the Wernecke Mountains. The exact nature and the tectonic mechanism responsible for this disturbance are still poorly understood, as the event is weakly manifested at the surface, and geological relationships argue against significant compressional deformation during this time interval (Thorkelson et al., 2005). Local karst features in the Pinguicula Group (>1.38 Ga), imply subaerial chemical weathering and uplift prior to onset of deposition of the Mackenzie Mountains Supergroup in the Wernecke Mountains at ca. 1.00 Ga (Thorkelson, 2000). Evidence of deformation is limited to the presence of an angular unconformity between the two groups in the Ogilvie Mountains (Abbott,

1997), and is thus poorly constrained to a large time interval of >300 m.y. The new SHRIMP data compliments a U-Pb titanite date of 1113±5 Ma from a late stage vein within the Wernecke Breccia body at the Slab mineral occurrence (Hunt, 2004; Fig. 1). In addition, two Ar-Ar white mica cooling ages from vein and breccia bodies hosted by the Wernecke Supergroup (1178.0±6.1, 1135.0±5.5; Hunt, 2004) that are considerably older than the ca. 1.0-0.75 Ga Corn Creek orogeny (Fig. 8) support a Grenville-age thermal disturbance in the study area.

No evidence for Grenville-age magmatism in the Wernecke Mountains has been found to date. Direct evidence for Grenville-age igneous activity, however, exists in the southern Mackenzie Mountains of Northwest Territories, where granitic xenoliths from the Coates Lake diatreme yielded crystallization ages of ca. 1175-1100 Ma (Jefferson and Parrish, 1988) and ca. 1128.7 +3.9/-3.5 Ma (Mortensen and Colpron, 1998). A coeval, ca. 1.1 Ga lithospheric mantle melting event, spanning the length of the Canadian Cordillera and based on an Osmium isotopic study of spinel lherzolite xenoliths collected from mid-Tertiary alkali basaltic lavas has been suggested by Peslier et al. (2000). This inferred mantle melting episode is coeval with the suggested LREE enrichment of the Quartet Mountain Lamprophyre source mantle at ca. 1.2-1.1 Ga, based on the calculated Nd model ages from the lamprophyres. It remains unclear, however, whether the sub-Cordilleran mantle was added directly to the North American lithosphere as it experienced melt extraction, or whether it was formed as oceanic lithosphere that was later accreted to the North American craton (Peslier et al., 2000).

Scattered geochronological evidence for Grenville-age tectonism spans the length of the northern Cordillera, extending as far south as central Idaho (Fig. 7; Table 7). A number of preliminary results from studies conducted in central and northern Idaho (Gillerman et al., 2002; Jercinovic et al., 2002; Sha et al., 2004; Lund et al., 2004; Doughty, 2005; Vervoort et al., 2005) offer evidence of a late Mesoproterozoic tectono-thermal event in the northwestern U.S. Cordillera. Lu-Hf geochronology of garnet-bearing amphibolites and pelitic schists hint at a ca. 1.2-1.0 Ga contractional event (Sha et al., 2004; Vervoort et al., 2005). Ca. 1.2-1.0 Ga U-Pb and Re-Os dates from hydrothermal deposits in the Lemhi Pass, Idaho (Gillerman et al., 2002; Jercinovic et al., 2002) along with detrital zircon geochronology from a quartzite in central Idaho provide further evidence supporting a Grenville-age orogenic event in central Idaho (Lund et al., 2004). U-Pb dating of metamorphic zircon rims from the Priest River complex established a ca. 1.1-1.0 Ga metamorphic event in northern Idaho (Doughty, 2005). This event was, however argued by Doughty (2005) to be primarily the result of a thermal pulse because of the absence of Grenville-age deformation in the overlying ca. 1.47-1.40 Belt-Purcell Supergroup.

In the Purcell Basin of southeastern British Columbia, U-Pb dating of titanite and secondary zircon from the Mesoproterozoic Moyie Sills identified a metamorphic episode at ca. 1120-1030 Ma (Anderson and Davis, 1995). Moreover, K-Ar and Rb-Sr systematics of most of the Belt-Purcell rocks have been reset by a Grenville-age disturbance, yielding prevalently 1.1-1.0 Ga ages (Anderson and Davis, 1995). As in the Wernecke Mountains and northern Idaho,

the evidence for major deformation in the Belt-Purcell Basin is lacking, hence the Grenville-age metamorphism in the basin was interpreted to signify burial metamorphism, rather than orogeny (Anderson and Davis, 1995).

The Buffalo Hump Formation, which overlies the Belt-Purcell Supergroup, (Anderson and Parrish, 2000) contains ca. 1224-1070 Ma detrital igneous zircon thought to have been sourced from a proximal region to the west (Ross et al., 1992). Paleozoic diatremes in the southern Canadian Rocky Mountains (Pell, 1987, 1994; Helmstaedt et al., 1988; Smith et al., 1988) contain a small population of ca. 1.1-1.0 Ga xenocrystic zircon, which is consistent with the presence of Grenville-age crystalline rocks in the Cordilleran basement, although it is permissible that the xenocrysts originated as detrital grains in Neoproterozoic or lower Paleozoic clastic strata (Parrish and Reichenbach, 1991). Similarly, distinct ca. 1030 Ma and ca. 1053 Ma age peaks from the Ordovician Mount Wilson Formation miogeoclinal sandstone were attributed to two distinct, Grenville-age, igneous episodes that generated unrecognized plutons along the Cordilleran Margin (Gehrels and Ross, 1998). Furthermore, a granitic clast collected from the Neoproterozoic Horsethief Creek Group in the southeastern Cariboo Mountains, British Columbia, yielded a crystallization age of 1189±33 Ma (Ross et al., 1992), implying a proximal Grenville-age source in the southern Canadian Cordillera.

Also notable are the oldest detrital zircon grains and the age of a felsic metaporphyry clast from the metaconglomerate unit of the Bob Lake assemblage of the Nicola Horst, which yielded U-Pb ages of ca. 1030 Ma and ca. 1038 Ma,

respectively (Erdmer et al., 2002). Additionally, a sample of quartz-feldspar-biotite schist, also from the Bob Lake assemblage, produced two concordant Grenville-age analyses. The significance of these ages is uncertain however, as both the timing and the palaeographic location of the Bob Lake assemblage are poorly understood. The paleogeographic setting of the ca. 1.0-0.9 Ga metarhyolite, which in part forms the Proterozoic basement of Alaska's Farewell terrane is also poorly constrained (Bradley et al., 2003).

Importantly, Grenville-age deformation of the northwestern Laurentia is evident in the Coppermine homocline, where the rocks of the ca. 1.267 Ga Coppermine River Group were faulted and affected by two orthogonal generations of folding prior to the deposition of the ca. 1.00 - 0.723 Ga Shaler Supergroup (Hildebrand and Baragar, 1991). The observed structural relationships imply that a north-south directed compressional event was supplanted by an east-west directed event, and that the Coppermine homocline underwent two deformational events between ca. 1.267 Ga and 1.0 Ga.

The newly-identified period of ca. 1150 Ma metamorphism in the Wernecke Mountains expands the list of Grenville-age tectono-thermal disturbances that affected the Laurentian northwestern paleomargin along its length and provides additional constraints for reconstructions of the Late Mesoproterozoic supercontinent Rodinia.

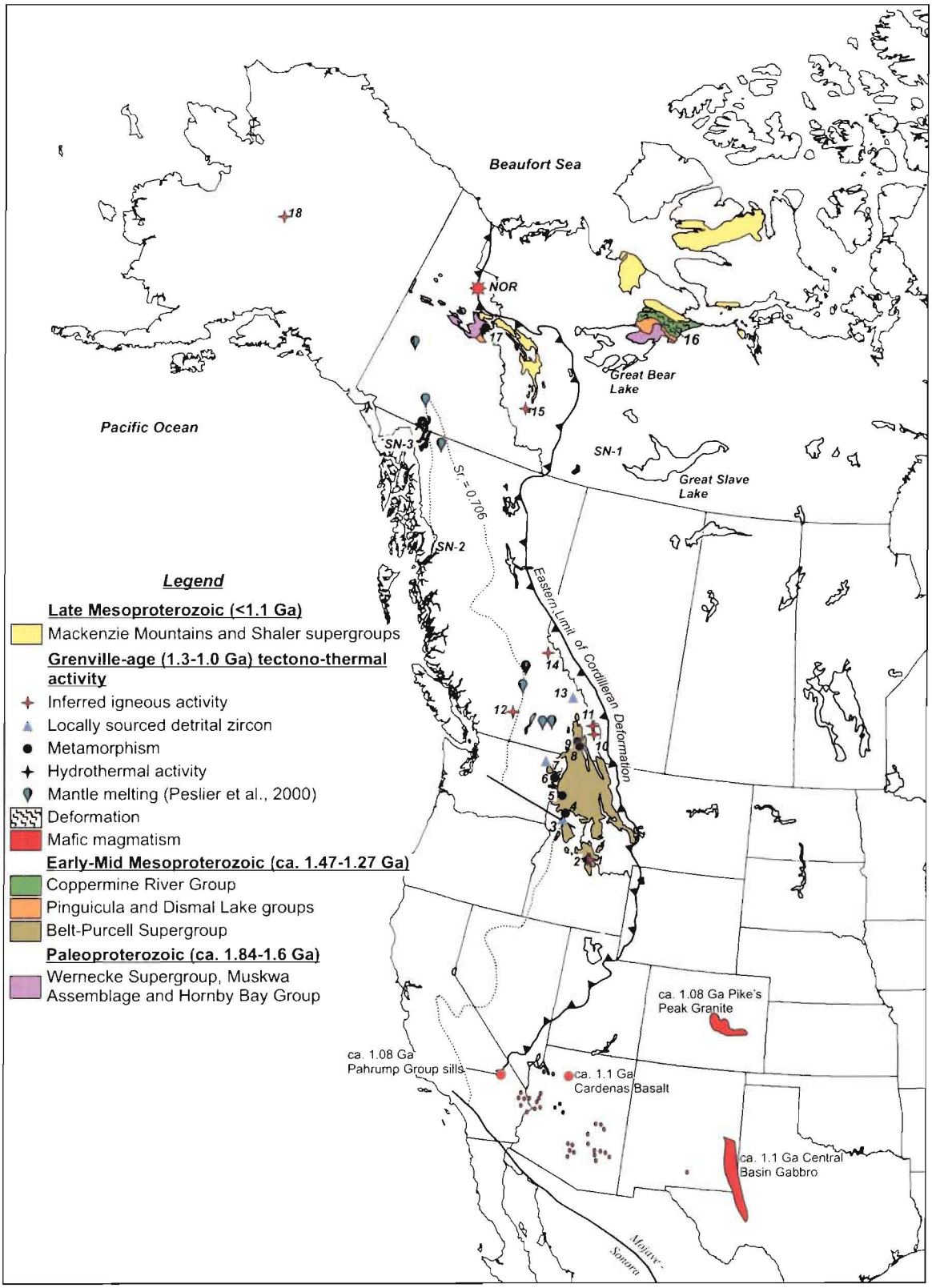

Figure 7. Grenville-aged tectono-thermal activity in western North America. See Table 7 for more details.

Tectonic Model for the Grenville-age Metamorphism of Northwestern Laurentia

The geographical extent of the geochronological evidence summarized above argues for a regional tectono-thermal event or a series of events that affected the northwestern margin of Laurentia at ca. 1.2-1.0 Ga. An important observation regarding this event is the absence of deformation in regions north of central Idaho that are known to have experienced metamorphism during this time (Anderson and Davis, 1995; Thorkelson, 2000; Doughty, 2005), in contrast to the presence of deformational structures attributed to the Grenville-age event in central Idaho (Sha et al., 2004; Vervoort et al., 2005). Specifically, regional geology of Proterozoic inliers in northern Canada argues against significant Grenville-age compressional deformation (Thorkelson, 2000). Similarly, Anderson and Davis (1995) invoke burial metamorphism to explain the lack of deformation that accompanied the upper greenschist – lower amphibolite facies metamorphism of the Moyie sills at ca. 1.1 Ga. In contrast, Sha et al. (2004) and Vervoort et al. (2005) attributed the deformational structures from the Clearwater Complex-Boehls Butte Core Complex (Fig. 7) to a contractional event that led to crustal thickening. Furthermore, Lund et al. (2004) contended that mineralization ages (Gillerman et al., 2002; Jercinovic et al., 2002) along with locally derived ca. 1.2-1.0 Ga detrital zircon provide evidence for a ca. 1.2-1.0 Ga orogenic event in central Idaho.

A number of models place western Laurentia adjacent to other cratonic landmasses during Grenvillian time. Models that identify Australia as a conjugate to western Laurentia are based on: similarity of glacio-eustatic Neoproterozoic sedimentary cycles (Eisbacher, 1985); Meso- to Neoproterozoic stratigraphy and metallogeny (Bell and Jefferson, 1987); continuity of Proterozoic orogenic belts that occur in western Laurentia and East Gondwanaland (Australia and Antarctica; Moores, 1991; Dalziel, 1991; Hoffman, 1991); unusual ca. 1610-1500 Ma detrital zircon geochronology of Belt-Purcell Supergroup (Ross and Villeneuve, 2003) that is typical of basement-blocks of south-central Australia (Ross et al., 1992); and the identification of Grenville-age detrital zircon in both Buffalo Hump Formation and North Queensland (Blewett et al., 1998). Much of the evidence used to argue for Late Mesoproterozoic-Neoproterozoic link between northwestern Laurentia and Australia relies on Paleoproterozoic and Early Mesoproterozoic correlations and hence implies long-term stability (>500 m.y.) of the combined landmass prior to the development of Rodinia. Geological evidence supporting the Grenville-age link between the two continents is limited to the presence of Grenvillian detrital zircon grains along the proposed conjugate margins (Blewett et al., 1998) and similar Neoproterozoic stratigraphy that is also present in South China (Eisbacher, 1985). Although paleomagnetic data demonstrate that joint motion of Laurentia and Australia is permissible in the ca. 1050-725 Ma interval, such a connection is not permissible during the ca. 1.5-1.2 Ga interval (Pisarevsky et al., 2003; Li et al., 2008). This paleomagnetic constraint, however, does not negate a link between Australia and northwestern

Laurentia during the Paleoproterozoic (Idnurm and Giddings, 1995; Thorkelson et al., 2001a; Betts and Giles, 2006). An important weakness of the models that propose a direct Australia-northwestern Laurentia linkage that was terminated by Neoproterozoic rifting is the poor agreement of Neoproterozoic plume records of the two continents (Li et al., 2008).

Although most Rodinian paleoreconstructions place Siberia along Laurentia's northern margin (Hoffman, 1991; Condie and Rosen, 1994; Frost et al., 1998; Rainbird et al., 1998; Pisarevsky and Natapov, 2003), the model of Sears and Price (1978, 2000, 2003) and Sears et al. (2004) invokes a Proterozoic connection between Siberia and western Laurentia based on permissible alignment of Paleoproterozoic orogenic belts and shear zones, Mesoproterozoic dike/sill swarms and Mesoproterozoic Belt-Purcell and Udzha basins. This configuration, however, is not supported by paleomagnetic evidence (Li et al., 2008) and is further weakened by the absence of potential sources of ca. 1.6-1.5 Ga zircon in Siberia, thus requiring at least one additional continental mass that would serve as a source of this age of zircon for both Belt-Purcell and Udzha basins. In addition, much like the AUSWUS model, which positions Australia west of the southwestern U.S.A. (Brookfield, 1993; Karlstrom et al., 1999), this configuration places the adjacent craton far to the south, leaving northwestern Laurentia without a conjugate landmass.

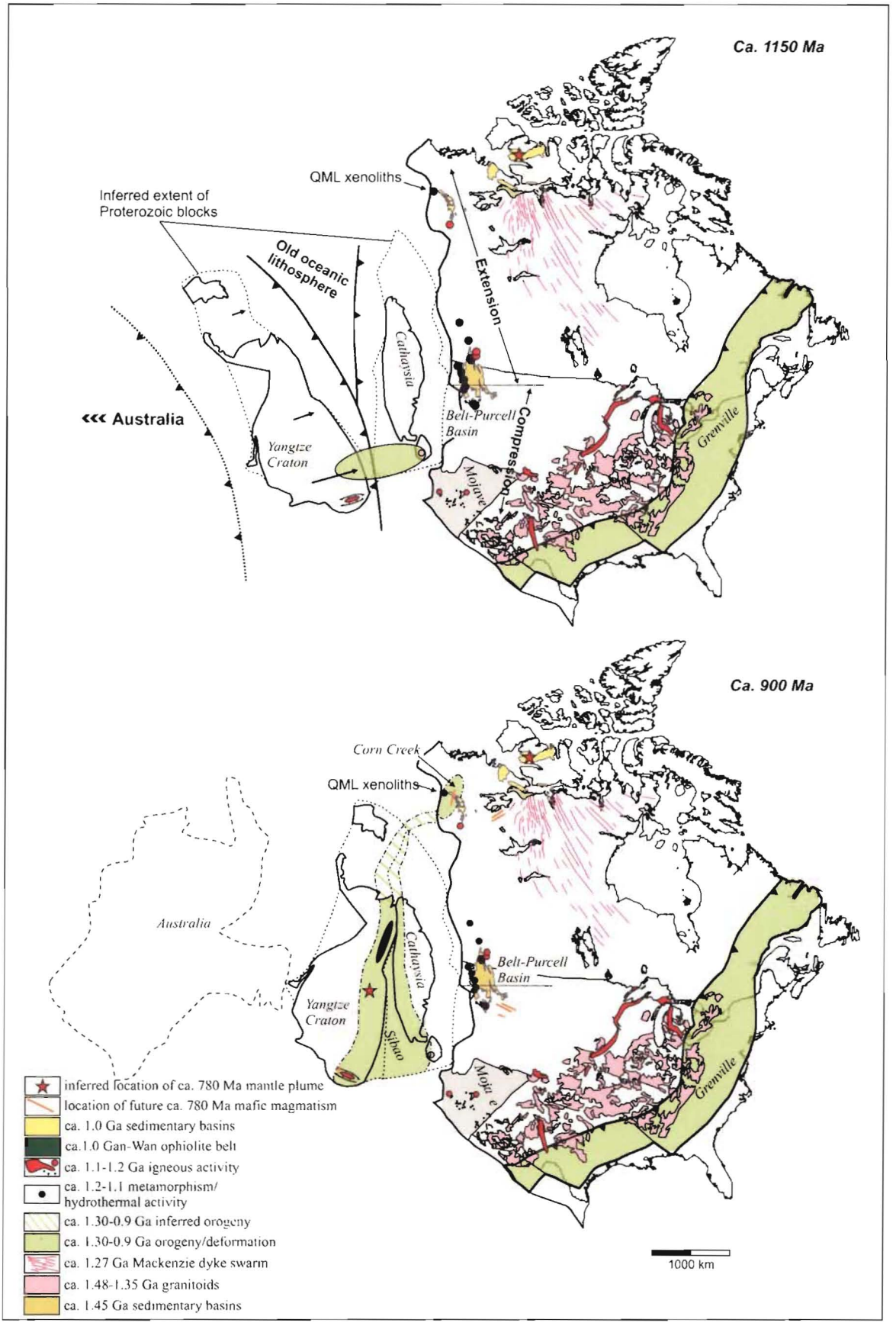
Ca. 1150 Ma
QML xenoliths
Inferred extent of
Proterozoic blocks
Old oceanic
lithosphere
Extension
Compression
Cathaysia
Belt-Purcell
Basin
Grenville
Mojave
Yangtze
Craton
<<< Australia
Ca. 900 Ma
Corn Creek
QML xenoliths
Australia
Cathaysia
Belt-Purcell
Basin
Yangtze
Craton
Sibao
Grenville
inferred location of ca. 780 Ma mantle plume
location of future ca. 780 Ma mafic magmatism
ca. 1.0 Ga sedimentary basins
ca.1.0 Gan-Wan ophiolite belt
ca. 1.1-1.2 Ga igneous activity
ca. 1.2-1.1 metamorphism/
hydrothermal activity
ca. 1.30-0.9 Ga inferred orogeny
ca. 1.30-0.9 Ga orogeny/deformation
ca. 1.27 Ga Mackenzie dyke swarm
ca. 1.48-1.35 Ga granitoids
ca. 1.45 Ga sedimentary basins
1000 km

Figure 8. Tectonic model for the cryptic Grenville-aged metamorphism along the western margin of ancestral North America. The model is an adaptation of the "missing-link" model of Li et al. (2007), and treats the Cathaysia block as a piece of Laurentian crust, detached during the break-up of Rodinia at ca. 780 Ma. a) In this model, the asymetric convergence rate of the Yangtze Craton towards the Cathysia block at ca. 1.15 Ga, accounts for the deformation accompanying metamorphism and igneous activity in SW USA, and the absence of deformation accompanying metamorphism in NW Canada and the Belt-Purcell Basin. The Yangtze-Cathysia collision and the related formation of the Sibao Orogen is believed to have begun in the south before ca. 1140 Ma (Greentree et al., 2006), and to have ended at ca. 900 Ma in the north (relative to figure orientation). b)The late collision in the north is coincident with the Corn Creek orogeny (Thorkelson et al., 2005) and may mark the transition from extensional, back-arc tectonics to a compressional regime and related thin-skinned orogenesis. The ca. 780 Ma mafic magmatism in Laurentia (Harlan et al., 2003) and Yangtze Craton (Li et al. 2003b) interpreted to be mantle plume generated, serves as a piercing point for the model in the Neoproterozoic.

The "missing-link" hypothesis of Li et al. (1995; 2002; 2008) is an attractive alternative to explain the belt of scattered 1.2-1.0 Ga metamorphic and igneous crystallization ages along the western margin of ancestral North America (Fig. 7). In this hypothesis, the ca. 1830-1430 Ma Cathaysia Block of the South China Block was the western extension of the Laurentian craton during the Mesoproterozoic and served as a proximal western source for some of the sediment in the Belt-Purcell Supergroup and the overlying Buffalo Hump Formation (Li et al., 2002, 2008). The ca. 1430 Ma granitic intrusions on Hainan Island are similar to the ca. 1.48-1.35 Ga granitoids that form a transcontinental magmatic belt across southern Laurentia (e.g., Whitmeyer and Karlstrom, 2007), and were used by Li et al. (2002) to position Cathaysia adjacent to the Mojave Province of southwestern Laurentia (Fig. 8). According to the model, Cathaysia became attached to Laurentia after the Wopmay Orogeny (ca. 2.10-1.84 Ga), but prior to deposition of the ca. 1.47-1.40 Ga Belt-Purcell Supergroup (Ross and Villeneuve, 2003). The other half of the South China Block, the Yangtze Craton, began obliquely colliding with the unified Laurentia-Cathaysia mass at ca. 1140 Ma at the western end (present-day coordinates) of the Sibao Orogen (Greentree et al., 2006). The collision, accompanied by ophiolite obduction (Li et al., 1994; 2003), progressed to the east and continued until ~900 Ma. The separation of Cathaysia from Laurentia is envisioned to have happened during Neoproterozoic rifting and the break-up of Rodinia.

We propose a model which utilizes the oblique collision of the Yangtze Craton with Cathaysia to explain the range of Grenville-age igneous,

metamorphic and deformational features that are present along northwestern Laurentia. The oblique convergence generated two distinct stress fields in Laurentia at ca. 1150 Ma: a dominantly extensional field between the Purcell Basin and the present-day Arctic Ocean, and a dominantly compressional field south of the Belt-Purcell Basin (Fig. 8). In the model, the northwestern Laurentian margin, north of central Idaho, occupied a region of extending continental crust overriding the slowly advancing northern (present day North American coordinates) portion of the oceanic basin separating it from the Yangtze Craton. In this scenario, the extension is driven by the rollback of the subducting slab, which is more rapid than the advancement of the overriding Laurentian plate (cf. Molnar and Atwater, 1978). This far-field continental back arc may have extended from the Mackenzie Delta in the north to the Belt-Purcell basin in the south (Fig. 8). Elevated geotherms, associated with the thinning of continental lithosphere, would thus account for the observed metamorphism and magmatism stemming from small-volume crustal melting. Supporting evidence for the upwelling and decompressive melting of the upper mantle that accompanied the proposed lithospheric thinning in the back-arc environment is provided the Re-Os study of Peslier et al. (2000) and the suggested LREE enrichment of the Quartet Mountain Lamprophyre mantle source (this study). The extension may have been followed by a phase of thermal subsidence accompanied by sedimentation and the deposition of the Mackenzie Mountains Supergroup. A similar model has been proposed by Giles et al. (2002) and Betts and Giles (2006) to account for the development of ca. 1.80-1.67 Ga basins in northeastern Australia.

Furthermore, the subsiding Mackenzie Mountain Supergroup basin is envisioned to have been sourced from a topographically elevated region to the east as originally proposed by Rainbird et al. (1992, 1997). We also speculate that the continent-continent collision, which followed the consumption of the ocean basin intervening between the Yangtze Craton and Cathaysia Block at ca. 900 Ma, may have generated the Corn Creek orogeny and terminated deposition of Mackenzie Mountains Supergroup.

Our proposed model does not account for the pre-1.0 Ga contractional deformation that affected the ca. 1.267 Ga Coppermine River Group in the Coppermine homocline (Irvine and Baragar, 1991; Fig. 7). We think it is likely that the extensional stress field produced by the oblique convergence of Yangtze Craton with western Laurentia did not extend east of present-day Great Bear Lake (Figs. 7 and 8), and that the stress-field in the area of the Coppermine homocline was dominated by tectonic processes to the east, related to the Grenville Orogeny, or presently unidentified processes to the north.

In contrast to the proposed Grenville-age extensional tectonic regime that dominated northwestern Laurentia, preliminary studies by Sha et al. (2004), Lund et al. (2004) and Vervoort et al. (2005) suggested that ca. 1.2-1.0 Ga metamorphism in north-central Idaho was synchronous with orogenesis and development of polyphase deformational structures. Further south in Arizona and California, Howard (1991) concluded that ca. 1.1 Ga diabase sheets were emplaced into the crust that was under tectonic compression or in an isotropic state of stress. The oblique convergence between the Yangtze Craton and the

Laurentia-Cathysia mass and the initial collision at ca. 1140 Ma (Greentree et al., 2006) at the latitude of present day southwestern U.S. may have produced a compressive stress field through much of the western U.S.

Conclusions

The Quartet Mountain Lamprophyres are a suite of Early Cambrian phlogopite-rich ultramafic dykes that were emplaced into Proterozoic metasedimentary strata at ca. 532-522 Ma. Trace element systematics indicate magma genesis by small degrees of partial melting of a LREE-enriched, garnetiferous upper mantle. Some of the lamprophyres contain crustal +/- mantle xenoliths. Many of the crustal xenoliths display metamorphic grades no higher than lower greenschist and appear to be fragments of wallrock from the Wernecke Supergroup or Mackenzie Mountains Supergroup which host the intrusions. These xenoliths were not investigated; however, five xenoliths with higher metamorphic grades were studied using standard petrography, scanning electron microscopy, Nd isotope geochemistry, and SHRIMP U-Pb geochronology. Three of these xenoliths contain sillimanite, one contains relict orthopyroxene, and one displays a retrograde assemblage dominated by sericite. The source rocks for these xenoliths is unknown, but two plausible options are (1) the cratonic infrastructure (likely pre-1.84 Ga), and (2) deeply buried parts of the suprastructure, including the Wernecke Supergroup or lower successions. The data from these five xenoliths provide important new information on metamorphism of the Yukon crust, with implications for the Proterozoic evolution of western Laurentia.

Two xenoliths display metamorphic zircon growth and recrystallization at ca. 1.27 Ga, implying metamorphism related to emplacement of the coeval Bear River dykes (Schwab et al., 2004) which are the western continuation of the Mackenzie dyke swarm (Le Cheminant and Heaman, 1989). Concomitant veining in the Richardson Mountains of northern Yukon (Parrish and Bell, 1987) appears to be a shallow manifestation of igneous intrusions at depth (Schwab et al., 2004).

One xenolith contains abundant, nearly-concordant ca. 1.45-1.60 Ga zircon cores that fall within a North American magmatic gap in igneous ages (Ross and Villeneuve, 2003) as well as a continuum of near-concordant ages from cores, ranging from ca. 1.3 to 1.15 Ga. The data are interpreted to represent (1) igneous crystallization of zircon at times >1.6 Ga; (2) complete metamorphic or metasomatic recrystallization at ca. 1.6 Ga, and (3) renewed metamorphism and partial resetting of U-Pb systematics at ca. 1.15 Ga. The 1.6 Ga event is likely tied to widespread hydrothermal activity that produced the Wernecke breccias and related iron-oxide copper gold occurrences (Thorkelson et al., 2001a). The 1.15 Ga event belongs to a set of Grenville-age disturbances that extend from Yukon to central Idaho.

Grenville-age metamorphism is also evident in two sillimanite-bearing xenoliths. U-Pb SHRIMP analyses of metamorphic zircon rims and recrystallized domains yield near identical metamorphic ages of ca. 1.15 Ga. Furthermore, one orthopyroxene-bearing xenolith, derived from an inferred meta-igneous protolith is characterized by near coeval igneous crystallization and late stage

recrystallization at ca. 1.15 Ga. Altogether, four xenoliths provide unequivocal evidence for a thermal pulse in the crust of northern Yukon at ca. 1.15 Ga.

Hints of ca. 1.2-1.0 Ga tectono-thermal activity exist along much of the pre-Cordilleran margin of western North America. Evidence that the metamorphism in northwestern Laurentia was accompanied by compressional deformation and orogenesis is lacking. In contrast, Grenville-age metamorphism and magmatism in the western United States south of the Belt-Purcell Basin has been interpreted as compressional (Howard, 1991; Sha et al. 2004; Lund et al., 2004; Vervoort et al., 2005). To reconcile this difference, we invoke the "missing link" model of Li et al. (1995, 2002, 2008), which involves oblique collision between the Yangtze Craton and a unified Laurentia-Cathysia block between ca. 1140 Ma and ca. 900 Ma. We suggest that the oblique convergence generated two distinct stress fields in Laurentia at ca. 1150 Ma: a dominantly compressional field south of the Belt-Purcell Basin and a dominantly extensional field between the Purcell Basin and the present-day Arctic Ocean. The extension in northwestern Laurentia was accompanied by lithospheric thinning and crustal heating that is recorded by the xenoliths. The final stages of the encroachment of the Yangtze craton at ca. 900 Ma onto the Laurentia-Cathysia landmass may be recorded by the compressional deformation of the Corn Creek orogeny (1.00-0.78 Ga) and inversion of the Mackenzie Mountains Supergroup sedimentary basin.

Tables

Table 1. Quartet Mountain Lamprophyres - locations and field measurements

Sample	Lamprophyre field number	Location Easting	Northing	1:50 000 NTS map sheet	Orientation	Width (m)
1	DM-05-1-1-2	514617	7226946	106E/2	015/80	1.5
2[a,b,c]	DT-02-12-1-4	546987	7219808	106F/4	240/85	0.15
3[b]	DM-05-3-2-3	546610	7219902	106E/1	232/60	0.80
4	DM-05-4-1-1	528748	7222915	106E/1	float	
5	DM-05-4-2-1	528950	7223483	106E/1	toppled	0.85
6[a,b,c]	DT-02-7-1-1	529033	7223487	106E/1	290/80	2
7[a]	DT-02-7-3-1	529033	7223487	106E/1	080/70	1.75
8	RBI-05-1-1-1	528607	7223554	106E/1	talus	
9	DM-05-5-1-1	528037	7223962	106E/1	talus	
10	DM-05-6-2-1	528632	7223374	106E/1	090/89	0.80
11	DM-05-6-3-1	528478	7223438	106E/1	float	
12	DM-05-6-4-1	528273	7223543	106E/1	float	
13	DM-05-7-1-1	516530	7227670	106E/2	260/89	1.2
14	DM-05-7-2-1	516037	7228640	106E/2	-	
15	DM-05-7-4-1	515768	7229922	106E/2	steep at 255	1.5
16[a,b,c]	TOA-96-8-1	516399	7230074	106E/2	float	
17	DT-02-9-4-1	524225	7231523	106E/1	140/80	1.2
18[a,b]	DT-93-151-1	553466	7197871	106C/13	270/90	
19	-	-	-	106C/13	-	

Notes:

[a] sample analyzed for geochemistry; [b] sample analyzed for ^{40}Ar-^{39}Ar geochronology; [c] sample analyzed for Nd isotopes

Table 2. Major element oxide (wt. %) and trace element (ppm) concentrations from the Quartet Mountain Lamprophyres.

Sample No.	2		6		7		16[†]	18[‡]
UTM	0547011 7219889		0529033 7223487		0529033 7223487		0533466 7197871	0516399 7230074
Major Elements								
SiO_2	23.78	*0.32*	39.63	*0.53*	40.19	*0.53*	37.40	31.03
TiO_2	1.42	*0.02*	3.26	*0.04*	3.29	*0.04*	3.50	3.76
Al_2O_3	2.83	*0.10*	7.80	*0.25*	8.34	*0.27*	6.62	6.33
Fe_2O_3	7.56	*0.24*	13.00	*0.40*	13.19	*0.41*	21.66	13.47
MnO	0.12	*0.01*	0.19	*0.01*	0.26	*0.01*	0.44	0.31
MgO	19.43	*0.21*	15.38	*0.17*	14.73	*0.16*	16.00	14.18
CaO	16.29	*0.25*	11.50	*0.18*	11.39	*0.18*	9.20	14.83
Na_2O	0.06	*0.07*	1.07	*0.08*	0.87	*0.08*	0.46	0.18
K_2O	1.89	*0.04*	1.37	*0.03*	1.03	*0.03*	1.01	2.60
P_2O_5	1.01	*0.07*	0.63	*0.06*	0.69	*0.06*	0.86	1.95
LOI	24.76		4.71		4.95		7.25	10.2
Total	99.14		98.55		98.92		104.40	98.84
Trace Elements								
Ba	1204	*43*	983	*36*	543	*23*	4263	2160
Rb	86	9	44	*5*	32	*5*	38	92
Cs	3.5	*0.3*	2.7	*0.2*	3.6	*0.3*	3.1	3.3
Th	29.47	*2.66*	6.91	*0.85*	7.16	*0.87*	8.74	23.17
Ta	7.86	*0.81*	5.02	*0.55*	5.27	*0.57*	5.94	8.12
U	4.69	*0.56*	1.73	*0.27*	1.75	*0.28*	2.42	3.85
Nb	168.6	*5.7*	84.4	*4.8*	89.3	*4.9*	122.4	157.3
La	194.4	*14.8*	56.0	*5.1*	59.4	*5.4*	66.8	194.5
Ce	360.1	*18.2*	111.3	*7.0*	117.6	*7.3*	134.0	380.5
Pb	14	*8*	11	*8*	9	*8*	6	*bdl*
Sr	1544	*18*	432	*7*	388	*6*	846	951
Pr	39.06	*8.44*	12.96	*2.80*	13.75	*2.97*	16.21	37.33
Nd	138.5	*2.0*	51.9	*2.0*	54.0	*2.0*	64.2	157.3
Zr	253	*11*	261	*11*	264	*11*	318	354
Sm	20.30	*1.53*	10.85	*0.92*	11.57	*0.96*	12.12	26.29
Hf	6.5	*0.7*	6.6	*0.7*	6.6	*0.7*	7.6	8.8
Eu	4.90	*0.12*	3.10	*0.10*	3.25	*0.10*	3.58	6.44
Gd	11.84	*0.89*	8.24	*0.64*	8.56	*0.66*	11.11	18.60
Tb	1.46	*0.25*	1.18	*0.21*	1.22	*0.21*	1.23	2.25
Dy	5.59	*0.81*	5.09	*0.74*	5.32	*0.77*	6.53	9.56
Ho	0.79	*0.17*	0.78	*0.17*	0.81	*0.18*	1.03	1.40
Er	1.82	*0.35*	1.86	*0.36*	2.06	*0.39*	2.26	3.44
Tm	0.209	*0.047*	0.234	*0.052*	0.252	*0.055*	0.300	0.305
Y	20	*2.9*	21	*2.9*	22	*2.9*	25	42
Yb	1.23	*0.26*	1.37	*0.29*	1.45	*0.31*	1.44	1.87
Lu	0.131	*0.024*	0.166	*0.029*	0.174	*0.030*	0.190	0.259
V	100	*13*	248	*25*	250	*25*	322	220
Sc	20.1	*4.3*	27.5	*5.3*	24.1	*4.8*	23.8	*nd*
Cr	1220	*192*	734	*143*	736	*144*	851	364
Co	74.2	*17.6*	84.1	*19.3*	86.1	*19.6*	84.0	97.8
Cu	19	*4*	67	*6*	64	*6*	19	*bdl*
Ni	744	*52*	457	*33*	458	*33*	591	412

Abbreviations: bdl=below detection limit; nd=no data

Errors at 95% confidence level, in wt% or ppm for major element oxides and trace elements, respectively are shown in italicized letters.

[†]Thorkelson, 2000

[‡]Thorkelson, unpublished data

Table 3. Sm-Nd isotope data for Quartet Mountain Lamprophyres and their constituent crustal xenoliths.

	UTM coordinates			Sm	Nd	$^{147}Sm/^{144}Nd$	$^{143}Nd/^{144}Nd$			
Sample No.	Northing	Easting	Unit	(ppm)	(ppm)			Uncertainty[b]	T_{DM}[c]	ε_{Nd} (T)[d]
2	7219808	546987	QML	28.21	207.41	0.0822	0.512164	0.000004	1.16	-1.5 (530)
6	7223487	529033	QML	10.81	55.28	0.1183	0.512465	0.000005	1.11	1.9 (530)
16	7230074	516399	QML	27.16	172.27	0.0953	0.512213	0.000006	1.22	-1.4 (530)
9044[a]			xenolith	6.11	35.67	0.1036	0.511476	0.000005	2.32	-2.2 (1710)
9047[a]			xenolith	5.31	27.60	0.1164	0.512087	0.000007	1.68	6.9 (1710)
9048[a]			xenolith	7.69	44.17	0.1053	0.511478	0.000005	2.36	-2.6 (1710)

[a]Xenoliths 9044, 9047 and 9048 were separated from sample 2.
[b]Ucertainty in $^{143}Nd/^{144}Nd$ is expressed as 2 standard deviations (2σ).
[c]Depleted-mantle model age was calculated using the formulation of Goldstein et al., 1984.
[d]ε_{Nd} values are calculated for ages (Ma) shown in parentheses.

Table 4. ^{40}Ar-^{39}Ar results for phlogopite separates from the Quartet Mountain Lamprophyre samples 2, 3, 6 and 16

Laser Power (%)	$^{40}Ar/^{39}Ar$	$\pm$	$^{38}Ar/^{39}Ar$	$\pm$	$^{37}Ar/^{39}Ar$	$\pm$	$^{36}Ar/^{39}Ar$	$\pm$	Ca/K	Cl/K	$\%^{36}Ar$	$\%^{39}Ar^{a}$	$^{40}Ar^{*}/^{39}Ar_{K}$	$\pm$	Apparent age (Ma)	$\pm 2\sigma$
Sample 2 *phlogopite, UTM (546987, 7219808), J = 0.009570±0.000012, volume* $^{39}Ar_{K}$ *= 608.94 x* $10^{-11}cm^{3}$*, integrated age = 529.93±1.22 Ma*																
2.0	67.698	0.027	0.043	0.276	2.048	0.038	0.142	0.087	17.585	0	60.60	0.29	26.786	3.590	411.70	49.33
2.2	38.671	0.017	0.015	0.581	1.056	0.039	0.039	0.152	9.055	-0.001	28.73	0.43	27.657	1.812	423.63	24.74
2.4	52.388	0.023	0.024	0.229	0.144	0.102	0.072	0.092	1.232	-0.001	40.12	0.57	31.458	2.056	474.79	27.29
2.6	36.249	0.013	0.013	0.121	0.105	0.050	0.008	0.203	0.896	0	6.11	1.77	34.128	0.636	509.87	8.28
2.8	36.230	0.013	0.015	0.131	0.038	0.052	0.004	0.207	0.330	0	3.22	3.00	35.158	0.509	523.23	6.57
3.0	36.317	0.011	0.014	0.127	0.027	0.044	0.004	0.152	0.232	0	3.41	3.17	35.173	0.447	523.43	5.77
3.2	36.405	0.007	0.013	0.088	0.013	0.100	0.004	0.220	0.114	0	2.85	3.99	35.462	0.350	527.16	4.51
†3.4	36.334	0.006	0.013	0.132	0.015	0.061	0.002	0.322	0.125	0	1.53	5.23	35.874	0.293	532.46	3.76
†3.6	36.046	0.007	0.014	0.041	0.009	0.101	0.002	0.308	0.077	0	1.25	5.25	35.689	0.301	530.08	3.87
†3.8	36.037	0.006	0.012	0.050	0.009	0.059	0.001	0.308	0.073	0	0.98	7.63	35.778	0.259	531.23	3.34
†3.9	36.151	0.006	0.013	0.090	0.006	0.089	0.002	0.401	0.048	0	1.41	5.28	35.737	0.312	530.70	4.02
†4.0	36.311	0.009	0.013	0.053	0.005	0.177	0.001	0.293	0.044	0	1.18	5.79	35.978	0.336	533.80	4.31
†4.2	36.375	0.008	0.012	0.109	0.004	0.095	0.002	0.243	0.038	0	1.33	5.61	35.984	0.301	533.80	3.86
†4.2	36.375	0.007	0.012	0.143	0.003	0.311	0.001	0.426	0.025	-0.001	1.14	3.74	36.056	0.312	534.79	4.00
†4.3	36.073	0.008	0.014	0.051	0.006	0.153	0.001	0.423	0.048	0	0.98	4.36	35.813	0.335	531.67	4.30
†4.4	36.459	0.008	0.013	0.080	0.007	0.124	0.002	0.305	0.060	0	1.63	3.61	35.958	0.338	533.53	4.34
†4.6	36.195	0.007	0.013	0.064	0.006	0.098	0.001	0.430	0.051	0	0.69	6.93	36.040	0.286	534.59	3.67
†4.8	36.214	0.006	0.012	0.043	0.004	0.161	0.002	0.328	0.032	0	1.23	5.90	35.865	0.259	532.34	3.33
†5.0	35.897	0.008	0.012	0.107	0.004	0.157	0.001	0.436	0.037	-0.001	1.02	5.91	35.623	0.340	529.23	4.37
†5.2	36.043	0.009	0.013	0.056	0.002	0.201	0.001	0.436	0.016	0	1.07	5.63	35.750	0.358	530.87	4.61
†5.4	36.130	0.009	0.012	0.065	0.002	0.419	0.002	0.234	0.017	-0.001	1.51	5.66	35.679	0.365	529.95	4.69
5.7	36.539	0.007	0.014	0.071	0.001	0.548	0.002	0.253	0.006	0	1.26	7.59	36.172	0.286	536.29	3.67
6.0	36.370	0.010	0.013	0.125	0.002	0.833	0.004	0.392	0.021	0	3.20	2.65	35.299	0.593	525.06	7.65
Sample 3. *phlogopite, UTM (546610, 7219902), J = 0.010051±0.000010, volume* $^{39}Ar_{K}$ *= 30.89 x* $10^{-11}cm^{3}$*, integrated age = 471.26±3.06 Ma*																
2.0	21.032	0.029	0.091	0.283	0.182	0.086	0.036	0.409	0.430	0.015	17.26	1.70	13.540	4.388	230.19	70.04
2.2	24.763	0.020	0.042	0.217	0.195	0.091	0.023	0.209	0.845	0.005	11.20	3.04	19.676	1.508	325.56	22.83
2.4	33.235	0.010	0.042	0.179	0.065	0.069	0.012	0.237	0.206	0.006	4.38	6.06	30.528	0.907	482.80	12.59
2.6	33.530	0.012	0.036	0.105	0.043	0.124	0.011	0.234	0.095	0.004	4.47	7.02	30.942	0.869	488.53	12.02
2.8	34.279	0.011	0.042	0.165	0.038	0.189	0.011	0.200	0.014	0.005	3.03	5.60	31.874	0.765	501.38	10.51
3.0	33.845	0.013	0.032	0.232	0.027	0.196	0.007	0.253	0.022	0.003	1.82	8.44	32.287	0.703	507.03	9.62
3.2	36.024	0.010	0.040	0.052	0.021	0.087	0.008	0.167	0.038	0.006	3.53	12.94	34.126	0.518	532.04	6.99
3.4	28.269	0.009	0.067	0.046	0.219	0.022	0.003	0.475	1.366	0.012	0.66	17.59	27.602	0.544	441.73	7.72
3.7	27.175	0.009	0.070	0.098	0.271	0.026	0.005	0.350	1.681	0.013	1.78	16.58	26.194	0.532	421.62	7.63
4.0	32.943	0.008	0.051	0.073	0.089	0.036	0.004	0.152	0.512	0.008	1.57	20.33	32.001	0.309	503.11	4.23
4.5	44.722	0.047	0.076	0.404	0.300	0.142	0.073	0.293	0.103	0.008	8.46	0.69	31.188	6.789	491.93	93.73
Sample 6. *phlogopite, UTM (529033, 7223487), J = 0.010033±0.000010, volume* $^{39}Ar_{K}$ *= 139.04 x* $10^{-11}cm^{3}$*, integrated age = 523.57±1.35 Ma*																
2.0	38.167	0.023	0.086	0.191	0.137	0.118	0.042	0.232	0.240	0.014	17.45	0.44	28.386	3.015	452.11	42.48
†2.2	35.910	0.011	0.030	0.173	0.029	0.197	0.007	0.374	0.058	0.003	1.68	2.21	34.497	0.823	536.21	11.06
†2.4	34.094	0.008	0.026	0.070	0.010	0.209	0.003	0.343	0.015	0.003	0.93	6.09	33.437	0.376	521.89	5.10
†2.6	33.911	0.005	0.024	0.064	0.004	0.183	0.001	0.352	0.002	0.002	0.12	12.34	33.667	0.197	525.01	2.67
†2.8	33.912	0.004	0.023	0.055	0.005	0.148	0.001	0.248	0.008	0.002	0.09	11.97	33.673	0.165	525.09	2.24
†3.0	33.981	0.010	0.024	0.073	0.005	0.219	0.001	0.286	0.003	0.002	0.17	9.22	33.675	0.350	525.12	4.74
†3.2	33.669	0.005	0.023	0.054	0.004	0.154	0.001	0.252	0.009	0.002	0.24	19.05	33.433	0.182	521.84	2.47
†3.4	35.158	0.006	0.025	0.051	0.005	0.138	0.005	0.085	0.003	0.002	3.78	10.35	33.607	0.260	524.20	3.52
†3.6	34.178	0.006	0.022	0.050	0.006	0.226	0.002	0.311	0.002	0.002	0.43	8.45	33.767	0.266	526.36	3.59
†4.0	33.794	0.011	0.024	0.038	0.007	0.100	0.001	0.496	0.020	0.002	0.09	12.11	33.560	0.399	523.56	5.41
5.0	33.530	0.005	0.031	0.044	0.008	0.155	0.001	0.390	0.011	0.004	0.03	7.76	33.239	0.226	519.21	3.07

Table cont'd.

Table 4. *cont'd.*

Laser Power (%)	$\frac{^{40}Ar}{^{39}Ar}$	$\pm\frac{^{40}Ar}{^{39}Ar}$	$\frac{^{38}Ar}{^{39}Ar}$	$\pm\frac{^{38}Ar}{^{39}Ar}$	$\frac{^{37}Ar}{^{39}Ar}$	$\pm\frac{^{37}Ar}{^{39}Ar}$	$\frac{^{36}Ar}{^{39}Ar}$	$\pm\frac{^{36}Ar}{^{39}Ar}$	$\frac{Ca}{K}$	$\frac{Cl}{K}$	$\%^{40}Ar$	$\%^{39}Ar^{a}$	$\frac{^{40}Ar^{*}}{^{39}Ar_{K}}$	$\pm\frac{^{40}Ar^{*}}{^{39}Ar_{K}}$	Apparent age (Ma)	$\pm 2\sigma$
***Sample 16**, phlogopite, UTM (516399, 7230074), J = 0.010042±0.000010, volume $^{39}Ar_{K}$ = 703.71 x 10^{15} cm^{3}, integrated age = 540.57±0.84 Ma*																
2.0	48.869	0.014	0.364	0.065	0.442	0.064	0.124	0.062	2.408	0.075	69.96	0.13	13.924	2.260	236.12	35.92
2.2	25.996	0.009	0.157	0.059	1.604	0.024	0.025	0.158	10.119	0.032	21.87	0.37	19.615	1.204	324.37	18.23
2.4	39.740	0.010	0.127	0.065	2.787	0.018	0.026	0.141	17.741	0.025	13.58	0.33	33.644	1.165	525.11	15.79
2.6	40.218	0.008	0.076	0.050	1.018	0.017	0.013	0.141	6.418	0.013	6.39	0.65	37.204	0.609	572.68	8.04
2.8	46.157	0.005	0.101	0.021	0.153	0.022	0.006	0.063	0.949	0.020	2.95	2.26	44.596	0.258	667.63	3.22
3.0	42.560	0.005	0.085	0.026	0.033	0.046	0.003	0.098	0.187	0.016	1.34	2.65	41.797	0.233	632.26	2.97
3.2	38.997	0.005	0.068	0.021	0.021	0.055	0.001	0.158	0.126	0.012	0.54	7.27	38.671	0.199	591.93	2.60
3.3	35.311	0.004	0.045	0.036	0.013	0.056	0.001	0.350	0.076	0.007	0.24	6.38	35.107	0.164	544.82	2.20
3.4	35.160	0.004	0.048	0.024	0.011	0.045	0.001	0.303	0.060	0.008	0.38	4.87	34.891	0.172	541.92	2.30
3.5	35.119	0.005	0.058	0.033	0.014	0.050	0.001	0.346	0.077	0.010	0.14	5.94	34.944	0.171	542.63	2.30
3.6	34.576	0.004	0.058	0.025	0.026	0.037	0.000	0.203	0.161	0.010	0.16	9.26	34.420	0.146	535.58	1.97
'3.7	34.050	0.005	0.064	0.017	0.028	0.028	0.001	0.245	0.171	0.012	0.28	7.71	33.845	0.166	527.83	2.25
'3.8	34.000	0.005	0.065	0.021	0.026	0.024	0.001	0.259	0.157	0.012	0.22	6.80	33.813	0.164	527.39	2.22
'3.9	33.918	0.005	0.061	0.026	0.022	0.032	0.001	0.275	0.131	0.011	0.21	6.12	33.727	0.173	526.23	2.34
'4.0	33.910	0.004	0.059	0.017	0.018	0.045	0.001	0.182	0.102	0.010	0.24	5.47	33.702	0.158	525.90	2.14
'4.1	33.817	0.005	0.052	0.025	0.017	0.038	0.000	0.222	0.098	0.009	0.08	6.61	33.673	0.157	525.51	2.13
'4.2	34.015	0.005	0.062	0.028	0.019	0.048	0.001	0.394	0.107	0.011	0.06	4.24	33.848	0.173	527.87	2.34
'4.4	33.903	0.004	0.051	0.029	0.012	0.043	0.000	0.392	0.068	0.008	0.11	8.01	33.758	0.150	526.66	2.03
'4.6	33.839	0.005	0.076	0.014	0.013	0.068	0.001	0.304	0.071	0.014	0.13	5.39	33.668	0.164	525.43	2.22
'4.9	33.865	0.004	0.055	0.026	0.006	0.023	0.000	0.341	0.032	0.009	0.13	9.53	33.719	0.143	526.13	1.94

Neutron flux monitor: 28.02 Ma Fish Canyon Tuff sanidine (Fcs)

Isotope production ratios: $(^{40}Ar/^{39}Ar)_{K}$ = 0.0302±0.00006, $(^{37}Ar/^{39}Ar)_{Ca}$ = 1416.4±0.5, $(^{36}Ar/^{39}Ar)_{Ca}$ = 0.3952±0.0004, Ca/K = 1.83±0.01 $(^{37}Ar_{Ca}/^{39}Ar_{K})$

[a] Fraction of ^{39}Ar as percent of total run

[*] Step used in plateau age calculations

All uncertainties quoted at 2σ level

Table 5. ^{40}Ar-^{39}Ar results for phlogopite separates from the Quartet Mountain Lamprophyre sample 18

Laser Power (%)[a]	$\frac{^{40}Ar}{^{39}Ar}$	$\pm\frac{^{40}Ar}{^{39}Ar}$	$\frac{^{38}Ar}{^{39}Ar}$	$\pm\frac{^{38}Ar}{^{39}Ar}$	$\frac{^{37}Ar}{^{39}Ar}$	$\pm\frac{^{37}Ar}{^{39}Ar}$	$\frac{^{36}Ar}{^{39}Ar}$	$\pm\frac{^{36}Ar}{^{39}Ar}$	volume $^{39}Ar_K$ ($\times 10^{-11}$ cm^3)	$\%^{40}Ar$	$\%^{39}Ar$[b]	$\frac{^{40}Ar^*}{^{39}Ar_K}$	$\pm\frac{^{40}Ar^*}{^{39}Ar_K}$	Apparent age (Ma)	$\pm 2\sigma$[c]
Sample 18 *phlogopite, UTM (546987, 7219808), J = 0.01948080±0.00019*[d]															
Aliquot 1															
3.0	17.889	0.224	0.012	0.011	0.503	0.012	0.0067	0.0006	1.6059	11.1	2.3	15.898	0.276	486.76	7.41
'5.0	17.721	0.115	0.011	0.011	0.044	0.001	0.0013	0.0001	6.2683	2.2	8.8	17.326	0.117	524.66	3.08
'7.0	23.937	0.645	0.012	0.011	0.131	0.022	0.0240	0.0018	0.4134	29.6	0.6	16.852	0.783	512.16	20.71
'9.0	20.372	0.295	0.012	0.011	0.074	0.013	0.0120	0.0017	0.7618	17.4	1.1	16.824	0.581	511.43	15.39
45.0	24.098	0.897	0.012	0.012	0.106	0.036	0.0200	0.0030	0.2921	24.6	0.4	18.176	1.214	546.86	31.51
Aliquot 2															
3.0	22.361	0.578	0.012	0.012	0.132	0.022	0.0230	0.0009	0.3818	30.4	0.5	15.553	0.637	477.47	17.19
'5.0	18.134	0.298	0.012	0.011	0.145	0.008	0.0039	0.0007	0.8766	6.4	1.2	16.968	0.351	515.24	9.27
'7.0	17.424	0.056	0.011	0.011	0.021	0.001	0.0009	0.0001	7.4661	1.6	10.5	17.145	0.066	519.89	1.73
45.0	36.420	3.535	0.043	0.012	0.783	0.095	0.0762	0.0221	0.0721	61.8	0.1	13.907	7.039	432.50	194.85
Aliquot 3															
'3.0	16.723	0.324	0.014	0.011	1.196	0.029	0.0087	0.0016	0.8787	15.3	1.2	14.161	0.564	439.53	15.54
'5.0	17.549	0.099	0.009	0.011	0.035	0.001	0.0013	0.0002	6.8288	2.2	9.6	17.156	0.108	520.18	2.84
'7.0	17.781	0.128	0.010	0.011	0.047	0.002	0.0022	0.0005	2.8642	3.6	4	17.144	0.189	519.89	4.98
'9.0	18.388	0.279	0.009	0.011	0.073	0.005	0.0050	0.0004	1.3447	8	1.9	16.909	0.296	513.67	7.83
45.0	34.022	1.484	0.030	0.011	0.367	0.044	0.0597	0.0060	0.1563	51.9	0.2	16.377	2.212	499.55	58.95
Aliquot 4															
'3.0	19.123	0.425	0.019	0.011	4.536	0.105	0.0156	0.0021	0.5449	24.1	0.8	14.518	0.739	449.33	20.24
'5.0	17.843	0.142	0.009	0.011	0.103	0.003	0.0021	0.0004	3.9277	3.4	5.5	17.236	0.177	522.28	4.65
'7.0	18.424	0.177	0.010	0.011	0.070	0.003	0.0038	0.0006	1.7901	6.1	2.5	17.306	0.245	524.14	6.43
45.0	23.750	0.736	0.021	0.011	0.273	0.021	0.0143	0.0036	0.3212	17.8	0.5	19.529	1.284	581.63	32.70
Aliquot 5															
'3.0	16.935	0.143	0.012	0.011	0.569	0.019	0.0030	0.0005	2.5019	5.3	3.5	16.039	0.194	490.53	5.19
'5.0	17.704	0.190	0.009	0.011	0.040	0.002	0.0009	0.0001	6.9332	1.6	9.7	17.424	0.191	527.25	5.00
'7.0	17.958	0.188	0.010	0.011	0.047	0.003	0.0021	0.0003	2.4183	3.4	3.4	17.351	0.200	525.32	5.24
'9.0	19.697	0.339	0.012	0.011	0.059	0.025	0.0079	0.0018	0.7793	11.9	1.1	17.359	0.630	525.52	16.55
45.0	25.017	1.143	0.011	0.012	0.229	0.019	0.0304	0.0039	0.2626	35.9	0.4	16.025	1.480	490.15	39.63
Aliquot 6															
'3.0	17.574	0.300	0.013	0.011	0.272	0.019	0.0039	0.0005	1.3395	6.6	1.9	16.419	0.324	500.66	8.63
'5.0	17.689	0.085	0.011	0.011	0.026	0.002	0.0012	0.0003	4.8896	1.9	6.9	17.344	0.112	525.13	2.95
'7.0	17.748	0.160	0.012	0.011	0.074	0.003	0.0014	0.0008	2.3506	2.3	3.3	17.332	0.273	524.83	7.17
'9.0	18.912	0.336	0.012	0.011	0.071	0.006	0.0053	0.0011	1.0208	8.2	1.4	17.357	0.464	525.47	12.20
45.0	29.728	1.440	0.010	0.014	0.202	0.040	0.0490	0.0062	0.1601	48.7	0.2	15.240	2.231	468.99	60.47
Aliquot 7															
'3.0	23.251	1.739	0.052	0.012	7.200	0.292	0.0466	0.0141	0.1229	59.2	0.2	9.476	4.470	305.62	132.67
'5.0	17.698	0.109	0.009	0.011	0.317	0.012	0.0017	0.0004	3.5048	2.9	4.9	17.193	0.168	521.16	4.43
'7.0	18.240	0.317	0.011	0.011	0.099	0.013	0.0037	0.0006	1.0151	6.1	1.4	17.134	0.350	519.60	9.23
45.0	23.146	1.341	0.020	0.011	0.696	0.039	0.0252	0.0064	0.1705	32.2	0.2	15.691	2.278	481.17	61.31
Aliquot 8															
3.0	37.632	6.214	0.025	0.023	1.513	0.196	0.1246	0.0176	0.0359	97.8	0.1	0.821	7.178	28.64	248.58
5.0	17.336	0.169	0.008	0.011	0.053	0.008	0.0013	0.0003	2.3534	2.3	3.3	16.942	0.189	514.55	5.01
7.0	17.909	0.227	0.009	0.011	0.079	0.005	0.0032	0.0008	1.2838	5.2	1.8	16.970	0.329	515.28	8.68
'9.0	18.245	0.394	0.010	0.011	0.076	0.009	0.0032	0.0005	1.0726	5.2	1.5	17.294	0.403	523.83	10.59
'45.0	17.751	0.206	0.009	0.011	0.024	0.009	0.0018	0.0003	2.1886	5.2	3.1	17.229	0.223	522.11	5.87

[a] As measured by laser in % of full nominal power (10 W); [b] Fraction ^{39}Ar as percent of total run; [c] Errors are analytical only and do not reflect error in irradiation parameter J; [d] Nominal J, referenced to FCT-SAN = 28.03 Ma (Renne et al., 1994).

' Step used in plateau age calculations

All uncertainties quoted at 2σ level

Table 6. ^{204}Pb corrected U-Pb SHRIMP analytical data for crustal xenoliths from sample 2.

Spot name	U (ppm)	Th (ppm)	Th/U	Pb* (ppm)	f(206)^{204}	^{207}*Pb/^{235}*U	±^{207}Pb/^{235}U	^{206}*Pb/^{238}*U	±^{206}Pb/^{238}U	Corr. coeff.	^{207}*Pb/^{206}*Pb	±^{207}Pb/^{206}Pb	^{206}Pb/^{238}U	±^{206}Pb/^{238}U	^{207}Pb/^{206}Pb	±^{207}Pb/^{206}Pb	Discordance (%)
9044-2.1	1334	35	0.03	673.7	0.03	14.63	0.37	0.5876	0.0137	0.933	0.1806	0.0016	2980	56	2659	15	12
9044-5.1	206	193	0.97	36.8	0.33	3.32	0.21	0.2076	0.0103	0.780	0.1160	0.0046	1216	55	1896	72	36
9044-7.1	101	93	0.96	28.5	0.26	4.50	0.41	0.3291	0.0227	0.754	0.0992	0.0060	1834	110	1609	112	-14
9044-9.1	165	134	0.84	56.2	0	9.18	0.26	0.3960	0.0105	0.925	0.1682	0.0018	2151	48	2540	18	15
9044-11.1	1040	8	0.01	186.9	0	2.34	0.05	0.2093	0.0041	0.950	0.0810	0.0005	1225	22	1221	13	0
9044-19.1	817	18	0.02	93.0	0	1.33	0.03	0.1326	0.0024	0.867	0.0727	0.0007	803	13	1006	21	20
9044-19.2	159	141	0.91	23.9	0.84	2.14	0.12	0.1733	0.0046	0.479	0.0895	0.0043	1030	25	1415	93	27
9044-21.1	1455	99	0.07	222.4	0.12	1.96	0.05	0.1777	0.0033	0.705	0.0800	0.0015	1054	18	1198	37	12
9044-23.1	682	16	0.02	100.3	0	1.86	0.04	0.1713	0.0030	0.757	0.0789	0.0012	1019	17	1170	30	13
9044-23.2	404	60	0.15	144.8	0.09	9.42	0.41	0.4165	0.0116	0.644	0.1640	0.0054	2245	53	2498	56	10
9044-27.1	873	7	0.01	144.4	0.01	2.16	0.04	0.1926	0.0034	0.884	0.0813	0.0007	1135	18	1228	18	8
9044-30.1	886	48	0.06	134.6	0	1.95	0.04	0.1768	0.0032	0.909	0.0801	0.0007	1050	17	1199	16	12
9044-51.1	2231	116	0.05	387.4	0.01	2.28	0.05	0.2021	0.0037	0.838	0.0817	0.0010	1187	20	1237	23	4
9044-52.1	1356	876	0.67	224.0	0.09	2.37	0.06	0.1921	0.0039	0.870	0.0894	0.0010	1133	21	1412	22	20
9044-65.1	225	133	0.61	50.5	0.34	3.60	0.19	0.2607	0.0122	0.889	0.1001	0.0024	1493	63	1626	45	8
9044-69.1	648	7	0.01	113.2	0.18	2.24	0.05	0.2028	0.0040	0.843	0.0800	0.0010	1190	22	1197	25	1
9044-71.1	662	47	0.07	76.8	0.17	1.35	0.06	0.1348	0.0044	0.781	0.0728	0.0019	815	25	1007	53	19
9044-77.1	784	14	0.02	111.6	0.01	1.73	0.04	0.1657	0.0032	0.846	0.0757	0.0009	988	18	1088	24	9
9044-78.1	218	91	0.43	54.9	0.28	4.42	0.19	0.2925	0.0065	0.505	0.1096	0.0041	1654	32	1792	69	8
9044-84.1	1206	53	0.05	305.2	0.00	4.32	0.16	0.2946	0.0084	0.773	0.1063	0.0025	1664	42	1737	43	4
9044-85.1	1778	62	0.04	605.5	0	6.48	0.21	0.3964	0.0090	0.707	0.1186	0.0027	2152	41	1936	41	11
9046-3.1	2728	264	0.10	481.5	0	2.22	0.04	0.2055	0.0034	0.969	0.0783	0.0003	1205	18	1155	8	-4
9046-3.2	868	7	0.01	164.7	0.05	2.59	0.05	0.2208	0.0039	0.925	0.0852	0.0006	1286	21	1320	14	3
9046-4.1	576	46	0.08	96.1	0.28	2.06	0.04	0.1936	0.0034	0.860	0.0771	0.0008	1141	19	1125	21	-1
9046-5.1	1446	16	0.01	336.3	0.07	3.65	0.07	0.2705	0.0044	0.903	0.0978	0.0008	1543	22	1582	14	2
9046-6.1	697	1	0.00	159.0	0	3.42	0.07	0.2655	0.0047	0.921	0.0935	0.0007	1518	24	1499	14	-1
9046-6.2	2170	216	0.10	363.6	0.00	2.10	0.04	0.1951	0.0034	0.956	0.0780	0.0004	1149	18	1148	11	0
9046-8.1	3031	286	0.09	523.6	0.00	2.18	0.04	0.2011	0.0033	0.970	0.0787	0.0003	1181	18	1166	8	-1
9046.13.1	222	25	0.11	36.1	1.11	1.93	0.10	0.1872	0.0038	0.383	0.0749	0.0037	1106	21	1066	100	-4
9046-14.1	260	51	0.20	43.2	0.62	2.15	0.10	0.1924	0.0046	0.527	0.0812	0.0031	1134	25	1227	75	8
9046-15.1	3186	228	0.07	559.2	0.02	2.19	0.04	0.2042	0.0034	0.973	0.0777	0.0003	1198	18	1138	8	-5
9046-15.2	1430	29	0.02	330.7	0.03	3.58	0.06	0.2691	0.0046	0.949	0.0965	0.0005	1536	23	1557	11	1
9046-15.3	3828	342	0.09	673.1	0.05	2.19	0.04	0.2046	0.0034	0.971	0.0777	0.0003	1200	18	1139	8	-5
9046-17.1	704	2	0.00	126.2	0.18	2.39	0.05	0.2082	0.0036	0.911	0.0831	0.0007	1219	19	1272	15	4
9046-18.1	1461	15	0.01	322.4	0	3.22	0.07	0.2569	0.0050	0.885	0.0909	0.0009	1474	26	1445	19	-2
9046-19.1	1480	27	0.02	349.1	0	3.66	0.07	0.2748	0.0049	0.969	0.0967	0.0004	1565	25	1561	8	0
9046-20.1	2598	236	0.09	445.1	0.11	2.18	0.04	0.1992	0.0033	0.949	0.0792	0.0004	1171	18	1178	11	1
9046-21.1	662	51	0.08	112.4	0	2.18	0.04	0.1976	0.0033	0.875	0.0800	0.0007	1162	18	1198	18	3
9047-4.1	230	60	0.26	67.8	0.00	5.60	0.13	0.3422	0.0069	0.876	0.1187	0.0013	1897	33	1937	20	2
9047-4.2	340	29	0.09	58.1	0	2.19	0.05	0.1992	0.0038	0.801	0.0796	0.0011	1171	20	1188	28	1
9047-12.1	494	4	0.01	90.7	0.19	2.40	0.07	0.2134	0.0048	0.803	0.0814	0.0014	1247	25	1232	33	-1
9047-14.1	547	4	0.01	100.2	0	2.48	0.05	0.2131	0.0038	0.890	0.0843	0.0008	1245	20	1300	18	4
9047-16.1	450	4	0.01	84.1	0	2.62	0.08	0.2178	0.0040	0.583	0.0874	0.0022	1270	21	1370	50	7
9047-17.1	586	284	0.49	159.4	0.00	4.76	0.14	0.3168	0.0057	0.630	0.1089	0.0024	1774	28	1781	41	0
9047-36.1	157	139	0.88	26.0	0.23	2.03	0.07	0.1926	0.0042	0.636	0.0765	0.0020	1136	23	1109	53	-2
9047-37.1	275	99	0.36	45.1	0.21	2.07	0.06	0.1906	0.0036	0.707	0.0789	0.0015	1125	19	1170	37	4
9047-37.2	215	65	0.30	38.5	0.12	2.68	0.12	0.2078	0.0043	0.444	0.0934	0.0039	1217	23	1497	79	19
9047-37.3	575	9	0.02	96.7	0	2.17	0.04	0.1958	0.0034	0.861	0.0803	0.0008	1153	19	1205	20	4

Table cont'd.

Table 6. *cont'd.*

Spot name	U (ppm)	Th (ppm)	Th/U	Pb* (ppm)	%(206)^{204}	^{207}*Pb/^{235}*U	±	^{206}*Pb/^{238}*U	±	Corr. coeff.	^{207}*Pb/^{206}*Pb	±	^{206}Pb/^{238}U	±	^{207}Pb/^{206}Pb	±	Discordance (%)
9048-4.1	1065	48	0.04	194.7	0	2.67	0.06	0.2158	0.0038	0.769	0.0899	0.0013	1259	20	1423	28	12
9048-7.1	1237	61	0.05	205.8	0.13	2.08	0.04	0.1934	0.0035	0.908	0.0781	0.0006	1140	19	1150	16	1
9048-10.1	461	183	0.40	119.5	0	4.45	0.22	0.3020	0.0116	0.766	0.1069	0.0034	1701	57	1747	59	3
9048-13.1	1012	93	0.09	170.5	0.12	2.11	0.04	0.1958	0.0033	0.829	0.0782	0.0009	1153	18	1153	23	0
9048-13.2	1100	80	0.07	176.0	0.21	1.97	0.04	0.1860	0.0031	0.884	0.0767	0.0007	1100	17	1114	18	1
9049-2.1	226	477	2.11	38.4	0.69	2.09	0.10	0.1959	0.0040	0.413	0.0774	0.0035	1153	22	1132	90	-2
9049-5.1	229	310	1.40	38.2	0	2.31	0.06	0.1942	0.0040	0.821	0.0862	0.0012	1144	21	1343	27	15
9049-6.1	73	31	0.43	12.5	1.78	2.30	0.14	0.1953	0.0053	0.434	0.0854	0.0048	1150	28	1324	109	13
9049-6.2	472	313	0.66	82.8	0.47	2.19	0.05	0.2032	0.0037	0.761	0.0783	0.0012	1192	20	1153	31	-3
9049-6.3	126	81	0.64	20.3	1.54	2.01	0.12	0.1848	0.0043	0.391	0.0791	0.0044	1093	24	1174	109	7
9049-7.1	207	97	0.47	34.6	0.39	2.18	0.08	0.1939	0.0041	0.578	0.0815	0.0024	1143	22	1234	58	7
9049-9.1	219	502	2.37	35.1	1.02	1.92	0.11	0.1847	0.0088	0.792	0.0754	0.0028	1093	48	1079	73	-1

Uncertainties at 1σ (absolute) are calculated by numerical propagation of all known sources of error. Pb* denotes radiogenic Pb. %(206)^{204} refers to mole percent of total ^{206}Pb that is due to common Pb, calculated using the common ^{204}Pb method; common Pb composition used is the surface blank. Corr. coeff. = correlation coefficient. Discordance relative to the origin = 100 × [1-(^{206}Pb/^{238}U age)/(^{207}Pb/^{206}Pb age)].

Table 7. Compilation of western Laurentian Grenville-age structural relationships and geochronometric dates

	Location	Description	Method	Interpreted Age	Reference
1	Lemhi Pass, Idaho	molybdenite mineralization	Re-Os molybdenite	1055±4 Ma	Gillerman et al., 2002; Jercinovic et al., 2002
2	Lemhi Pass, Idaho	Th-REE mineralization	U-Th-Pb- monazite/thorite	800-1100 Ma	Gillerman et al., 2002
3	Lowell, Idaho	detrital zircon in quartzite	U-Pb zircon	1.2-1.1 Ga	Lund et al., 2004
4	Clearwater Complex, Idaho	garnet ampibolite; pelitic schist	Lu-Hf garnet	1149±4; 1056±57, 1006±5 Ma	Vervoort et al., 2005
5	Boehls Butte-Clearwater Complex, Idaho	amphibolite-grade schist	Lu-Hf garnet-whole rock	ca. 1.01 Ga	Sha et al., 2004
6	Priest River mm. Complex, Idaho	high grade metamorphic rocks	U-Pb zircon‡	ca. 993-1096 Ma	Doughty, 2004
7	Buffalo Hump Formation, E. Washington	detrital zircon in quartzite	U-Pb zircon†	ca. 1.1 Ga	Ross et al., 1992
8	Moyie Sill, Purcell Supergroup, SE B.C.	zircon and titanite in metagabbro	U-Pb zircon/titanite†	ca. 1.0-1.1 Ga	Anderson and Davis, 1995
9	Moyie Sill, Purcell Supergroup, SE B.C.	titanite in metagabbro sill	U-Pb titanite†	ca. 1.0-1.1 Ga	Anderson and Davis, 1995
10	Cross diatreme, SE B.C.	xenocrystic zircon in diatreme	U-Pb zircon†	1066.4±2.3	Parrish and Reichenbach, 1991
11	Joff diatreme, SE B.C.	xenocrystic zircon in diatreme	U-Pb zircon†	1045.5±7.0	Parrish and Reichenbach, 1991
12	Nicola Horst, southern B.C.	felsic clast in Bob Lake assemblage	U-Pb zircon†	ca. 1.04 Ga	Erdmer et al., 1997
13	Mount Wilson Formation, SE B.C.	detrital zircon in Ordovician s.stone	U-Pb zircon†	ca. 1030 (n=9), 1053 Ma (n=3)	Gehrels and Ross, 1998
14	Horsethief Creek Group, eastern B.C.	granitic boulder in Windermere S. Group	U-Pb zircon†	1189±33 Ma	Ross et al., 1992
15	Coates Lake diatreme, western N.W.T.	2 granitoid xenoliths	U-Pb zircon†	ca. 1140 Ma	Jefferson and Parrish, 1988;
16	Coppermine Homocline, N.W.T	deformation of Coppermine River Group	structural relationships	1128.7 +3.9/-3.5 Ma 1100-1267 Ma	Mortensen and Colpron, 1998 Hildebrand and Baragar, 1991
17	Wernecke Mountains, Yukon	4 gneissic xenoliths	U-Pb zircon‡	ca. 1150 Ma	This study
18	Farewell terrane, Alaska	basement metarhyolite to Farewell terrane	U-Pb zircon†	ca. 921 Ma, ca. 979 Ma	Bradley et. al, 2003

† Conventional TIMS U-Pb age; ‡ SHRIMP U-Pb age

APPENDICES

Appendix 1: Detailed Petrography of Crustal Xenoliths

Xenolith 9044

Xenolith 9044 is a finely banded light coloured gneiss of crustal affinity, approximately 3 cm across. Like most of the xenoliths found in sample 2, it has undergone significant rounding, leading to a broadly oval, prolate shape (Fig. A1). Minor reaction with the lamprophyre melt is evidenced by a thin marginal zone that is characterized by locally pervasive replacement of primary mineralogy by carbonate and sericite. Prior to crushing, and subsequent zircon separation and submission of powders for Sm-Nd analysis, all xenoliths were abraded using a Dremel^{TM} rotary grinder in an effort to remove as much of the marginal reaction rims as possible.

The xenolith is dominated by thin bands (<2 mm) composed of quartz and porphyroblasts set in a fine-grained matrix of granoblastic quartz. Quartz porphyroblasts commonly display undulose extinction, indicative of pre to syn-deformational growth. The quartz bands are separated by equally thin, discontinuous bands of garnet and sillimanite. Thin lenses dominated by sericite, with subordinate hematite are present, although not ubiquitous. Additionally, EDAX analyses positively identified K-feldspar as a sub-microscopic, irregularly-shaped mineral, occurring interstitially to quartz crystals.

The garnet grains are irregular in shape and heavily fractured, with fractures generally lined with iron-oxides and sericite. Garnet composition was estimated using EDAX, as 60 % pyrope and 40% almandine, with minor Ca. Sillimanite grains are irregular, approximately 0.05 mm across and set in a K-feldspar groundmass. Rutile, zircon and titanite are important accessory phases, and occur either as interstitial grains, or as mineral inclusions within quartz or garnet. Zircon crystals are dominantly oriented with c-axes parallel to the foliation direction. This observation supports the syn-kinematic rotation of the detrital zircon cores, but it does not provide definite evidence for syn-kinematic recrystallization or growth of metamorphic rims.

The metamorphic assemblage of xenolith 9044 implies upper amphibolite to granulite- facies metamorphism of an aluminous wacke protolith, under high temperatures and moderate pressures.

Xenolith 9046

Sample 9046 is a white-green, crudely foliated crustal xenolith, approximately 1.5 cm across. The xenolith has undergone significant retrograde metamorphism and or metasomatic alteration. Absence of phlogopite and cross-cutting carbonate veins argues against significant alteration during entrainment.

The xenolith foliated texture in manifested in thin-section by lenses composed dominantly of sericite, surrounded by a matrix of coarse crystalline to very fine carbonate and chlorite (Fig. A1). A relatively sericite-poor band, approximately 1.3 mm wide, contains abundant (>10%) anhedral, fractured

crystals of equant apatite (<0.3 mm across). Apatite grains show no indication of alteration along the fractures. In addition to apatite, the band is composed of euhedral sparry carbonate and chlorite mats, both of which are likely pseudomorphs after unidentified minerals.

The extensive retrograde metamorphism/ metasomatic alteration of xenolith 9046, makes the interpretation of its protolith very uncertain. Based on its very high sericite content and absence of quartz, it appears more likely that the xenolith was derived from an aluminous sedimentary protolith rather than a felsic peraluminous intrusive or extrusive rock.

Xenolith 9047

Xenolith 9047 is small, weakly foliated, ovoid inclusion approximately 2 cm long. A large veinlet, locally 0.2 mm wide and composed largely of fine-grained to sparry carbonate cuts the xenolith. In the thin-section, the veinlet can be traced back to the lamprophyre and it thus likely represents crystallized lamprophyre melt. Furthermore, the veinlet explains the anomalously high εNd value of xenolith 9047, which could be derived by approximately 10% contamination of the Wernecke Mountains Supergroup protolith with the lamprophyre melt (see Appendix 5 for more details).

The xenolith has undergone extensive retrograde metamorphism, as much of the xenolith is now composed of lenses of sericite juxtaposed against lenses of chlorite closely intergrown with microcrystalline potassic feldspar.

Within the chlorite-potassic feldspar lenses, very fine, massive to acicular, crystals of celestite $(Sr,Ba)SO_4$ were identified.

Small regions of xenolith 9047 escaped significant retrograde metamorphism, and thus likely still reflect the maximum P-T conditions that the xenolith was subjected to. Single grains or lenses of fine (0.1-0.2 mm), granoblastic, potassic feldspar, showing sericite alteration along margins are generally isolated, but sometimes occur in association with sillimanite. Sillimanite is fine grained (<0.1 mm), forming discontinuous lenses, and sometimes occurring as single grains intergrown with rutile and enclosed by garnet porphyroblasts. Garnet porphyroblasts are anhedral and heavily fractured, and contain significant rutile and opaque inclusions. Zircon crystals represent a very small population of xenolith 9047.

The preserved metamorphic assemblage of xenolith 9047 suggests granulite facies metamorphism of a pelitic protolith, under high temperatures and moderate pressures.

Xenolith 9048

Xenolith 9048 is a nearly circular, non-foliated inclusion, approximately 1.5 cm across. The apparent lack of foliation may however be an artifact of the way the xenolith was cut, rather than its characteristic feature.

The mineralogy of the xenolith is dominated by fine-grained, granoblastic heavily fractured crystals of sillimanite (Fig. A1). The sillimanite crystals are approximately equant in shape, lacking the high aspect ratios that commonly

typify sillimanite. The crystals are 0.3-1.2 mm long, and are closely intergrown. In addition to their atypical habit, the sillimanite crystals also display anomalously high birefringence, attributed to the excessive thickness of the polished thin-section (~0.35 mm). The single cleavage direction, parallel extinction, and length slow optical orientation of the crystals, however, are most consistent with their identification as sillimanite. Repeated EDAX analysis of the crystals demonstrated that they are pure Al_2SiO_5 with no noticeable substitution of Fe^{3+} or Mn^{3+} cations, thus removing the possibility that the crystals are high-Fe (>6 mol%) andalusite.

Extensive retrograde metamorphism of the xenolith is evident from large irregularly shaped lenses of sericite, which can in places be seen replacing sillimanite and potassium feldspar (Fig. A1). Relict, heavily altered potassium feldspar crystals occur as irregular patches surrounded by sericite. Coarse grained, heavily fractured garnet, is locally intergrown with sillimanite ± K-feldspar, is volumetrically minor. Garnet also shows signs of retrogression, being replaced by chlorite and sericite.

Other important minor mineral phases include rare zircon crystals, irregularly shaped rutile and minor opaques.

Xenolith 9049

Xenolith 9049 is an ovoid, finely laminated, green and white gneissic nodule. It is the largest xenolith encountered, its long axis measuring approximately 3 cm. The xenolith has undergone extensive retrograde

metamorphism, and has in part reacted with the lamprophyre magma, as evidenced by a carbonate veinlet approximately 1 mm wide, growth of post-kinematic unaligned phlogopite and phlogopite pseudomorphism of orthopyroxene (Fig. A1).

The texture of the xenolith is dominated by discontinuous lenses of polygonal, very fine grained feldspar altering to chlorite, and lenses and laminae that have been completely retrograded to carbonate, sericite, chlorite and a dark brown material inferred to be an extremely fine grained aggregate of carbonate, chlorite, sericite and clay. Lenses of fine grained feldspar, frequently contain, larger, irregularly shaped feldspar crystals that are commonly characterized by undulose extinction. EDAX determinations of feldspar grains have shown that they are Ca^{2+} free, and of approximate $Ab_{90}Or_{10}$ composition. Many of the lenses are likely boudins formed by tensional deformation of formerly continuous compositional bands.

An important mineralogical aspect of xenolith 9049 is the presence of coarse (>4 mm), relict crystals of Mg-rich orthopyroxene. The orthopyroxene has been in large part replaced by a Ca-Mg-Fe rich carbonate, opaque minerals, chlorite and a brown aggregate of microcrystalline unidentified minerals. It appears that orthopyroxene may once have formed a mono-mineralic band within the xenolith at least 0.5 mm thick.

The combination of prograde metamorphism, deformation, retrograde metamorphism and metasomatic alteration during entrainment, does not allow for a confident interpretation of the xenolith's protolith. Thus, based on the presence

of Mg-rich orthopyroxene, absence of quartz, relatively low abundance of aluminosilicate phases and absence of detrital zircon grains (see U-Pb geochronology section) xenolith 9049 is tentatively interpreted as an orthogneiss.

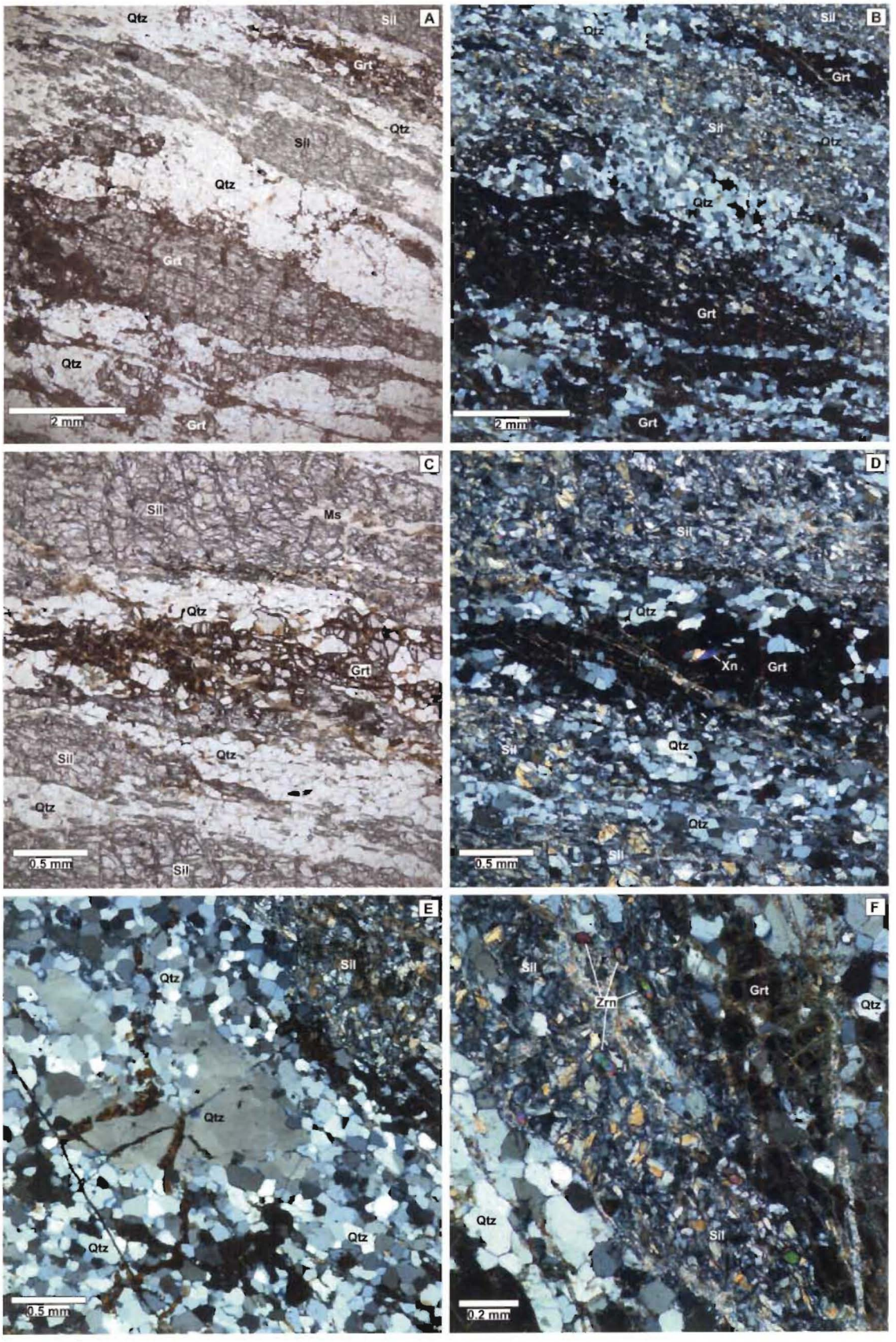
A
Qtz
Sil
Grt
Qtz
Sil
Qtz
Grt
Qtz
2 mm
Grt
B
Qtz
Sil
Grt
Sil
Qtz
Qtz
Grt
2 mm
Grt
C
Sil
Ms
Qtz
Grt
Sil
Qtz
Qtz
0.5 mm
Sil
D
Sil
Qtz
Xn
Grt
Sil
Qtz
Qtz
0.5 mm
Sil
E
Qtz
Sil
Qtz
Qtz
Qtz
0.5 mm
F
Sil
Zrn
Grt
Qtz
Qtz
Sil
0.2 mm

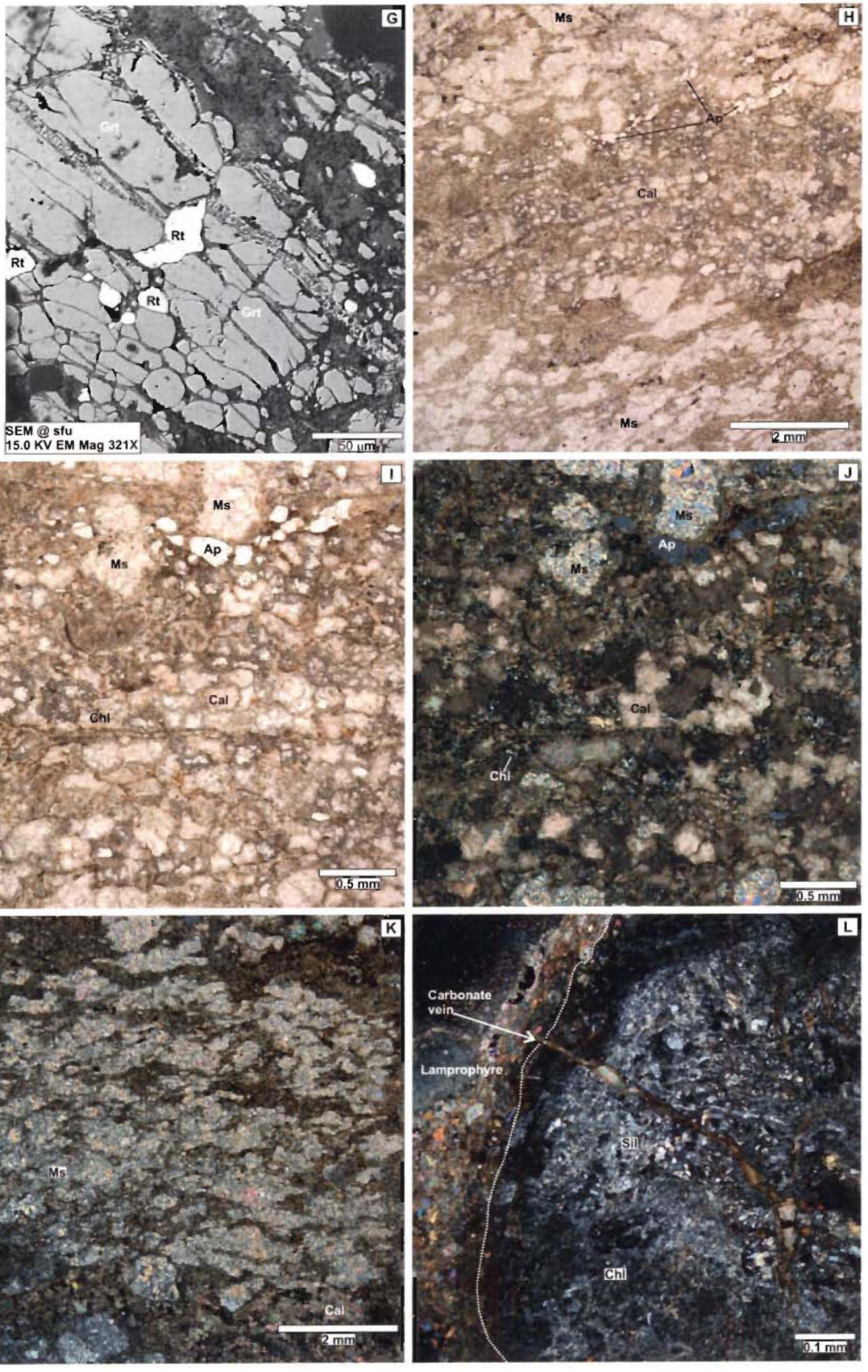
G
Grt
Rt
Rt
Rt
Grt
SEM @ sfu
15.0 KV EM Mag 321X
50 µm
H
Ms
Ap
Cal
Ms
2 mm
I
Ms
Ap
Ms
Cal
Chl
0.5 mm
J
Ms
Ap
Ms
Cal
Chl
0.5 mm
K
Ms
Cal
2 mm
L
Carbonate vein
Lamprophyre
Sil
Chl
0.1 mm

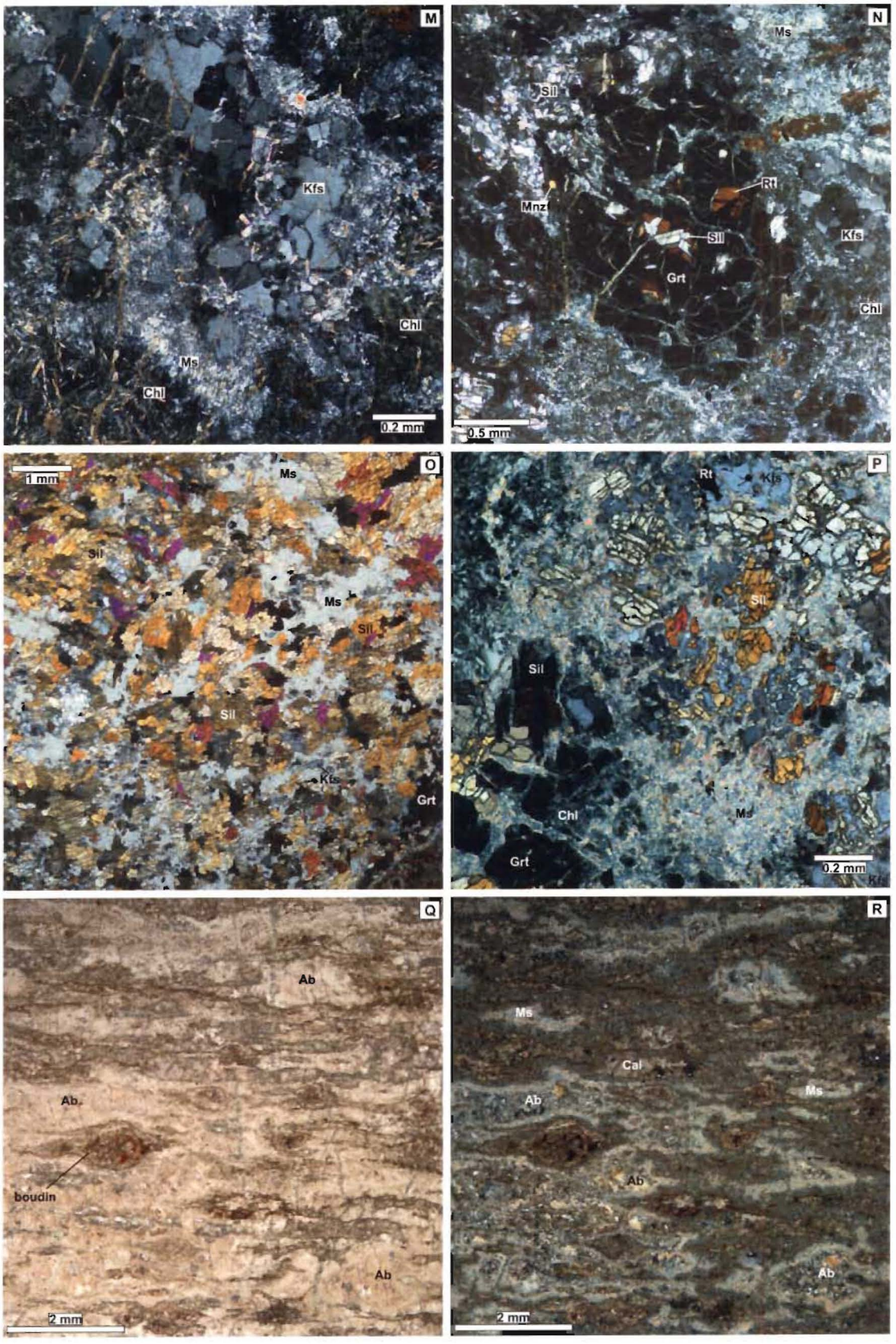
M
Kfs
Chl
Ms
Chl
0.2 mm
N
Ms
Sil
Rt
Mnz
Sil
Kfs
Grt
Chl
0.5 mm
O
1 mm
Ms
Sil
Ms
Sil
Sil
Kfs
Grt
P
Rt
Kfs
Sil
Sil
Chl
Ms
Grt
0.2 mm
Q
Ab
Ab
boudin
Ab
2 mm
R
Ms
Cal
Ab
Ms
Ab
Ab
2 mm

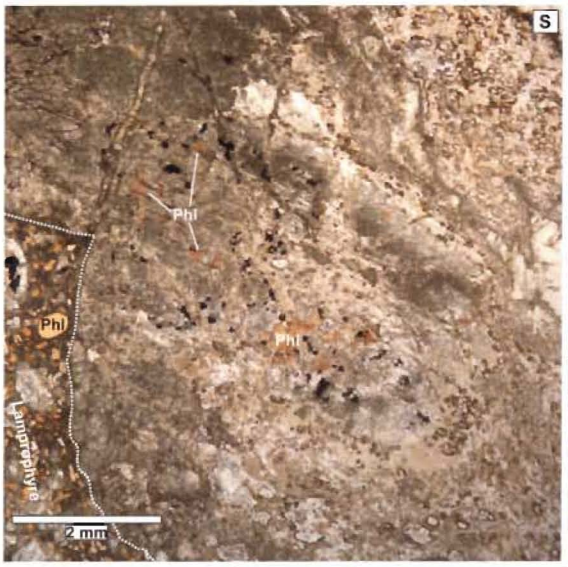
S
Phl
Phl
Phl
Lamprophyre
2 mm

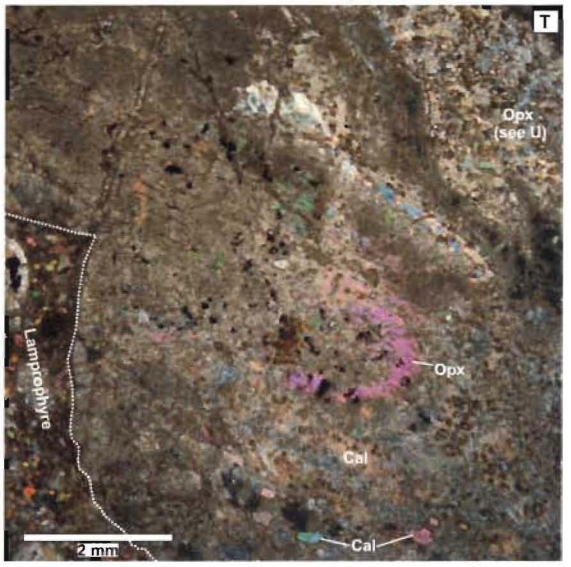
T
Opx
(see U)
Lamprophyre
Opx
Cal
2 mm
Cal

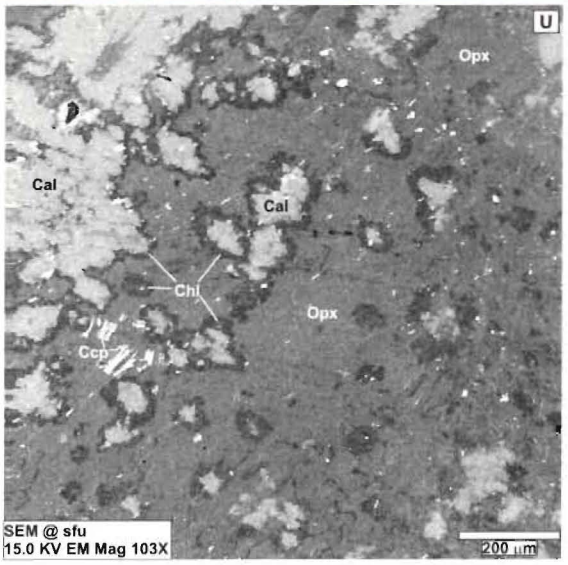
U
Opx
Cal
Cal
Chl
Opx
Ccp
SEM @ sfu
15.0 KV EM Mag 103X
200 µm

Figure A1. Representative photomicrographs of crustal xenoliths 9044,9046, 9047, 9048 and 9049. **A,B,C,D,E,F,G)** Representative photomicrographs of xenolith 9044. **A,B)** Representative photomicrographs in plane and cross-polarized light showing the finely banded texture of the xenolith. The prominent bands are composed of quartz, garnet and sillimanite. **C,D)** A band of heavily fractured hypidioblastic garnet crystals, enveloped on either side by quartz and sillimanite bands as seen in plane and cross-polarized light. Garnet fractures are commonly lined with iron oxides and sericite. A large (~0.3 mm long) crystal of xenotime is located in the centre of the garnet band. **E)** A cross-polarized light photomicrograph of a quartz porphyroblast, composed of a number of sub-domains, surrounded by fine grained, euhedral to subhedral quartz grains. The porphyroblast shows **F)** A cross-polarized light image of a sillimanite-garnet band, containing abundant subhedral zircon crystals. The zircon crystals are orinted with their c-axes parallel to subparallel to the foliation direction. **G**) A backscatter electron image of a heavily fractured garnet poikiloblast containing very fine grained biotite inclusions.

H,I,J,K) Representative photomicrographs of xenolith 9046 in plane and cross-polarized light. **H)** A representative plane-polarized photomicrograph of a sericite-poor band containing crystals of fractured apatite and sparry carbonate. **I and J)** Close-up plane and cross-polarized photomicrographs of the band shown in **H). K)** Crudely foliated appearance of 9046 in cross-polarized light. The fine-grained, first-order grey to second-order blue birefringent mats are composed of sericite. The irregular shaped, dark-brown material is dominatly composed of very fine grained carbonate with chlorite and clay (?).

L,M,N) Representative photomicrographs of xenolith 9047 in cross-polarized light. **L)** Photomicrograph showing a ~0.2 mm wide vein composed largely of sparry carbonate crystals. The vein originates from within the host lamprophyre and accounts for the anomalously positive eNd value of xenolith 9047. **M)** Representative photomicrograph of a lens of relict granoblastic K-feldspar, altering to sericite. Also shown, as the darker chlorite alteration. **N)** A photomicrograph of a large garnet crystal, with rutile, sillimanite and monazite inclusions.

O,P) Representative photomicrographs of xenolith 9048 in cross-polarized light. **O)** Representative image of the xenolith showing the highly fractured crystals of sillimanite and the extensive sericite alteration. **P)** A photomicrograph, showing the alteration of K-feldspar and sillimanite to sericite. Also evident is the alteration of garnet to chlorite and sericite. Note the parallel extinction of sillimanite.

Q,R,S,T,U) Representative photomicrographs of xenolith 9049. **Q,R)** Plane and cross-polarized image of 9049 showing its foliated texture and minearalogy dominated by lenses of alkali feldspar, carbonate, sericite, chlorite and a very fine grained dark-brown material. Note the microscopic boudin in the centre-left of the photomicrographs. **S,T)** Plane and cross-polarized image of a >0.5 mm wide orthopyroxene band. The anomalous first-order purple birefringence of orthopyroxene is due to >0.3 mm thin-section thickness. Orthopyroxene has largely been replaced by carbonate, opaque minerals, chlorite and a fine-grained brown aggregate. Pseudomorphism by phlogopite during entrainment is also evident. **U)** Back-scatter electon image of a highly altered ortopyroxene crystal in the upper-right corner. The light-grey anhedral crystals of carbonate are rimmed by black rims of chlorite. The medium grey host material is Mg-rich orthopyroxene. The white, equant to acicular crystals are foliation-parallel chalcopyrite.

Abbreviations: Ab=albite, Ap=apatite, Bt=biotite, Cal=calcite, Ccp=chalcopyrite, Chl=chlorite, Grt=garnet, Kfs=K-feldspar, Mnz=monazite, Ms=sericite, Opx=orthopyroxene, Phl=phlogopite, Qtz= quartz, Rt=rutile, Sil=sillimanite, Trd=tridymite, Zrn=zircon (after Kretz, 1983); Xn=xenotime.

Appendix 2: Sample Preparation and Methodology

New Ar-Ar Phlogopite Geochronology of the Quartet Mountain Lamprophyres

Four lamprophyre dykes were selected for Ar-Ar geochronology, to supplement an earlier analysis reported by Thorkelson (2000; see clarification in Thorkelson et al., 2003; Table 5). Sample locations are shown in Fig. 1 and were chosen on the basis of freshness and geographical location. The samples were crushed, washed in deionized water and sieved to obtain a phlogopite size fraction between 0.15 and 0.25 mm. Mineral separates were hand-picked, washed in acetone, dried, wrapped in aluminium foil and stacked in an irradiation capsule with similar-aged samples and neutron flux monitors (Fish Canyon Tuff sanidine (FCT-SAN), apparent age = 28.02 Ma; Renne et al., 1998). An attempt was made to select the least altered, inclusion-free phlogopite grains. Sample DT-02-12-1-4 was irradiated on April 25-27, 2005 at the McMaster Nuclear Reactor in Hamilton, Ontario for 84 MWH, with a neutron flux of ~3 x 10^{13} neutrons/cm^2/s. Total fusion analyses (n=72) of 21 neutron flux monitor positions yielded errors of <0.5% in the J value. Samples DT-02-7-1-1, DM-05-3-2-3 and TOA-96-6-8-1 were irradiated at the same facility on November 14-16, 2006, for 90 MWH, with a neutron flux of ~ 6 x 10^{13} neutrons/cm^2/s. Analyses (n=44) of 20 neutron flux monitor positions produced errors of 0.5% in the J value.

The samples were analyzed by the ^{40}Ar-^{39}Ar laser fusion technique at the Noble Gas Laboratory, Pacific Centre for Isotopic and Geochemical Research, University of British Columbia, Vancouver, BC, Canada (Table 4). The mineral separates were step-heated at incrementally higher powers in the defocused

beam of a 10W CO_2 laser (New Wave Research MIR10) until fused. The gas evolved from each step was analyzed by a VG5400 mass spectrometer equipped with an ion-counting electron multiplier. All measurements were corrected for total system blank, mass spectrometer sensitivity, mass discrimination, radioactive decay during and subsequent to irradiation, as well as interfering Ar from atmospheric contamination and the irradiation of Ca, Cl and K (Isotope production ratios: $(^{40}Ar/^{39}Ar)K=0.0302\pm0.00006$, $(^{37}Ar/^{39}Ar)Ca=1416.4\pm0.5$, $(^{36}Ar/^{39}Ar)Ca=0.3952\pm0.0004$, $Ca/K=1.83\pm0.01(^{37}ArCa/^{39}ArK)$).

Xenolith Sample Preparation

The xenoliths were separated from the host lamprophyre, and subsequently abraded along the margins using a Dremel™ rotary grinder in an effort to remove any lamprophyre material remaining on the surface and as much of the marginal reaction rims as possible. The nodules were then separately crushed using a stainless steel piston apparatus. The rock powders were then sieved using silk screen mesh into three separate size fractions. Zircon crystals were then hand picked from 120-245 μm and 30-120 μm fractions, using carefully cleaned petri dishes filled with ethanol. Following separation, the zircon crystals were immersed in distilled water and processed in an ultrasonic bath for 60 minutes in order to remove any material coating the zircon surface. Extreme care was exercised during the crushing and picking stages to avoid any potential of cross-contamination. No effort was made to select grains on the basis of morphology, colour or magnetism. The zircon separates, along with fragments of 559.0±0.2 Ma zircon standard z6266 (Stern and Amelin, 2003) were mounted in

epoxy resin at the Geological Survey of Canada (GSC) Geochronology Laboratory, in Ottawa. The mount was very lightly polished due to the very small size of the zircon separates and coated in high-purity Au. The grain mount was then imaged in both back-scatter electron (BSE) and cathodoluminescence (CL) modes using the GSC's Cambridge Instruments S200 scanning electron microscope.

The remaining rock powders from xenoliths 9044, 9047 and 9048 were stored in glass vials and submitted for Nd isotope analysis at the University of Alberta Radiogenic Isotope Facility.

U-Pb Geochronology

Zircon grains were analyzed at the J.C. Roddick Ion Microprobe Laboratory in Ottawa, using the second generation sensitive high resolution ion microprobe (SHRIMP II). U-Pb age determinations on ~9 × 12 um diameter spots were performed following standard operating procedures (Stern, 1997). Analyses were run at 22 minutes each, during which time 7 scans were performed. The calibration, correcting for the instrumental bias in the measured Pb/U ratios was was performed by multiple repeat measurements of $^{206}Pb^{+}/^{238}U^{+}$ and $^{254}[UO]^{+}/^{238}U^{+}$ of the 559.0±0.2 Ma z6266 zircon standard (Stern and Amelin, 2003). Within-session errors were evaluated by analyzing the standard every fourth or fifth analysis. Errors assigned to SHRIMP U-Pb ages were determined by numerical propagation of all known sources of error as outlined by Stern (1997). Overall, 61 analyses from 49 zircon grains were obtained during a single analytical session totalling ~40 hrs. The choice of spot locations was based on

zircon quality and relative absence of inclusions, textural relationships that were identified using cathodoluminescence (CL) imagery and the requirement that analytical spots be located within a single domain. Complete zircon U-Pb data are presented in Table 6, and concordia plots are shown in Fig. 5. CL photomicrographs of selected zircon grains are shown in Fig. 6. All errors reported in this and the following sections are given at the 95% confidence level.

Appendix 3: Geochemical Modelling

This appendix outlines the models used in interpretation of the geochemical character of the Quartet Mountain lamprophyres.

Hypothesis 1: The Quartet Mountain lamprophyres were derived by partial melting of a LREE enriched source mantle.

A model utilizing the concentrations of La and Yb as a function of degree of batch partial melting of both spinel and garnet peridotite was constructed to test the above hypotheses. The trace element composition of the model mantle sources was assumed to be equal to that of the primitive mantle composition (Sun and McDonough, 1985). The spinel and garnet peridotites were assumed to be composed of 80% olivine, 10% opx, 5% cpx, and 5% spinel or 5% garnet, respectively. The Nerst partition coefficients (Kd) used were as follows:

	olivine	***opx***	***cpx***	***spinel***	***garnet***
La	0.01	0.01	0.05	0.01	0.1
Yb	0.05	0.02	0.5	0.01	5

The bulk partition coefficient (D), for a given element, is defined as:

$$D = \sum_{i=1}^{n} x_i Kd_i ,$$

where x_i and Kd_i are the fraction of mineral i in a rock and the Nerst partition coefficient for the given element in mineral i. The bulk distribution coefficients calculated for spinel and garnet peridotite were: D_{La} = 0.012 and D_{Yb}=0.0675, and D_{La} = 0.0165 and D_{Yb}=0.317, respectively.

The concentration of La in Yb in melt as a function of the degree of batch partial melting of the two mantle sources is then calculated using:

$$C_L = \frac{C_0}{D + F(1-D)},$$

where C_L is the concentration of element i in the melt, C_0 is the initial concentration of element i in the unmelted source and F is the weight fraction of melt produced. At the inferred, very low, degree of partial melting, batch partial melting is likely to accurately reflect the melting conditions.

Figure A3 demonstrates that, even at very small degrees of melting (F<0.01) the concentrations of LREE observed in QML are up to 5 times greater than predicted by the melting of the primitive mantle source (Sun and McDonough, 1989). It thus appears that the source mantle had been enriched in LREE prior to the Early Cambrian generation of the Quartet Mountain lamprophyres. Comparison of the spinel and garnet peridotite models demonstrates that the garnet peridotite model is more consistent with the low measured Yb concentrations and elevated La/Yb ratios that characterize the QML.

Hypothesis 2: The Quartet Mountain lamprophyres were derived by partial melting of a mantle in which phlogopite or amphibole was left as a residual phase.

The relatively depleted primitive mantle-normalized LILE concentrations relative to the HFSE, coupled with the pronounced negative K anomalies hint at buffering of these elements during partial melting by a residual phase such as

phlogopite or amphibole. Involvement of these minerals in generation of a rock suite could be tested by plotting the concentrations of K against elements that behave incompatibly during melting involving these phases. Involvement of residual K-bearing phases during magma genesis will require that bulk partition coefficient for K (D_K) exceeds that of other incompatible elements and will thus produce a negative slope on a bivariate element diagram.

Figure A2 is a plot of K vs La, which behaves incompatibly in both phlogopite and amphibole. The positive correlation between K and La does not support the involvement of a K-bearing residual phase in the source. Instead, the relative LILE depletions and signature K-anomalies may reflect a relatively LILE depleted source.

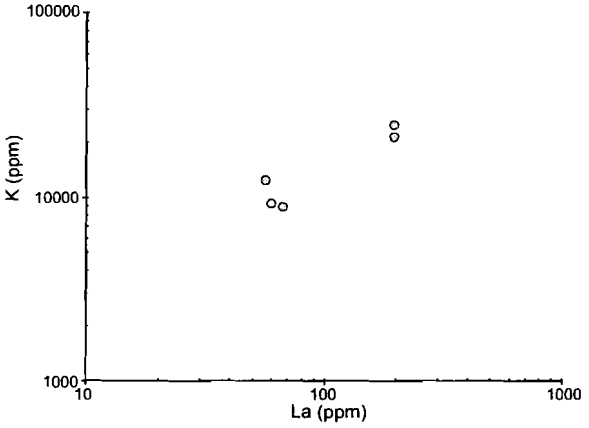

Figure A2. Log K (ppm) vs Log La (ppm) for the Quartet Mountain lamprophyres. The positive correlation between K and La argues against involvement of a K-bearing residual phase.

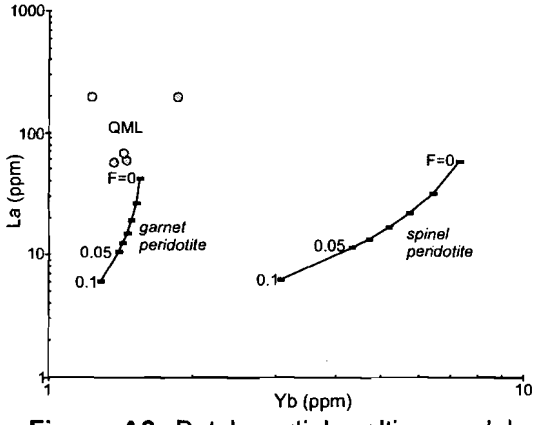

Figure A3. Batch partial melting model. The two lines represent modeled melt compositions from a garnet and a spinel peridotite, having primitive mantle trace element compositions (Sun and McDonough, 1989), as a function of fraction of melt produced (F).

Appendix 4: Overview of Equations for Nd Isotopic Compositions

Xenoliths 9044, 9047 and 9048, in addition to lamprophyre samples 2 and 6 were analyzed for Nd isotopic compositions at the Radiogenic Isotope Facility at the University of Alberta, in November of 2006. A number of values were derived from the measured data (Table 3) and this appendix lists the equations used in these derivations. Listed below are some important variables and constants used.

$\frac{^{143}Nd}{^{144}Nd}$	Measured isotopic ratio	atomic	As measured
Sm	Measured concentration	ppm	As measured
Nd	Measured concentration	ppm	As measured
at. wt. Sm	Atomic weight of Sm	g/mol	150.3656
at. wt. Nd	Atomic weight of Nd	g/mol	144.2399
^{147}Sm	Fractional abundance of ^{147}Sm relative to total Sm	atomic	0.149957
^{144}Nd	Fractional abundance of ^{144}Nd relative to total Nd	atomic	As defined below
λ	Decay constant for alpha decay of ^{147}Sm to ^{144}Nd	y^{-1}	6.54×10^{-12}

The subscript "t" denotes a value that has been recalculated to a time in the past, expressed in billions of years (Ga). The calculation of the present day $\frac{^{147}Sm}{^{144}Nd}$ from measured $\frac{^{143}Nd}{^{144}Nd}$ and Sm and Nd concentrations is as follows:

$$\frac{^{147}Sm}{^{144}Nd} = \left[\frac{Sm \times {}^{147}Sm}{at.wt.Sm}\right] \Big/ \left[\frac{Nd \times {}^{144}Nd}{at.wt.Nd}\right],$$

where

$$^{144}Nd = \frac{1}{\left(3.69014 + \frac{^{143}Nd}{^{144}Nd}\right)}.$$

The Sm-Nd isotopic evolution of a closed system through time is given by:

$$\frac{^{143}Nd}{^{144}Nd} = \frac{^{143}Nd}{^{144}Nd_0} + \frac{^{147}Sm}{^{144}Nd}\left(e^{(\lambda t)} - 1\right),$$

where subscript "0" denotes the initial $\frac{^{143}Nd}{^{144}Nd}$ at the time of system's closure.

Similarly, the isotopic evolution of the bulk earth is expressed as:

$$\frac{^{143}Nd}{^{144}Nd_{CHUR}} = \frac{^{143}Nd}{^{144}Nd_{0,CHUR}} + \frac{^{147}Sm}{^{144}Nd_{CHUR}}\left(e^{(\lambda t)} - 1\right),$$

where the subscript CHUR stands for "chondritic uniform reservoir" and denotes the values for the bulk earth, which have present day values of $\frac{^{143}Nd}{^{144}Nd_{CHUR}} = 0.512638$ and $\frac{^{147}Sm}{^{144}Nd_{CHUR}} = 0.1966$ (Jacobsen and Wasserburg, 1980). The above equation assumes that the *Sm/Nd* and initial $\frac{^{143}Nd}{^{144}Nd}$ of the earth

were identical to the *Sm/Nd* and $\frac{^{143}Nd}{^{144}Nd}$ ratios of chondritic meteorite parent bodies formed 4.55 Ga ago. Knowing the evolution of the bulk earth's $\frac{^{143}Nd}{^{144}Nd}$ through time is highly useful from both a geochronological and a geochemical standpoint. Additionally, this concept provides us with a useful notation for Nd isotope ratios that compares the relative deviation of $\frac{^{143}Nd}{^{144}Nd}$ of any rock to that of the bulk earth. The epsilon (ε) notation is defined as:

$$\varepsilon_{t,Nd} = \left[\left(\frac{\frac{^{143}Nd}{^{144}Nd}_{t}}{\frac{^{143}Nd}{^{144}Nd}_{t,CHUR}} \right) - 1 \right] \times 10^{4}.$$

The "depleted mantle" (DM) is a hypothetical upper mantle reservoir that was depleted in the more incompatible Nd relative to Sm through extraction of a partial melt in a previous episode, and has thus evolved along a more radiogenic trajectory than the bulk earth. The isotopic history of the "depleted mantle" is most commonly formulated according to the models of DePaolo (1981) and Goldstein et al. (1984). These models are based on compilations of the $\frac{^{143}Nd}{^{144}Nd_{t}}$ in ancient rocks that are presumed to have simple histories following their extraction from the mantle. The formulation of Goldstein et al. (1984) assumes linear evolution of $\frac{^{143}Nd}{^{144}Nd_{DM}}$ from $\varepsilon_{Nd} = 0$, at 4.5 Ga to present day $\frac{^{143}Nd}{^{144}Nd_{DM}}$ ratio of

0.513163, with the accompanying $\frac{^{147}Sm}{^{144}Nd}_{DM} = 0.2137$. The time evolution of $\frac{^{143}Nd}{^{144}Nd}_{DM}$ of Goldstein et al. (1984) may be expressed as:

$$\frac{^{143}Nd}{^{144}Nd}_{DM} = -\left[\frac{6.4}{4.5\times10^{12}}\right]t + 0.513163.$$

Assuming that throughout its history a rock has had the same or similar *Sm/Nd* as a mantle reservoir (usually CHUR or the depleted mantle), a model age estimating the time of extraction of that rock from the reservoir can be calculated. The model age thus represents the intersection of a sample's neodymium evolution curve with the evolution curve of a mantle reservoir in $\frac{^{143}Nd}{^{144}Nd}$ vs. time space. This calculated age provides a first-order constraint on the crustal residence time of a rock found in the earth's crust, although the uncertainty associated with this calculation is typically large.

The Quartet Mountain Lamprophyres are interpreted as low degree partial melts of the upper mantle, and were thus likely extracted from a reservoir geochemically similar to the "depleted mantle", rather than a reservoir having Nd isotope systematics akin to the bulk earth. The model depleted mantle age of a sample is calculated by combining the equations expressing the isotopic evolution of the sample and the depleted mantle. Using the depleted mantle model of Goldstein et al. (1984), the following relationship is derived:

$$\frac{^{143}Nd}{^{144}Nd} - \frac{^{147}Sm}{^{144}Nd}\left(e^{(\lambda t)} - 1\right) = \frac{^{143}Nd}{^{144}Nd_{DM}} - \frac{^{147}Sm}{^{144}Nd_{DM}}\left(e^{(\lambda t)} - 1\right).$$

Rearranging,

$$e^{\lambda t} = \frac{\frac{^{143}Nd}{^{144}Nd} - \left(\frac{^{143}Nd}{^{144}Nd}\right)_{DM}}{\frac{^{147}Sm}{^{144}Nd} - \left(\frac{^{147}Sm}{^{144}Nd}\right)_{DM}} + 1.$$

Solving for t,

$$t = \frac{1}{\lambda}\ln\left[\frac{\frac{^{143}Nd}{^{144}Nd} - \left(\frac{^{143}Nd}{^{144}Nd}\right)_{DM}}{\frac{^{147}Sm}{^{144}Nd} - \left(\frac{^{147}Sm}{^{144}Nd}\right)_{DM}} + 1\right] = \tau_{DM}.$$

Substituting in the known depleted mantle values yields:

$$\tau_{DM} = \frac{1}{\lambda}\ln\left[\frac{\frac{^{143}Nd}{^{144}Nd} - 0.513163}{\frac{^{147}Sm}{^{144}Nd} - 0.2137} + 1\right].$$

The model age assuming derivation from CHUR is expressed as follows:

$$\tau_{CHUR} = \frac{1}{\lambda}\left[\frac{\frac{^{143}Nd}{^{144}Nd} - 0.512638}{\frac{^{147}Sm}{^{144}Nd} - 0.1966} + 1\right]$$

and is also referred to as the "crustal residence" model age. The "crustal residence" model ages give younger estimates of the time of extraction than do "depleted mantle" model ages.

Appendix 5: Simple Binary Mixing Model for the Sm-Nd Isotope Geochemistry of Xenolith 9047

This appendix outlines the steps used in the calculation of the degree of contamination of the Wernecke Supergroup protolith by the lamprophyre magma that is required to produce the Nd isotopic composition of xenolith 9047. The basic premise of the model is that xenolith 9047 was originally a part of the Wernecke Supergroup. Furthermore, it is assumed that the xenolith's Sm-Nd isotopic systematics were comparable to those of the Wernecke Supergroup (Thorkelson et al., 2005) prior to its entrainment by lamprophyre sample 2. Thus, the model treats the range of available Sm-Nd analyses of the Wernecke Supergroup as one end-member composition, and a single Sm-Nd analysis of sample 2 as the other end-member composition. The model calculation was performed using present day $^{143}Nd/^{144}Nd$ ratios as well as $^{143}Nd/^{144}Nd$ ratios calculated for t = 530 Ma. Furthermore, the model calculations were performed using both measured Sm and Nd concentrations.

The concentration of any element X in a mixture, produced by the mixing of two end-member components in differing proportions which are specified by the parameter f defined as:

$$f = \frac{A}{A+B}$$

may be expressed as:

$$X_M = X_A f + X_B(1-f).$$

A and B are the weights of the two components in a given mixture, and X_A and X_B are the concentrations of element X in components A and B, respectively. In this model, A and B are used to denote the lamprophyre magma and Wernecke Supergroup end-members, respectively.

Mixing of two components, having not only different concentrations of Nd but also different $\frac{^{143}Nd}{^{144}Nd}$ can be expressed as:

$$\left(\frac{^{143}Nd}{^{144}Nd}\right)_M = \frac{Nd_A\left[\left(\frac{^{143}Nd}{^{144}Nd}\right)_B - \left(\frac{^{143}Nd}{^{144}Nd}\right)_A\right]}{Nd_M\left(Nd_A - Nd_B\right)} + \frac{Nd_A\left(\frac{^{143}Nd}{^{144}Nd}\right)_A - Nd_B\left(\frac{^{143}Nd}{^{144}Nd}\right)_B}{Nd_A - Nd_B}.$$

This equation is a hyperbola of the form:

$$\left(\frac{^{143}Nd}{^{144}Nd}\right)_M = \frac{a}{Nd_M} + b,$$

where a and b are constants, specified by the concentrations and $\frac{^{143}Nd}{^{144}Nd}$ ratios of neodymium that were measured in the lamprophyre and Wernecke Supergroup components. Recall that Nd_M, and thus $\frac{^{143}Nd}{^{144}Nd}$, are functions of the mixing parameter f.

Binary mixing hyperbolas can thus be plotted for $\left(\frac{^{143}Nd}{^{144}Nd}\right)_M$ vs. Nd_M and $\left(\frac{^{143}Nd}{^{144}Nd}\right)_M$ vs. Sm_M, where $\left(\frac{^{143}Nd}{^{144}Nd}\right)_M$, Nd_M and Sm_M at f values of 0 and 1 correspond to the compositions of the Wernecke Supergroup and lamprophyre

end-members, respectively. Figure A4 demonstrates that the neodymium isotopic signature of xenolith 9047 may be produced by mixing a Wernecke Supergroup protolith with approximately 10 weight % of lamprophyre melt, similar in composition to sample 2.

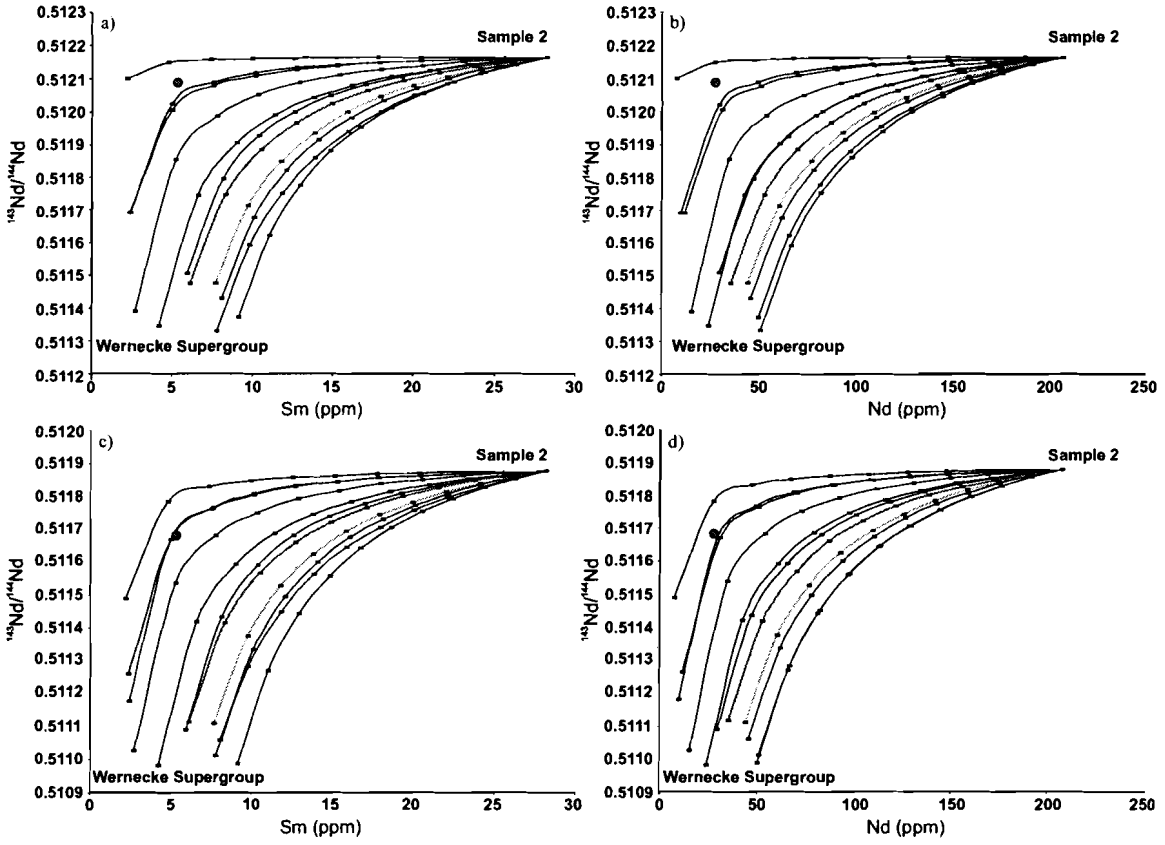

Figure A4. Calculated mixing curves reflecting mixing between xenolith-rich sample 2, and nine Wernecke Supergroup samples (Thorkelson, 2005). Each tick mark represents a 10% mixing increment (f = 0.1). Shaded circle represents the geochemical and isotopical composition of xenolith 9047. Light and dark grey curves represent modelled mixing between the lamprophyre and xenoliths 9048 and 9044, respectively. a) and b) $^{143}Nd/^{144}Nd$ vs. Sm and $^{143}Nd/^{144}Nd$ vs. Nd using present day isotopic ratios. c) and d) $^{143}Nd/^{144}Nd$ vs. Sm and $^{143}Nd/^{144}Nd$ vs. Nd using ratios calculated for t = 530 Ma.

Appendix 6: Overview of Equations Used for U-Pb Isotopic Dating of Zircon

Small, complexly zoned from xenoliths 9044, 9046, 9047, 9048 and 9049 were analyzed for U-Pb isotopic compositions at the J.C. Roddick Ion Microprobe Laboratory in Ottawa, in July, 2007 using the second generation sensitive high resolution ion microprobe (SHRIMP II). A detailed overview of the analytical techniques of zircon U-Pb age determinations using SHRIMP is provided by Stern (1997). The data was processed using the data reduction program "SQUID" (Ludwig, 2001a). The analytical results were interpreted using ISOPLOT (Ludwig, 2001b). This appendix reviews the main concepts of U-Pb zircon geochronology and lists the important constants, isotopic ratios and equations used in calculation of U-Pb ages of analyzed zircon domains.

There are four naturally occurring isotopes of Pb, the non-radiogenic ^{204}Pb and ^{206}Pb, ^{207}Pb and ^{208}Pb, which are the respective end-products of radioactive decay of ^{238}U, ^{235}U and ^{232}Th. The U-Pb method of dating is unique and appealing as it is based on the decay of two parent U isotopes to two daughter Pb isotopes. This allows for calculation of two ages, and serves as an internal test for the closure of the sample to the exchange of U or Pb. Importantly, the method allows for dating of disturbance events, provided that they have not led to the complete loss of radiogenic lead species. An additional age, based on the assumption that any disturbance resulting in effective Pb loss is recent, may be calculated from the measured radiogenic $\frac{^{207}Pb}{^{206}Pb}$ ratio.

$\frac{^{206}Pb^*}{^{238}U}$	Common-Pb corrected isotopic ratio	atomic	Measured[1]
$\frac{^{207}Pb^*}{^{235}U}$	Common-Pb corrected isotopic ratio	atomic	Measured[1,2]
$\frac{^{207}Pb^*}{^{206}Pb}$	Common-Pb corrected isotopic ratio	atomic	Measured[1]
$\frac{^{206}Pb}{^{238}U}age$	Calculated age	a	As defined below
$\frac{^{207}Pb}{^{235}U}age$	Calculated age	a	As defined below
$\frac{^{207}Pb}{^{206}Pb}age$	Calculated age	a	As defined below
λ_{238}	Decay constant for decay of ^{238}U to ^{206}Pb, assuming a closed system and secular equilibrium	y-1	1.55125×10^{-10}
λ_{235}	Decay constant for decay of ^{238}U to ^{206}Pb, assuming a closed system and secular equilibrium	y^{-1}	9.8485×10^{-10}
$\frac{^{238}U}{^{235}U}$	Present day $\frac{^{238}U}{^{235}U}$	atomic	137.88

[1] A complicated data reduction procedure that is beyond the scope of this thesis is performed using "SQUID" (Ludwig, 2001).

[2] The ^{235}U is calculated from the measured ^{238}U and the assumed present day $\frac{^{238}U}{^{235}U}$.

Direct measurement of the low-abundance ^{235}U isotopic species is highly impractical, due to the combination of low U concentrations (100 to 1000's of ppm) in zircon, low secondary ion yield generated by the bombardment of the zircon by the O_2^- primary ion beam, and the complex correction procedure for different relative ionization yields of U and Pb isotopic species. Instead, the ^{235}U abundance is calculated using the measured ^{238}U abundance and the well accepted $\frac{^{238}U}{^{235}U}$ value of 137.88.

$\frac{^{206}Pb^*}{^{238}U}$, $\frac{^{207}Pb^*}{^{235}U}$ and $\frac{^{207}Pb^*}{^{206}Pb}$ denote radiogenic ratios corrected for common (non-radiogenic) Pb. Non-radiogenic Pb may have two sources: the contaminant Pb contained within the gold coating and the initial common Pb that is incorporated in the zircon crystal lattice. The measured non-radiogenic Pb arising from the gold coating is corrected using the Pb composition measured independently by TIMS. Because Pb is highly incompatible in zircon, this correction is typically very small relative to the amount of radiogenic lead that is produced by the decay of the U and Th, and was thus not performed.

From the known $\frac{^{206}Pb^*}{^{238}U}$ and $\frac{^{207}Pb^*}{^{235}U}$ two separate ages may be calculated using the following relationships:

$$\frac{^{206}Pb^*}{^{238}U} = e^{\lambda_{238}t} - 1$$

and

$$\frac{^{207}Pb^{*}}{^{235}U} = e^{\lambda_{235}t} - 1$$

Simultaneously solving these equations for different values of time, t generates a curve in $\frac{^{206}Pb^{*}}{^{238}U}$ vs. $\frac{^{207}Pb^{*}}{^{235}U}$ space that describes the time-dependant evolution of $\frac{^{206}Pb^{*}}{^{238}U}$ and $\frac{^{207}Pb^{*}}{^{235}U}$, assuming closed system behaviour. This curve, is the locus of concordant $\frac{^{206}Pb^{*}}{^{238}U}$ and $\frac{^{207}Pb^{*}}{^{235}U}$ ratios and is referred to as the concordia curve. Considering the uncertainties in the decay rates of ^{238}U and ^{235}U ($\pm\lambda_{238}$ = 0.107%, $\pm\lambda_{235}$ = 0.126% at 2σ) shifts the position of the concordia curve in the $\left[\frac{^{207}Pb^{*}}{^{235}U}, \frac{^{206}Pb^{*}}{^{238}U}\right]$ space, thus producing a range of concordant values within the defined uncertainty limits. This range of concordant values hence defines a concordia "field", rather than a single concordia line that is defined by unique $\left[\frac{^{207}Pb^{*}}{^{235}U}, \frac{^{206}Pb^{*}}{^{238}U}\right]$ pairs. Isotopic system disturbances, typically lead to an effective loss of Pb, and consequent discordance in the $\frac{^{206}Pb^{*}}{^{238}U}$ and $\frac{^{207}Pb^{*}}{^{235}U}$ ratios. Given a sufficient number of discordant analyses affected by the same disturbance event, the timing of the disturbance can frequently be established.

From the determination of the $\frac{^{207}Pb^{*}}{^{206}Pb}$ ratio, the $\frac{^{207}Pb}{^{206}Pb}$ age can be calculated using the following relation:

$$\frac{\frac{^{207}Pb^{*}}{^{235}U}}{\frac{^{206}Pb^{*}}{^{238}U}} = \frac{e^{\lambda_{235}t} - 1}{e^{\lambda_{238}t} - 1}$$

Rearranging:

$$\frac{^{207}Pb^{*}}{^{206}Pb} = \frac{^{235}U}{^{238}U}\left(\frac{e^{\lambda_{235}t} - 1}{e^{\lambda_{238}t} - 1}\right)$$

And substituting,

$$\frac{^{207}Pb^{*}}{^{206}Pb} = \frac{1}{137.88}\left(\frac{e^{\lambda_{235}t} - 1}{e^{\lambda_{238}t} - 1}\right)$$

yields a transcendental equation that can not be solved for t by algebraic methods, but is easily solved on a computer by performing a series of successive approximations of t until a satisfactory solution is found.

The $\frac{^{207}Pb}{^{206}Pb}$ age, is generally not used for young samples (<1.5 Ga), which are low in radiogenic ^{207}Pb contents, and hence have large associated uncertainties. Such samples are better characterized using the $\frac{^{206}Pb}{^{238}U}$ ages, which are calculated from significantly more abundant ^{206}Pb and ^{238}U and are hence

more precise. Conversely, ages of samples older than approximately 1.5 Ga are typically better expressed using the $\frac{^{207}Pb}{^{206}Pb}$ ages.

Appendix 7: Scanning electron images of the analyzed zircon grains and supplementary zircon data

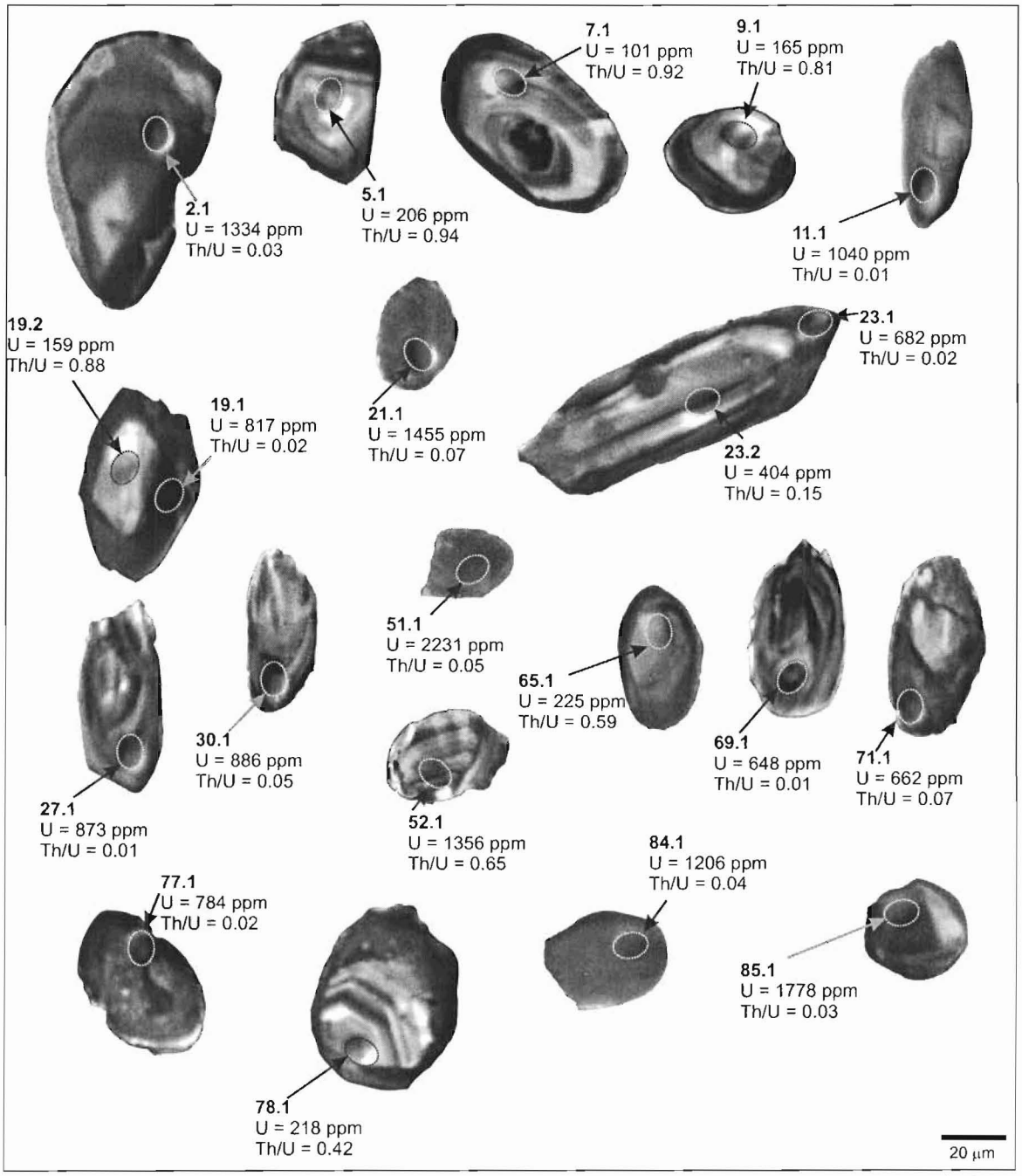

Figure A5. Cathodoluminescence photomicrographs of SHRIMP analyzed zircon crystals from xenolith 9044. Analysis spot identification numbers, locations, measured U concentrations and Th/U ratios are shown for each zircon in this figure and figures A6-A9.

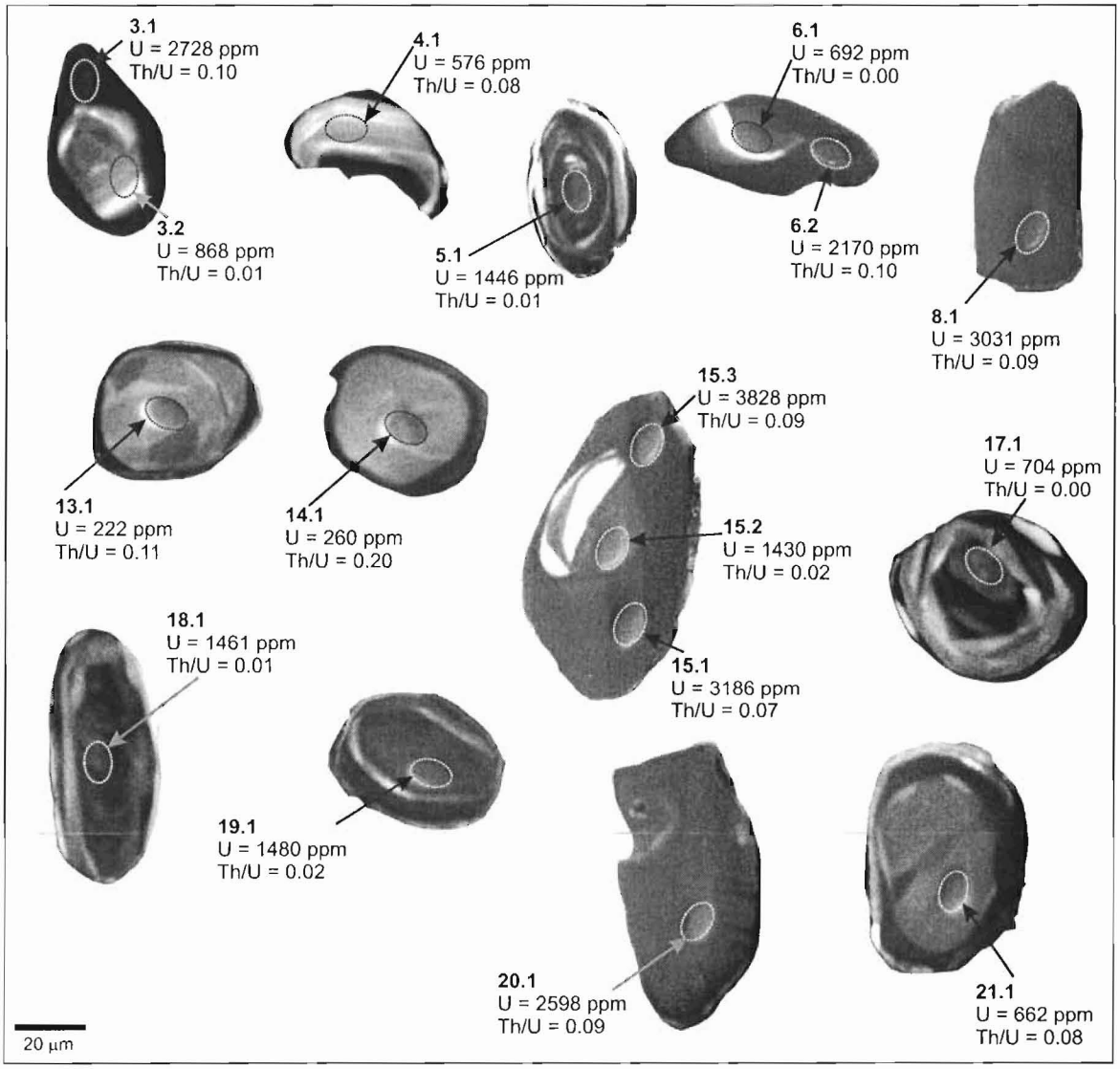

Figure A6. Cathodoluminescence photomicrographs of SHRIMP analyzed zircon grains from xenolith 9046.

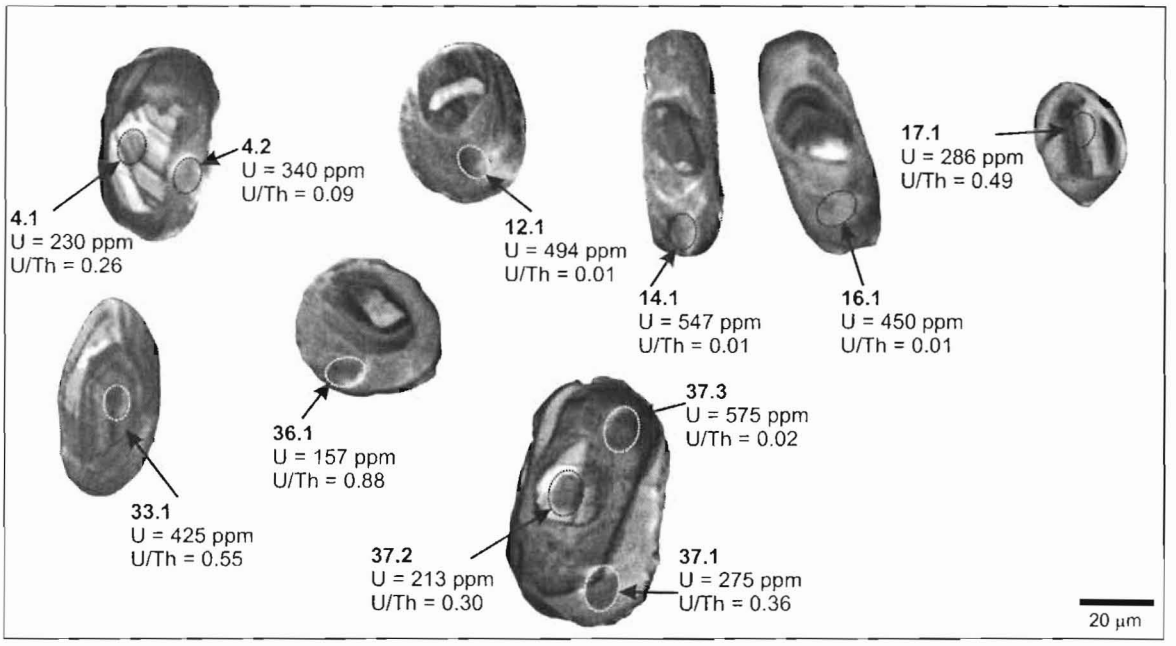

Figure A7. Cathodoluminescence photomicrographs of SHRIMP analyzed zircon grains from xenolith 9047.

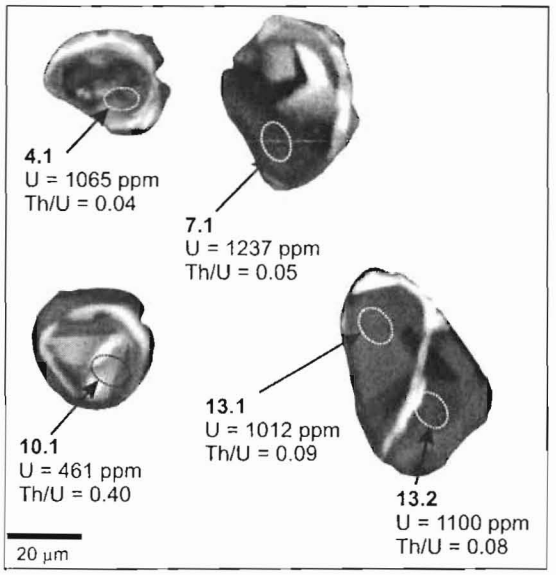

Figure A8.
Cathodoluminescence photomicrographs of SHRIMP analyzed zircon grains from xenolith 9048.

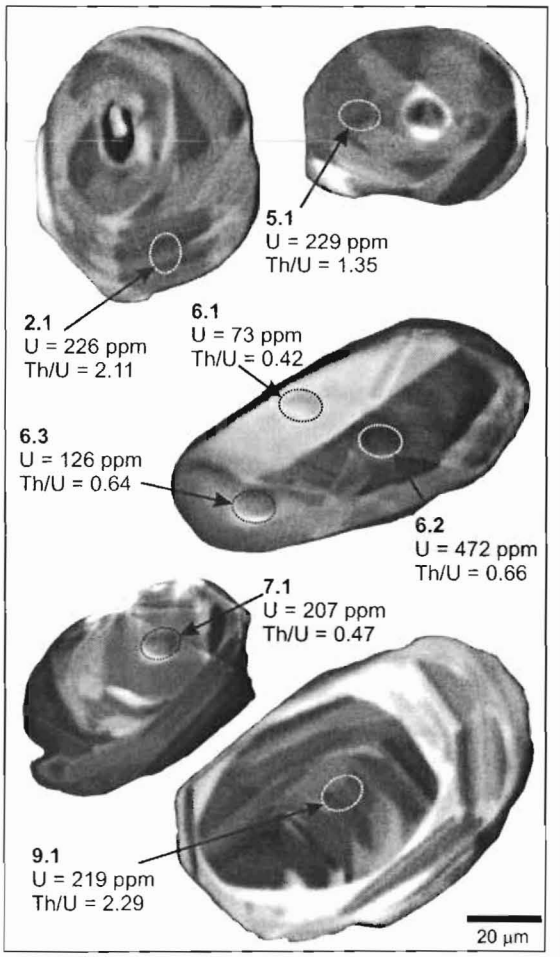

Figure A9. (right). Cathodoluminescence photomicrographs of SHRIMP analyzed zircon grains from xenolith 9049.

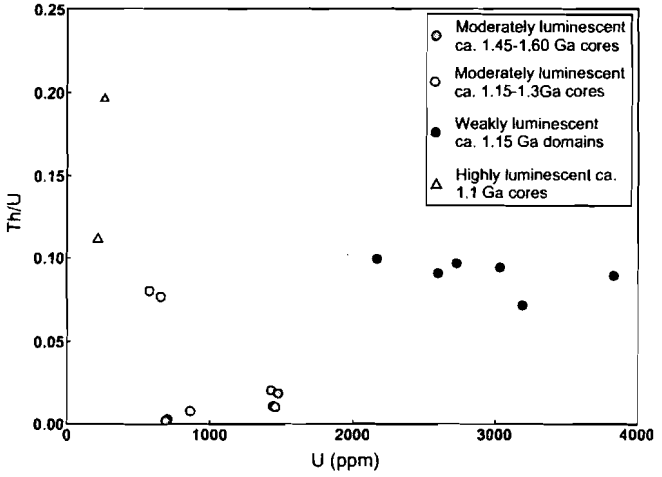

Figure A10. Th/U vs. U(ppm) diagram showing the chemical composition of different zircon domains from xenolith 9046. The weakly luminescent, unzoned grains and rims are characterized by very high U concentrations (>2000 ppm) and uniform Th/U ratios (0.07-0.10). The moderately luminescent cores that plot in the continuous array along the concordia between ca. 1.45 Ga and 1.60 Ga show remarkably similar chemistry, with the exception of analysis 6.1 (see text). The moderately luminescent cores that plot along the concordia between ca. 1.15 and 1.30 Ga, show a much greater variation in their chemistry, with the "youngest" cores being depleted in U and showing elevated Th/U relative to the "older"cores. This trend may reflect a correlation between the degree of recrystallization and effective loss of U and radiogenic Pb. The highly luminescent cores may represent the completely recrystallized end-members of this hypothetical series.

Table A1. Summary of U-Pb age-calculations and associated statistical parameters

Xenolith	Age Significance	Method	Analyses Used	Calculated Age and Error	MSWD[†]	POF[‡]
9044	Metamorphic zircon growth and radiogenic Pb loss during lamprophyre emplacement	U-Pb discordia linc regression	11.1, 19.1, 21.1, 23.1 27.1, 30.1, 51.1 69.1, 17.1, 77.1	1246 ± 29 Ma 503 ± 79 Ma	1.4	0.19
9046	Metamorphic zircon growth	weighted mean $^{206}Pb/^{238}U$ age	3.1, 6.2, 8.1 15.1, 15.3, 20.1	1184 ± 15 Ma	1.4	0.23
	Best estimate of metamorphism using metamorphic zircon, and recrystallized cores	weighted mean $^{206}Pb/^{238}U$ age	3.1, 4.1, 6.2, 8.1 13.1, 14.1, 15.1 15.3, 20.1, 21.1	1168 ± 22 Ma	2.2	0.004
9047	Zircon recrystallization	Concordia age	12.1, 14.1, 16.1	1269 ± 20 Ma	3.5	0.061
	Metamorphic zircon growth	Concordia age	4.2, 36.1, 37.1	1149 ± 21 Ma	1.14	0.29
9048	Metamorphic zircon growth	Concordia age	7.1, 13.1	1149 ± 19 Ma	0.061	0.95
9049	Crystallization age of igneous protolith and post-emplacement recrystallization of zircon	weighted mean $^{206}Pb/^{238}U$ age	2.1, 6.1 6.2, 6.3, 7.1 9.1, 5.1	1146 ± 31 Ma	2.0	0.068

[†] MSWD - Mean Square of Weighted Deviates
[‡] POF - Probability of Fit

Appendix 8: Age and Nature of the Upper Amphibolite to Granulite Grade Crustal Xenoliths

The study of the Quartet Mountain Lamprophyre xenoliths was in large part driven by their upper amphibolite to granulite-facies metamorphic grade, which is significantly higher than the maximum regional greenschist metamorphism observed in the schist belts of the Fairchild Lake Group (FLG; Delaney, 1981; Thorkelson et al., 2005). The greenschist metamorphic grade of FLG was attained at peak temperatures of 450-550 °C (Brideau et al., 2002; Laughton et al., 2005) during the first deformational phase of Racklan orogeny, between 1.71 and 1.60 Ga (Thorkelson et al., 2005). In contrast, the sillimanite and potassium-feldspar bearing mineral assemblage of xenoliths 9044, 9047 and 9048 implies minimum metamorphic temperatures of ~600 °C (Spear and Cheney, 1989; Fig. A11). The base of the Fairchild Lake Group, the oldest non-crystalline rock unit in the Canadian Cordillera, is nowhere exposed and thus the nature of the substrate on which it lays is uncertain. The unexposed, underlying rock is presumed to be crystalline basement older than ca 1.84 Ga (Thorkelson et al., 2005), or an unidentified sedimentary succession, with the maximum age of ca. 1.84 Ga. Presently, this hypothesis cannot be examined geophysically, as no deep seismic data for the study area and much of the Yukon-Northwest Territories border are available, and the available aeromagnetic and gravity data do not offer insight into the subsurface stratigraphy. However, seismic and gravity surveys ~100 km north of the study area, in the Eagle Plains fold belt and the Richardson Mountains anticlinorium, are consistent with westward increasing

depth to the crystalline basement, deepening from ~10 km, underneath the Richardson Mountains anticlinorium, to ~28 km beneath the Eagle Plains fold belt (Hall and Cook, 1998). Approximately 25-30 km of supracrustal Proterozoic strata are interpreted to overlie the present day Yukon basement, based on the data from Lithoprobe Slave-Northern Cordillera Lithospheric Evolution (SNORCLE) line 3 transect, approximately 150 km to the southeast, in the Mackenzie Mountains of eastern Yukon (Cook et al., 2004). Characterization of the age, depth and thickness, and petrologic character of this underlying basement presents an important challenge in improving our understanding of the evolution of northwestern Laurentia.

The identified peraluminous mineral assemblage of garnet+sillimanite+K-feldspar+muscovite±quartz in xenoliths 9044, 9046 and 9047 is consistent with high-temperature metamorphism of a pelitic protolith. The identification of small, rounded zircon cores, characterized by variable chemistry and zoning patterns, using BSE and CL imagery further supports the meta-sedimentary origin of the high-grade xenoliths. Imprecise SHRIMP data from detrital zircon cores from xenolith 9044, suggest that the xenolith is older than ca. 1.71 Ga, but is likely younger than ca. 1.84 Ga. Imprecise analyses of 6 detrital cores from xenoliths 9047 and 9048 are consistent with this interpretation. The age of deposition of the xenolith protolith is bracketed by the ca. 1.71-1.84 Ga interval, and is thus indistinguishable from the age of the Wernecke Supergroup. Similarly, the neodymium isotopic systematics of xenoliths 9044 and 9048 are indistinguishable from those of the Wernecke Mountains (Thorkelson et al., 2005)

and fall within the range characteristic of the western Canadian Shield, and the terranes amalgamated during the ca. 1.95-1.84 Ga Wopmay Orogen (Bowring and Podosek, 1989; Villeneuve et al., 1991, 1993; Ross et al., 2001).

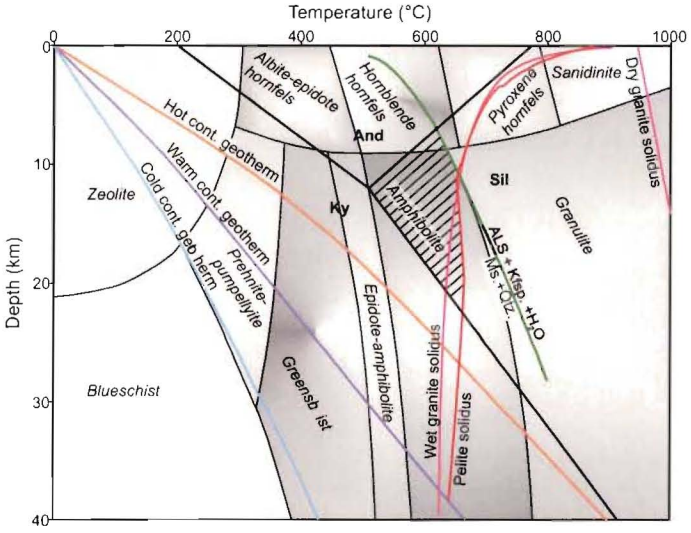

Figure A11. Depth-Temperature projection for the crustal lithosphere. The figure shows the relevant mineral stability fields, melting relationships and model geotherms. The aluminosilicate mineral stability fields (And: Andalusite; Ky: Kyanite; Sil: Sillimanite) are from Holdaway (1971); univariant curve representing reaction muscovite + quartz = K-feldspar + aluminosilicate + H_2O is from Spear and Cheney (1989); wet granite solidus curve is from Luth (1964) and Johannes (1984); dry granite solidus is from Johannes and Holtz (1996); pelite solidus is from White et al. (2001), model cold and warm continental geotherms are from Winter (2001), model hot continental geotherm is from Harder and Russell (2006). The observed retrograde metamorphic assemblage of Qtz + Sil + Kfs + Ms positions xenoliths 9044, 9047 and 9048 on the low-T side of the Ms+Qtz = Kfs + ALS + H_2O univariant, within the sillimanite stability and upper amphibolite facies fields (diagonally hatched field). The replacement relationship between muscovite and K-feldspar, however, indicates that xenoliths experienced granulite-grade peak metamorphic conditions at ~T = 600 °C. The figure also demonstrates an accepted hot crustal geothermal conditions cannot account for the inferred peak metamorphic conditions.

Appendix 9. Geologic Map of Australia displaying the known sources of ca. 1.60-1.49 Ga zircon.

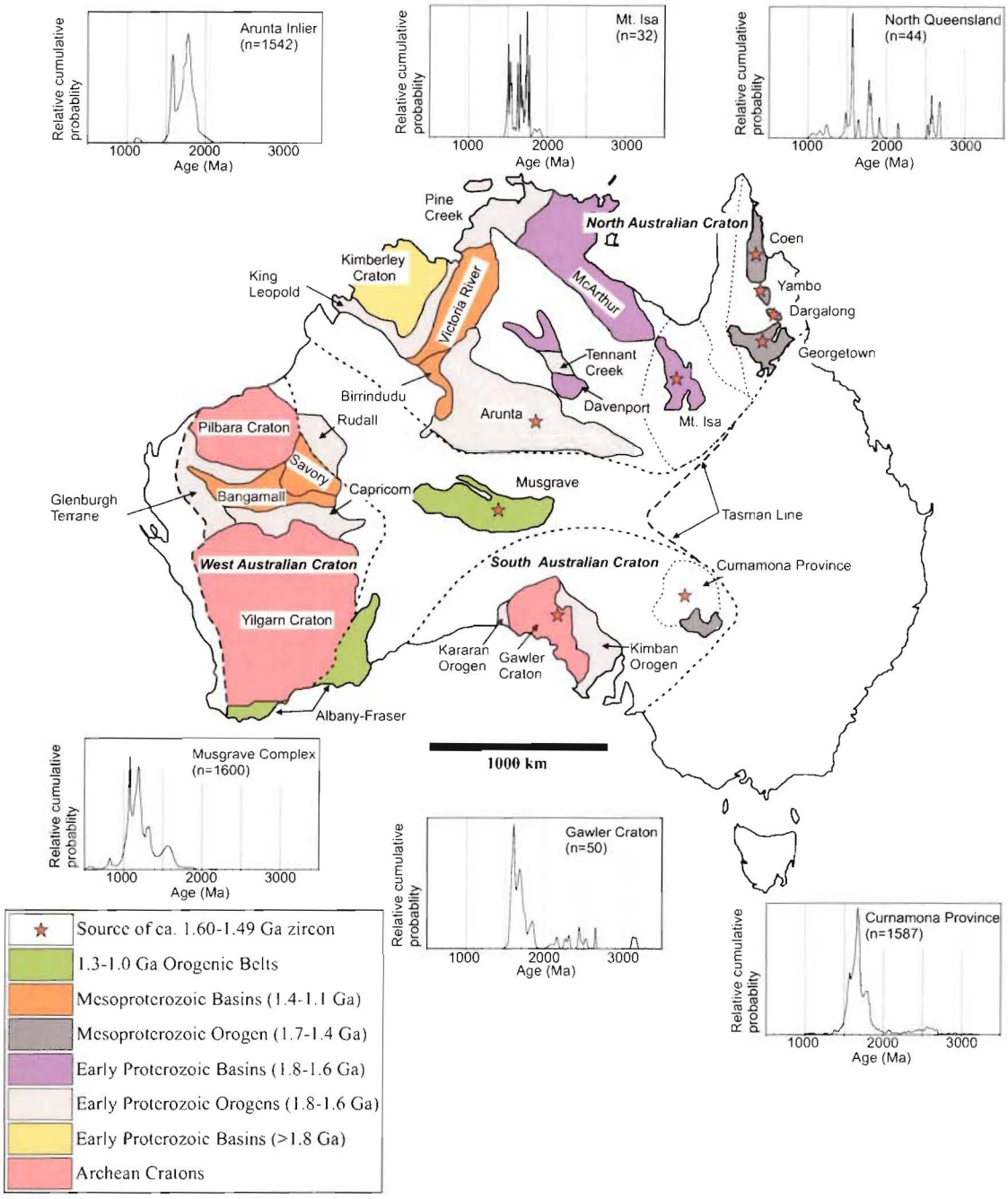

Figure A12. Map of Australia displaying the major Archean, Paleoproterozoic and Mesoproterozoic terranes, along with the known Australian sources of ca. 1.60-1.49 Ga zircon. Sources for geochronologic data used to construct the cumulative age probability plots are as follows: Gawler Craton - Ireland et al. (1998); Arunta Inlier - Camacho et al. (2002); North Queensland - Blewett et al. (1998); Mt. Isa - Connors and Page (1995) and Page and Sun (1998); Curnamona Province - Raetz et al. (2002); Musgrave Complex - Camacho et al. (2002). Map modified from Betts and Giles (2006) and Wade et al. (2006).

REFERENCE LIST

Abbott, J.G. 1997. Geology of the upper Hart River area, eastern Ogilvie Mountains, Yukon Territory (116A/10, 116A/11). Exploration and Geological Services Division, Yukon Region, Indian and Northern Affairs Canada, Bulletin 9, 76 p.

Ahäll, K., Connelly, J.N. and Brewer, T.S. 2000. Episodic rapakivi magmatism due to distal orogenesis? correlation of 1.69-1.50 Ga orogenic and inboard, "anorogenic" events in the Baltic Shield. Geology 28, 823-826.

Aitken, J.D. 1991. The Ice Brook Formation and post-Rapitan late Proterozoic glaciation, Mackenzie Mountains, Northwest Territories. Geological Survey of Canada, Bulletin 404, 43 p.

Aitken, J.D. and McMechan, M.E. 1992. Middle Proterozoic assemblages. *In:* H. Gabrielse and C.J. Yorath (Eds.), Geology of the Cordilleran Orogen in Canada. Geological Survey Canada, Geology of Canada, no.4, Chap. 5, pp.97-124.

Anderson, H.E. and Davis, D.W. 1995. U-Pb geochronology of the Moyie sills, Purcell Supergroup, southeastern British Columbia: implications for the Mesoproterozoic geological history of the Purcell (Belt) Basin, Canadian Journal of Earth Sciences 32, 1180-1193.

Anderson, H.E. and Parrish, R.R. 2000. Chapter 7. U-Pb geochronological evidence for the geological history of the Belt-Purcell Supergroup, southeastern British Columbia. *In:* J.W. Lydon, T. Höy, J.F. Slack and M.E. Knapp (Eds.), The Geolgical Environment of the Sullivan Deposit, British Columbia. Geological Association of Canada, Mineral Deposits Division, Special Publication No.1, pp. 113-126.

Bell, R.T. 1986. Megabreccias in northeastern Wernecke Mountains, Yukon Territory. *In:* Current Research, Part A. Geological Survey of Canada, Paper 1986-1A, pp. 375-384.

Bell, R.T. and Jefferson, C.W. 1987. An hypothesis for an Australian-Canadian connection in the late Proterozoic and the birth of the Pacific Ocean. *In:* Proceedings of Pacific Rim Congress 1987; Parkville, Victoria, Australia. The Australasian Institute of Mining and Metallurgy, Carlton, Victoria, Australia, pp. 39-50.

Bell, S., Condie, K.C. and Geraldes, M.C. 1999. Origin of arc-related granitoids from the SW Amazon Craton; juvenile crustal additions at 1550-1450 Ma. *In:* Abstracts with Programs, Geological Society of America 1999 Annual Meeting. Geological Society of America 31, 205.

Bettencourt, J.S., Tosdal, R.M., Leite, W.B. and Payolla, B.L. 1999. Mesoproterozoic rapakivi granites of the Rondonia tin province, southwestern border of the Amazonian Craton, Brazil - I. reconnaissance U-Pb geochronology and regional implications. Precambrian Research 95, 41-67.

Betts, P.G. and Giles, D. 2006. The 1800-1100 Ma tectonic evolution of Australia. Precambrian Research 144, 92-125.

Blewett, R.S., Black, L.P., Sun, S.S., Knutson, J., Hutton, L.J. and Bain, J.H.C. 1998. U-Pb zircon and Sm-Nd geochronology of the Mesoproterozoic of north Queensland: implications for a Rodinian connection with the Belt Supergroup of North America. Precambrian Research 89, 101-127.

Bowring, S.A. and Podosek, F.A. 1989. Nd isotopic evidence from Wopmay Orogen for 2.0-2.4 Ga crust in western North America. Earth and Planetary Science Letters 94, 217-230.

Bradley, D.C., Dumoulin, J., Layer, P. Sunderlin, D., Roeske, S., McClelland, B., Harris, A.G., Abbott, J.G., Bundtzen, T. and Kusky, T. 2003. Late Paleozoic orogeny in Alaska's Farewell terrane. Tectonophysics 372, 23-40.

Brideau, M.-A., Thorkelson, D.J., Godin, L. and Laughton, J.R. 2002. Paleoproterozoic deformation of the Racklan orogeny, Slats Creek (106/D/16) and Fairchild Lake (106C/13) map areas, Wernecke Mountains, Yukon. *In:* D.S. Emond, L.H. Weston, and L.L. Lewis (Eds.), Yukon Exploration and Geology 2001. Exploration and Geological Services Division, Yukon Region, Indian and Northern Affairs Canada, pp. 65-72.

Brookfield, M.E. 1993. Neoproterozoic Laurentia-Australia fit. Geology 21. 683-686.

Camacho, A., Hensen, B.J. and Armstrong, R. 2002. Isotopic test of a thermally driven intraplate orogenic model, Australia. Geology 30, 887-890.

Canil, D. 2004. Mildly incompatible elements in peridotites and the origins of mantle lithosphere. Lithos 77, 375-393.

Cecile, M.P. 1982. The lower Paleozoic Misty Creek Embayment, Selwyn Basin, Yukon and Northwest Territories. Geological Survey of Canada, Bulletin 335, 78 p.

Colpron, M., Logan, J.M. and Mortensen J.K. 2002. U-Pb zircon age constraint for late Neoproterozoic rifting and initiation of the lower Paleozoic passive margin of western Laurentia. Canadian Journal of Earth Sciences 39. 133-143.

Condie, K.C and Rosen, O.M. 1994 Laurentia-Siberia connection revisited. Geology 22, 168-170.

Connors, K.A. and Page, R.W. 1995. Relationships between magmatism, metamorphism and deformation in the western Mount Isa inlier, Australia. Precambrian Research 71, 131-153.

Cook, D.G. and MacLean, B.C. 2004. Subsurface Proterozoic stratigraphy and tectonics of the western plains of the Northwest Territories. Geological Survey of Canada. Bulletin 575, 91 p.

Cook, F.A., Clowes, R.M., Snyder, D.B., Van der Velden, A.J., Hall, K.W., Erdmer, P. and Evenchick, C.A. 2004. Precambrian crust beneath the Mesozoic northern Canadian Cordillera discovered by Lithopropbe seismic reflection profiling. Tectonics 23, TC201O, 28 p.

Corfu, F., Hanchar, J.M., Hoskin, P.W.O. and Kinny, P.D. 2003. Atlas of zircon textures. *In:* J.M. Hanchar and P.W.O. Hoskin (Eds.), Zircon. Mineralogical Society of America, Reviews in Mineralogy and Geochemistry 53, 469-500.

Creaser, R.A., Erdmer, P., Stevens, R.A. and Grant, S.J. 1997. Tectonic affinity of Nisutlin and Anvil assemblage strata from the Teslin tectonic zone, northern Canadian Cordillera: constraints from neodymium isotope and geochemical evidence. Tectonics 16, 107-121.

Dalziel, I.W.D. 1991. Pacific margins of Laurentia and East Antarctica-Australia as a conjugate rift pair: evidence and implications for an Eocambrian supercontinent. Geology 19, 598-601.

Davis, W.J. 1997. U-Pb zircon and rutile ages from granulite xenoliths in the Slave Province; evidence for mafic magmatism in the lower crust coincident with Proterozoic dike swarms, Geology 25, 343-346.

Davis, W.J., Canil, D., MacKenzie, J.M. and Carbno, G.B. 2003. Petrology and U-Pb geochronology of lower crustal xenoliths and the development of a craton, Slave Province, Canada. Lithos 71, 541-573.

Delaney, G.D. 1981. The mid-Proterozoic Wernecke Supergroup, Wernecke Mountains, Yukon Territory. *In:* F.H.A. Campbell (Ed.), Proterozoic basins of Canada. Geological Survey of Canada, Paper 81-10, pp. 1-23.

DePaolo, D.J. Neodymium isotopes in the Colorado Front Range and crust-mantle evolution in the Proterozoic. Nature 291, 193-196.

DePaolo, D.J. and Wasserburg, G.J. 1976. Nd isotopic variations and petrogenetic models. Geophysical Research Letters 3, 249-252.

Dodson, M.H. 1973. Closure temperature in cooling geochronological and petrological systems. Contributions to Mineralogy and Petrology 40, 259-274.

Doughty, P.T. and Chamberlain, K.R. 2004. New U-Pb SHRIMP evidence for multiple metamorphic events in the northern U.S. Cordillera; Eocene, Cretaceous, and late Precambrian (Grenville) events. *In:* Abstracts with Programs, Geological Society of America 2004 annual meeting. Geological Society of America 36, 271.

Dudas, F.Ö. and Lustwerk, R.L. 1997. Geochemistry of the Little Dal basalts: continental tholeiites from the Mackenzie Mountains, Northwest Territories, Canada. Canadian Journal of Earth Sciences 34, 50-58.

Eisbacher, G.H. 1978. Two major Proterozoic unconformities, northern Cordillera. *In:* Current research, part A. Geological Survey of Canada, Paper 78-1A, pp. 53-58.

Eisbacher, G.H. 1981. Sedimentary tectonics and glacial record in the Windermere Supergroup, Mackenzie Mountains, northwestern Canada. Geological Survey of Canada, Paper 80-27, 40 p.

Eisbacher, G.H. 1985. Late Proterozoic rifting, glacial sedimentation, and sedimentary cycles in the light of Windermere deposition, western Canada. Palaeogeography, Palaeoclimatology, Palaeoecology 51, 231-254.

Erdmer, P., Moore, J.M., Heaman, L., Thompson, R.I., Daughtry, K.L. and Creaser, R.A. 2002. Extending the ancient margin outboard in the Canadian Cordillera; record of Proterozoic crust and Paleocene regional metamorphism in the Nicola Horst, southern British Columbia, Canadian Journal of Earth Sciences 39, 1605-1623.

Ernst, R.E., Head, J.W., Parfitt, E., Grosfils, E. and Wilson, E. 1995. Giant radiating dyke swarms on Earth and Venus. Earth and Planetary Science Letters 39, 1-58.

Frost, B.R. Avchenko, O.V, Chamberlain, K.R. and Frost, C.D. 1998. Evidence for extensive Proterozoic remobilization of the Aldan Shield and implications for Proterozoic plate tectonic reconstructions of Siberia and Laurentia. Precambrian Research 89, 1-23.

Gabrielse, H., Blusson, S.L. and Roddick, J.A. 1973. Geology of Flat River, Glacier Lake, and Wrigley Lake map-areas, District of Mackenzie and Yukon Territory. Geological Survey of Canada, Memoir 366 (Parts I and II), 421 p.

Gehrels, G.E. and Ross, G.M. 1998. Detrital zircon geochronology of Neoproterozoic to Permian miogeoclinal strata in British Columbia and Alberta, Canadian Journal of Earth Sciences 35, 1380-1401.

Giles, D., Betts, P. and Lister, G. 2002. Far-field continental backarc setting for the 1.80-1.67 Ga basins of northeastern Australia, Geology 30, 823-826.

Gillerman, V.S., Jercinovic, M.J. and Stein, H.J. 2002. U-Pb and Re-Os geochronology suggest a multistage Precambrian-Mesozoic history for thorium and copper mineralization, Lemhi Pass, Idaho. *In:* Abstracts with Programs, Geological Society of America 2002 annual meeting, Geological Society of America 34, 337.

Godwin, C.I. and Price, B.J. 1986. Geology of the Mountain Diatreme kimberlite, north-central Mackenzie Mountains, district of Mackenzie, Northwest Territories. *In:* Mineral deposits of Northern Cordillera symposium, Whitehorse, Yukon, Vol. 37, pp. 298-310.

Goldstein, S.L., O'Nions, R.K. and Hamilton, P.J. 1984. A Sm-Nd isotopic study of atmospheric dusts and particulates from major river systems. Earth and Planetary Science Letters 70, 221-236.

Goodfellow, W.D., Cecile, M.P. and Leybourne, M.I. 1995. Geochemistry, petrogenesis, and tectonic setting of lower Paleozoic alkalic and potassic volcanic rocks, northern Canadian Cordilleran miogeocline. Canadian Journal of Earth Science 32, 1236-1254.

Gordey, S.P. and Anderson, R.G. 1993. Evolution of the northern Cordilleran miogeocline, Nahanni map area (105I), Yukon and Northwest Territories. Geological Survey of Canada, Memoir 428, 214 p.

Gordey, S.P. and Makepeace, A.J. (compilers). 2003. Yukon Digital Geology (version 2), Yukon Geological Survey, Open File 2003-9(D); also known as Geological Survey of Canada Open File 1749, 2 CD-ROMs.

Green, L.H. 1972. Geology of Nash Creek, Larsen Creek, and Dawson map-areas, Yukon Territory (106D, 116A, 116B and 116C (E1/2)), Operation Ogilvie, Geological Survey of Canada, Memoir 364, 157 p.

Greentree, M.R., Li, Z.X., Li, X.H. and Wu, H. 2006. Late Mesoproterozoic to earliest Neoproterozoic basin record of the Sibao orogenesis in western South China and relationship to the assembly of Rodinia. Precambrian Research 151, 79-100.

Hall, K.W. and Cook, F.A. 1998. Geophysical transect of the Eagle Plains fold belt and Richardson Mountains anticlinorium, northwest Canada. Geological Society of America Bulletin 110, 311-325.

Hamilton, R. and Rock, N.M.S. 1989. Geochemistry, mineralogy and petrology of a new find of ultramafic lamprophyres from Bulljah Pool, Nabberu Basin, Yilgarn Craton, western Australia. Lithos 24, 275-290.

Harder, M. and Russell, J.K. 2006. Thermal state of the upper mantle beneath the Northern Cordilleran Volcanic Province (NCVP), British Columbia, Canada. Lithos 87, 1-22.

Harlan, S.S., Heaman, L., LeCheminant, A.N. and Premo, W.R. 2003. Gunbarrel mafic magmatic event: A key 780 Ma time marker for Rodinia plate reconstructions. Geology 31, 1053-1056.

Heaman, L.M., LeCheminant, A.N. and Rainbird, R.H. 1992. Nature and timing of Franklin igneous events, Canada: Implications for a late Proterozoic mantle plume and the break-up of Laurentia. Earth and Planetary Science Letters 109, 117-131.

Helmstaedt, H.H., Mott, J.A., Hall, D.C., Schulze, D.J. and Dixon, J.M. 1988. Stratigraphic and structural setting of intrusive breccia diatremes in the White River-Bull River area, southeastern British Columbia. *In:* Geological Fieldwork 1987, British Columbia Ministry of Energy , Mines and Petroleum Resources, Paper 1988-1, pp. 363-368.

Hildebrand, R.S., Hoffman, P.F. and Bowring, S.A. 1987. Tectono-magmatic evolution of the 1.9-Ga Great Bear magmatic zone, Wopmay Orogen, northwestern Canada. Journal of Volcanology and Geothermal Research 32, 99-118.

Hildebrand, R.S. and Baragar, W.R.A. 1991. On folds and thrusts affecting the Coppermine River Group, northwestern Canadian Shield, Canadian Journal of Earth Sciences 28, 523-531.

Hoffman, P.F. 1980. Wopmay Orogen: a Wilson cycle of early Proterozoic age in the northwest of the Canadian Shield. Geological Survey of Canada, Special Paper 20, 523-549.

Hoffman, P.F. 1991. Did the breakout of Laurentia turn Gondwanaland inside-out? Science 252, 1409-1412.

Hoskin, P.W.O. and Schaltegger, U.. 2003. The composition of zircon and igneous and metamorphic petrogenesis. *In:* J.M. Hanchar and P.W.O. Hoskin (Eds.), Zircon. Mineralogical Society of America, Reviews in Mineralogy and Geochemistry 53, 27-62.

Howard, K.A. 1991. Intrusion of horizontal dikes; tectonic significance of middle Proterozoic diabase sheets widespread in the upper crust of the southwestern United States. Journal of Geophysical Research 96, 12-12,478.

Hulstein, R. 1994. Assessment Report on the 1993 geological and geochemical investigation of the Kiwi Property, Kennecott Canada Inc., Mayo Mining District, Yukon Territory, NTS map area 106E/2. Energy, Mines and resources, Government of Yukon, Assessent Report, 23 p.

Hunt, J. 2004. The geology and genesis of iron oxide-copper-gold mineralisation associated with Wernecke Breccia, Yukon, Canada. Unpublished PhD thesis, James Cook University, Queensland, Australia.

Idnurm, M. and Giddings, J.W. 1995. Paleoproterozoic-Neoproterozoic North America-Australia link: new evidence from paleomagnetism. Geology 23, 149-152.

Ireland, T.R., Floettmann, T., Fanning, C.M., Gibson, G.M. and Preiss, W.V. 1998. Development of the early Paleozoic Pacific margin of Gondwana from detrital-zircon ages across the Delamerian orogen, Geology 26, 243-246.

Irvine, T.N. and Baragar, W.R.A. 1971. A guide to the chemical classification of the common volcanic rocks. Canadian Journal of Earth Sciences 8, 523-548.

Jacobsen, S.B. and Wasserburg, G.J, 1980. Sm-Nd isotopic evolution of chondrites, Earth and Planetray Science Letters 50, 139-155.

Jefferson, C.W. and Parrish, R.R. 1989. Late Proterozoic stratigraphy, U-Pb zircon ages, and rift tectonics, Mackenzie Mountains, northwestern Canada. Canadian Journal of Earth Sciences 26, 1784-1801.

Jefferson, C.W. and Ruelle, J.C.L. 1987. The late Proterozoic Redstone Copper Belt, Mackenzie Mountains, Northwest Territories. *In:* J.A. Morin (Ed.) Mineral Deposits of Northern Cordillera. Canadian Institute of Mining and Metallurgy 37, 154-168.

Jercinovic, M.J., Gillerman, V.S. and Stein, H.J. 2002. Application of microprobe geochronology to hydrothermal monazite and thorite, Lemhi Pass District, Idaho. *In:* Abstracts with Programs, Geological Society of America 2002 annual meeting. Geological Society of America 34, 172.

Karlstrom, K.E. Williams, M.L., McLelland, J., Geissman, J.W. and Ahäll, K.I. 1999. Refining Rodinia: geological evidence for Australia-western U.S. connection in the Proterozoic. GSA Today 9, 1-7.

Kretz, R. 1983. Symbols for rock-forming minerals, American Mineralogist 68, 277-279.

Laughton, J.R., Thorkelson, D.J., Brideau, M., Hunt, J.A. and Marshall, D.D. 2005. Early Proterozoic orogeny and exhumation of Wernecke Supergroup revealed by vent facies of Wernecke Breccia, Yukon, Canada. Canadian Journal of Earth Sciences 42, 1033-1044.

Laznicka, P. and Gaboury, D. 1988. Wernecke breccias and Fe, Cu, U mineralization: Quartet Mountain-Igor area (NTS 106E). *In:* J.G. Abbott (Ed.), Yukon Geology, Volume 2, Expoloration and Geological Services Division, Yukon Region, Indian and Northern Affairs Canada, p. 42-50.

Le Maitre, R.W. (Ed.). 2002. Igneous rocks; a classification and glossary of terms; recommendations of the International Union of Geological Sciences Subcommission on the Systematics of Igneous Rocks. Cambridge, Cambridge University Press, 236 p.

LeCheminant, A.N. and Heaman, L.M. 1989. Mackenzie igneous events, Canada; middle Proterozoic hotspot magmatism associated with ocean opening. Earth and Planetary Science Letters 96, 38-48.

Lenz, A.C. 1972. Ordovician to Devonian history of northern Yukon and adjacent district of Mackenzie. Bulletin of Canadian Petroleum Geology 20, 321-359.

Li X.H., Zhou G., Zhao J., Fanning, C.N. and Compston, W. 1994. SHRIMP ion microprobe zircon U-Pb age and Sm-Nd isotopic characteristics of the NE Jiangxi ophiolite and its tectonic implications. Chinese Journal of Geochemistry 13, 317-325.

Li, Z.X., Zhang, L. and Powell, C.M. 1995. South China in Rodinia: part of the missing link between Australia-east Antarctica and Laurentia? Geology 23, 407-410.

Li, Z.X., Li X.H., Zhou H. and Kinny, P.D. 2002. Grenvillian continental collision in south China; new SHRIMP U-Pb zircon results and implications for the configuration of Rodinia, Geology 30, 163-166.

Li, Z.X., Cho, M. and Li, X.H. 2003a. Precambrian tectonics of East Asia and relevance to supercontintent evolution. Precambrian Research 122, 1-6.

Li, Z.X., Li, X.H. Kinny, P.D., Wang, J., Zhang, S. and Zhou, H. 2003b. Geochronology of Neoproterozoic syn-rift magmatism in the Yangtze Craton, South China and correlations with other continents: evidence for a mantle superplume that broke up Rodinia. Precambrian Research 122, 85-109.

Li, Z.X., Bogdanova, S.V., Collins, A.S., Davidson, A., De Waele, B., Ernst, R.E., Fitzsimons, I.C.W., Fuck, R.A., Gladkochub, D.P., Jacobs, J., Karlstrom, K.E., Lu, S., Natapov, L.M., Pease, V., Pisarevsky, S.A., Thrane, K. and Verinovsky, V. 2008. Assembly, configuration, and break-up history of Rodinia: a synthesis. Precambrian Resesarch, 179-210.

Ludwig, K.R. 2001a. SQUID 1.02: A user's manual. Special Publication 2, Berkley Geochronology Center.

Ludwig, K.R. 2001b. User's manual for Isoplot/Ex Rev. 2.49: A geochronological toolkit for Microsoft Excel. Special Publication 1a, Berkley Geochronology Center, Berkley.

Lund, K., Aleinikoff, J.N., Evans, K.V. and Kunk, M.J. 2004. Proterozoic basins and orogenic belts of central Idaho. In: Abstracts with Programs, Geological Society of America 2004 annual meeting. Geological Society of America 36, 271.

MacLean, B.C. and Cook, D.G. 2004. Revisions to the Paleoproterozoic Sequence A, based on reflection seismic data across the western plains of the Northwest Territories, Canada. Precambrian Research 129, 271-289.

McArthur, M.L., Tipnis, R.S. and Godwin, C.I. 1980. Early and Middle Ordovician conodont fauna from the Mountain diatreme, Northern Mackenzie Mountains, District of Mackenzie. In: Current Research, Part A. Geological Survey of Canada, Paper 80-1A, pp. 363-368.

Milidragovic, D. 2005. Petrography and geochemistry of the Quartet lamprophyres. Unpublished B.Sc. thesis, Simon Fraser University, 38 p.

Milidragovic, D., Thorkelson, D.J. and Marshall, D.D. 2006. Geology of the Quartet Mountain lamprophyre suite, Wernecke Mountains, Yukon. *In:* D.S. Emond, Bradshaw, G.D., L.L. Lewis and L.H. Weston (Eds.), Yukon Exploration and Geology 2005. Yukon Geological Survey, pp. 231-245.

Mitchell, R.H. 1986. Kimberlites; mineralogy, geochemistry, and petrology. Plenum Press, New York, 442 p.

Mitchell, R.H. 1995. Kimberlites, orangeites, and related rocks. Plenum Press, New York, 410 p.

Molnar, P. and Atwater, T. 1978. Interarc spreading and Cordilleran tectonics as alternates related to the age of subducted oceanic lithosphere. Earth and Planetary Science Letters 41, 330-340.

Moores, E.M. 1991. Southwest U.S.-east Antarctic (SWEAT) connection: a hypothesis. Geology 19, 425-428.

Mortensen, J.K. and Colpron, M. 1998. Geochronological and geochemical studies of the Coates Lake diatreme, southern Mackenzie Mountains, western N.W.T. In: F.A. Cook and P. Erdmer (Eds.) Slave-Northern Cordillera Lithospheric Evolution (SNORCLE) and Cordilleran Tectonics Workshop. Lithoprobe Secretariat, The University of British Columbia, Vancouver, B.C., Lithoprobe Report 64, p.278.

Mustard, P.S. and Roots, C.F. 1997. Rift-related volcanism, sedimentation, and tectonic setting of the Mount Harper Group, Ogilvie Mountains, Yukon Territory. Geological Survey of Canada, Bullettin 492, 92 p.

Norris, D.K. 1997. The geology, mineral and hydrocarbon potential of the northern Yukon Territory and northwestern District of Mackenzie. *In:* D.K. Norris (Ed.) The geology, mineral and hydrocarbon potential of northern Yukon Territory and northwestern district of Mackenzie. Geological Survey of Canada, Bulletin 422, Chap. 3, pp. 21-64.

Norris, D.K. and Dyke, L.D. 1997. Proterozoic. *In:* D.K. Norris (Ed.) The geology, mineral and hydrocarbon potential of northern Yukon Territory and northwestern district of Mackenzie. Geological Survey of Canada, Bulletin 422, Chap. 4, pp. 65-84.

Page, R.W. and Sun, S.S. 1998. Aspects of geochronology and crustal evolution in the Eastern Fold Belt, Mt. Isa Inlier. Australian Journal of Earth Sciences 45, 343-361.

Parrish, R.R. and Reichenbach, I. 1991. Age of xenocrystic zircon from diatremes of western Canada. Canadian Journal of Earth Sciences 28, 1232-1238.

Parrish, R.R. and Bell, R.T. 1987. Age of the NOR breccia pipe, Wernecke Supergroup, Yukon Territory. *In:* Radiogenic age and isotopic studies, Report 1. Geological Survey of Canada, Paper 87-2, pp. 39-42.

Pell, J. 1987. Alkaline ultrabasic rocks in British Columbia: carbonatites, nepheline syenites, kimberlites, ultramafic lamprophyres and related rocks. British Columbia Ministry of Energy, Mines and Petroleum Resources, Geological Survey Branch, Open File 1987-17.

Pell, J. 1994. Carbonatites, nepheline syenites, kimberlites and related rocks in British Columbia. British Columbia Ministry of Energy, Mines and Petroleum Resources, Bulletin 88, 133 p.

Peslier, A.H., Reisberg, L., Ludden, J. and Francis, D. 2000. Os isotopic systematics in mantle xenoliths; age constraints on the Canadian Cordillera lithosphere. Chemical Geology 166, 85-101.

Pisarevsky, S.A. and Natapov, L.M. 2003. Siberia and Rodinia. Tectonophysics 375, 221-245.

Pisarevsky, S.A., Wingate, M.T.D. and Harris, L.B., 2003. Late Mesoproterozoic (ca. 1.2 Ga) paleomagnetism of the Albany-Fraser orogen: no pre-Rodinia Australia-Laurentia connection. Geophysical Journal International 155, F6-F11.

Raetz, M., Krabbendam, M. and Donaghy, A.G. 2002. Compilation of U-Pb zircon data from the Willyama Supergroup, Broken Hill region, Australia: evidence for three tectonostratigraphic successions and four magmatic events? Australian Journal of Earth Sciences 49, 965-983.

Rainbird, R.H., Heaman, L.M., and Young, G.M. 1992. Sampling Laurentia: detrital zircon geochronology offers evidence for an extensive Neoproterozoic river system originating from the Grenville orogen, Geology 20, 351-354.

Rainbird, R.H., McNicoll, V.J., Theriault, R.J., Heaman, L.M., Abbott, J.G., Long, D.G.F. and Thorkelson, D.J. 1997. Pan-continental river system draining Grenville orogen recorded by U-Pb and Sm-Nd geochronology of Neoproterozoic quartzarenites and mudrocks, northwestern Canada, Journal of Geology 105, 1-17.

Rainbird, R.H., Stern, R.A. Khudoley, A.K. Kropachev, A.P., Heaman, L.M. and Sukhorukov, V.I. 1998. U-Pb geochronology of Riphean sandstone and gabbro from southeast Siberia and its bearing on the Laurentia-Siberia connection. Earth and Planetary Science Letters 164, 409-420.

Rämö, O.T., Huhma, H. and Kirs, J. 1996. Radiogenic isotopes of the Estonian and Latvian rapakivi granite suites: new data from the concealed Precambrian of the east European Craton. Precambrian Research 79, 209-226.

Renne, P.R., Deino, A.L., Walter, R.C., Turrin, B.D., Swisher, C.C., Becker, T.A., Curtis, G.H, Sharp, W.D. and Jaouni, A-R. 1994. Intercalibration of astronomical and radioisotopic time. Geology 22, 783-786.

Renne, P.R., Swisher, C.C., Deino, A.L., Karner, D.B, Owens, T.L and DePaolo, D.J. 1998. Intercalibration of standards, absolute ages and uncertainties in $^{40}Ar/^{39}Ar$ dating. Chemical Geology 145, 117-152.

Rock, N.M.S. 1987. The nature and origin of lamprophyres; an overview. *In:* J. Fitton and B. Upton (Eds.) Alkaline igneous rocks, Geological Society Special Publications 30, 191-226.

Rock, N.M.S. 1991. Lamprophyres. Blackie and Son, Glasgow, United Kingdom, 285 p.

Ross, G.M. 1991. Tectonic setting of the Windermere Supergroup revisited, Geology 19, 1125-1128.

Ross, G.M., Parrish, R.R. and Winston, D. 1992. Provenance and U-Pb geochronology of the Mesoproterozoic Belt Supergroup (northwestern United States): implications for age of deposition and pre-Panthalassa plate reconstructions. Earth and Planetary Science Letters 113, 57-76.

Ross, G.M. and Villeneuve, M.E. 1997. U-Pb geochronology of stranger stones in Neoproterozoic diamictites, Canadian Cordillera: implications for provenance and ages of deposition. *In:* Radiogenic age and isotope studies, Report 10. Geological Survey of Canada, Current Research 1997-F, pp. 141-155.

Ross, G.M., Villeneuve, M.E. and Theriault, R.J. 2001. Isotopic provenance of the lower Muskwa Assemblage (Mesoproterozoic, Rocky Mountains, British Columbia): new clues to correlation and source areas. Precambrian Research 111, 57-77.

Ross, G.M. and Villeneuve, M. 2003. Provenance of the Mesoproterozoic (1.45 Ga) Belt basin (western North America); another piece in the pre-Rodinia paleogeographic puzzle. Geological Society of America Bulletin 115, 1191-1217.

Rubatto, D. and Gebauer, D. 2000. Use of Cathodoluminescence for U-Pb zircon dating by ion microprobe: some examples from the western Alps. *In:* M. Pagel, V. Barbin, P. Blanc and D. Ohnenstetter (Eds.), Cathodoluminescence in geosciences. Springer, Berlin, Federal Republic of Germany (DEU), Chap. 15, pp. 373-392.

Schwab, D.L., Thorkelson, D.J., Mortensen, J.K., Creaser, R.A. and Abbott, J.G. 2004. The Bear River dykes (1265-1269 Ma); westward continuation of the Mackenzie dyke swarm into Yukon, Canada. Precambrian Research 133, 175-186.

Sears, J.W. and Price, R.A. 1978. The Siberian connection: a case for Precambrian separation of the North American and Siberian cratons. Geology 6, 267-270.

Sears, J.W. and Price, R.A. 2000 New look at the Siberian connection: no SWEAT. Geology 28, 267-270.

Sears, J.W. and Price, R.A. 2003. Tightening the Siberian connection to western Laurentia. Geological Society of America Bulletin 115, 943-953.

Sears, J.W., Price, R.A. and Khudoley, A.K. 2004. Linking the Mesoproterozoic Belt-Purcell and Udzha Basins across the west Laurentia-Siberia connection. Precambrian Research 129, 291-308.

Sha, G.S., Vervoort, J.D., Watkinson, A.J., Doughty, P.T., Prytulak, J., Lee, R.G. and Larson, P.B. 2004. Geochronologic constraints on the tectonic evolution of the Boehls Butte-Clearwater core complex; evidence from 1.01 Ga garnets. *In:* Abstracts with Programs, Geological Society of America, Rocky Mountain section-56th annual meeting, Geological Society of America, Cordilleran section-100th annual meeting, Geological Society of America 36, 72.

Smith, C.B. 1983. Pb, Sr and Nd isotopic evidence for sources of southern African Cretaceous kimberlites. Nature 304, 51-54.

Smith, C.B., Colgan, E.A., Hawthorne, J.B. and Hutchinson, G. 1988. Emplacement age of the Cross Kimberlite, southeastern British Columbia, by Rb-Sr phlogopite method. Canadian Journal of Earth Sciences 25, 790-792.

Spear, F.S. and Cheney, J.T. 1989. A petrogenetic grid for pelitic schists in the system SiO_2 -Al_2O_3 -FeO-MgO-K_2O-H_2O, Contributions to Mineralogy and Petrology 101, 149-164.

Stacey, J.S. and Kramers, J.D. 1975. Approximation of terrestrial lead isotope evolution by a two-stage model. Earth and Planetary Science Letters 26, 207-221.

Stern, R.A. 1997. The GSC Sensitive High Resolution Ion Microprobe (SHRIMP): analytical techniques of zircon U-Th-Pb age determinations and performance evaluation. *In:* Radiogenic age and isotope studies, Report 10. Geological Survey of Canada, Paper 1997-F, pp. 1-31.

Stern, R.A. and Amelin, Y. 2003. Assessment of errors in SIMS zircon U-Pb geochronology using a natural zircon standard and NIST SRM 610 glass. Chemical Geology 197, 111-142.

Sun, S.S. and McDonough, W.F. 1989. Chemical and isotopic systematics of oceanic basalts: implications for mantle composition and processes. *In:* Magmatism in the ocean basins, Geological Society Special Publications 42, 313-345.

Tappe, S., Foley, S.F., Jenner, G.A. and Kjarsgaard, B.A. 2005. Integrating ultramafic lamprophyres into the IUGS classification of igneous rocks: Rationale and implications, Journal of Petrology 46, 1893-1900.

Thorkelson, D.J. 2000. Geology and mineral occurrences of the Slats Creek, Fairchild Lake and "Dolores Creek" areas, Wernecke Mountains, Yukon Territory (106D/16, 106C/13, 106C/14). Exploration and Geological Services Division, Yukon Region, Indian and Northern Affairs Canada, Bulletin 10.

Thorkelson, D.J., Mortensen, J.K., Creaser, R.A., Davidson, G.J. and Abbott, J.G. 2001a. Early Proterozoic magmatism in Yukon, Canada: constraints on the evolution of northwestern Laurentia. Canadian Journal of Earth Sciences 38, 1479-1494.

Thorkelson, D.J., Mortensen, J.K., Davidson, G.J., Creaser, R.A., Perez, W.A. and Abbott, J.G. 2001b. Early Mesoproterozoic intrusive breccias in Yukon, Canada: the role of hydrothermal systems in reconstructions of North America and Australia. *In* Rodinia and the Mesoproterozoic earth-ocean system. *Edited by* J.K. Bartley and L.C. Kah. Precambrian Research 111, 31-55.

Thorkelson, D.J., Laughton, J.R., Hunt, J.A. and Baker, T. 2003. Geology and mineral occurrences of the Quartet Lakes map area (NTS 106E/1), Wernecke and Mackenzie mountains, Yukon. *In:* D.S. Emond and L.L. Lewis (Eds.), Yukon Exploration and Geology 2002. Exploration and Geological Services Division, Yukon region, Indian and Northern Affairs Canada, pp. 223-239.

Thorkelson, D.J., Abbott, J.G., Mortensen, J.K., Creaser, R.A., Villeneuve, M.E., McNicoll, V.J. and Layer, P.W. 2005. Early and middle Proterozoic evolution of Yukon, Canada. Canadian Journal of Earth Sciences 42, 1045-1071.

Vervoort, J.D., McClelland, W.C., Oldow, J.S., Watkinson, A.J. and Sha, G.S. 2005. Grenville-age metamorphism on the western margin of Laurentia, northern Idaho; evidence from Lu-Hf garnet geochronology. In: Abstracts with Programs, Geological Society of America 2005 annual meeting. Geological Society of America 37, 89.

Villeneuve, M.E., Theriault, R.J. and Ross, G.M. 1991. U-Pb ages and Sm-Nd signature of two subsurface granites from the Fort Simpson magnetic high, northwest Canada. Canadian Journal of Earth Sciences 28, 1003-1008.

Wade, B.P., Barovich, K.M., Hand, M., Scrimgeour, I.R. and Close, D.F. 2006. Evidence for early Mesoproterozoic arc magmatism in the Musgrave block, central Australia; implications for Proterozoic crustal growth and tectonic reconstructions of Australia. Journal of Geology 114, 43-63.

Whitmeyer, S.J. and Karlstrom, K.E. 2007. Tectonic model for the Proterozoic growth of North America. Geosphere 3, 220-259.

Young, G.M. 1995. Are Neoproterozoic glacial deposits preserved on the margins of Laurentia related to the fragmentation of two supercontinents? Geology 23, 153-156.

Young, G.M., Jefferson, C.W., Delaney, G.D. and Yeo, G.M. 1979. Middle and late Proterozoic evolution of the northern Canadian Cordillera and Shield, Geology 7, 125-128.